

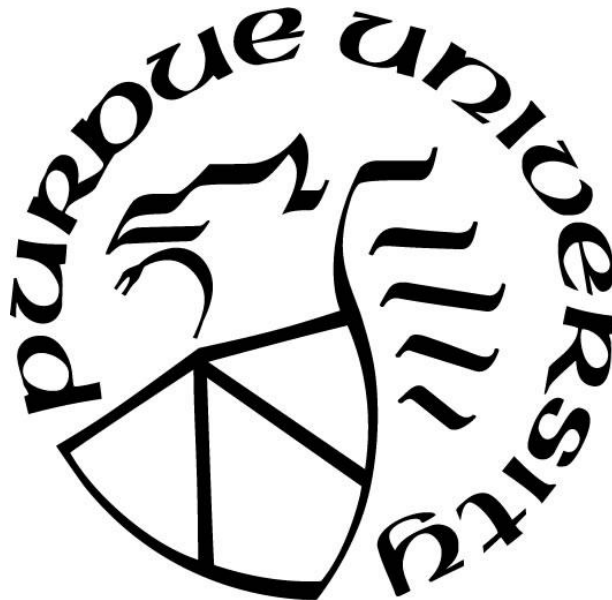
**PRELIMINARY DESIGN OF A HIGH-ENTHALPY HYPERSONIC WIND
TUNNEL FACILITY AND ANALYSIS OF FLOW INTERACTIONS IN A
HIGH-SPEED MISSILE CONFIGURATION**

by
Joshua C. Ownbey

A Thesis

*Submitted to the Faculty of Purdue University
In Partial Fulfillment of the Requirements for the degree of*

Master of Science in Aeronautics and Astronautics



School of Aeronautics and Astronautics
West Lafayette, Indiana
May 2021

THE PURDUE UNIVERSITY GRADUATE SCHOOL
STATEMENT OF COMMITTEE APPROVAL

Dr. Jonathan Poggie, Chair

School of Aeronautics and Astronautics

Dr. Timothée L. Pourpoint

School of Aeronautics and Astronautics

Dr. Joseph Jewell

School of Aeronautics and Astronautics

Dr. Carlo Scalò

School of Mechanical Engineering

Approved by:

Dr. Gregory Blaisdell

Dedicated to my family.

ACKNOWLEDGMENTS

Computer resources were provided by the Department of Defense High Performance Computing Program (DoD HPCMP) and by Information Technology at Purdue University, West Lafayette, Indiana. This work was supported by the Laboratory Directed Research and Development program at Sandia National Laboratories, a multimission laboratory managed and operated by National Technology and Engineering Solutions of Sandia LLC, a wholly owned subsidiary of Honeywell International Inc. for the U.S. Department of Energy's National Nuclear Security Administration under contract DE-NA0003525. The author wishes to thank Ph.D. student Utkarsh Pandey for sharing his advice and experimental data and thank Ph.D. student Caglar Yilmaz for experimental data from supersonic nozzle experiments. The author also wishes to thank Ph.D. students Robert Alviani and Akshay Deshpande, and Dr. Charles E. Lynch for assistance with software issues.

TABLE OF CONTENTS

LIST OF TABLES	7
LIST OF FIGURES	8
Abbreviations	13
Nomenclature	14
ABSTRACT	18
1. Introduction.....	19
1.1 True Enthalpy Hypersonic Test Facility	19
1.1.1 Method of Characteristics.....	19
1.1.2 Existing Tunnels	21
1.1.3 Thermochemistry Modeling	22
1.1.4 Project Scope	22
1.2 Hypersonic Missile	23
1.2.1 General Behavior of SBLI.....	23
1.2.2 Scope of Project.....	26
2. Methodology.....	28
2.1 Nozzle Contour Design.....	28
2.2 Method of Characteristics	30
2.2.1 Sivells' Computer Program for the Method of Characteristics	34
Transonic solution	36
Centerline distribution.....	37
Inviscid contour.....	38
Boundary layer correction.....	38
Input Parameters.....	39
2.3 Mesh Generation	40
2.3.1 Structured Grids.....	41
2.3.2 Unstructured Grids.....	42
2.4 Computational Fluid Dynamics (CFD) Code Configuration.....	43
2.4.1 SU2	44
2.4.2 CREATE Kestrel	47

2.5	Thermochemistry modeling	51
3.	High enthalpy hypersonic test facility	55
3.1	CONTUR	55
3.2	CFD Approach	61
3.3	Results	67
3.3.1	Nozzle Simulations	67
3.3.2	Thermodynamic Decomposition of N_2O	78
3.4	Conclusions and Future Work	81
4.	Shock / boundary-layer interaction in a hypersonic missile-fin configuration.....	84
4.1	CFD Approach	84
4.2	CFD Results	91
4.3	Conclusions	123
5.	Summary	125
	References	127
	APPENDIX A: Results of hypersonic missile-fin configurations	133
	APPENDIX B: Description of input parameters to CONTUR [8]	141
	APPENDIX C: MATLAB wrapper for Sivells' MOC computer program.....	146

LIST OF TABLES

Table 2.1: Reaction mechanism for real gas using Kestrel’s predefined <i>5-species air</i> . Units are in <i>cm</i> , <i>g</i> , <i>s</i> , and <i>K</i>	51
Table 2.2: Kinetic reaction mechanism for thermal decomposition of <i>N2O</i> . Units are in cm^3 , mole, and kJ.	52
Table 3.1: Values to estimate viscosity of an <i>N2-O2</i> gas mixture using Sutherland’s law of viscosity.	57
Table 3.2: Primary input parameters for CONTUR. Variables are listed as used in CONTUR.	60
Table 3.3: Select input parameters in SU2 for a simulated Mach 6.13 nozzle with a test article and test section.....	64
Table 3.4: Key inputs simulating the Mach 3.64 nozzle with a test section and test article in Kestrel.	66
Table 4.1: Key inputs simulating the Mach 3.64 nozzle with a test section and test article in Kestrel.	91

LIST OF FIGURES

Figure 1.1 Lattice structure in a Mach 1.4 nozzle [7].	20
Figure 1.2 Nozzle separated by lines for characteristic field method in a Mach 1.4 nozzle [7]...	20
Figure 1.3: Diagram of a SBLI on a blunt fin [18].	24
Figure 1.4: SBLI on a compression ramp without flow separation [22].	25
Figure 1.5: SBLI on a compression ramp with flow separation [23].	25
Figure 1.6: Drawing of conic missile configuration with fins number for reference.	27
Figure 1.7: Drawing of ogive missile configuration with fins numbered for reference.	27
Figure 2.1: A gradual expansion nozzle with characteristic lines designed for an exit Mach number, M_e . The straightening section and expansion section are separated by the inflection point [24].	29
Figure 2.2: Minimum length nozzle with characteristic lines [8].	29
Figure 2.3: Isentropic flow as it behaves in compression and expansion [27].	31
Figure 2.4: Regions of simple waves and nonsimple region [27].	32
Figure 2.5: Mach angle, μ , along an infinitesimal streamline [27].	33
Figure 2.6: Sample mesh in bounded flow for the MOC [27].	33
Figure 2.7: Sample of graphical solution to solving for point mesh point downstream of data curve [27].	33
Figure 2.8: Foelsch nozzle design with three flow regions [8].	35
Figure 2.9: Adapted Foelsch nozzle design with transitional flow [8].	35
Figure 2.10: Graphic that describes the basic method of Sivells' code. The labeled design points are used for reference [8].	36
Figure 2.11: Section of a nozzle contour at the throat displaying the sonic line for a transonic solution [8].	37
Figure 2.12: Sample input card for Sivells' computer program [8].	40
Figure 2.13: Coordinate transformation onto a rectangular (ξ, η) grid.	42
Figure 3.1: Sample input parameters for a Mach 6.13 nozzle with high temperature gas mixture of N_2 and O_2 .	56
Figure 3.2: Sample input parameters used for design of Mach 4 nozzle for cold N_2 gas.	56
Figure 3.3: Curve fit to estimate Sutherland's constant for a N_2 - O_2 gas mixture. The blue curve traces the data supplied by CEA. The dashed, red curve is the polynomial fit estimated by MATLAB using a solution for Sutherland's constant.	57

Figure 3.4: Inviscid and viscous flow nozzle geometry for the Mach 6.13 nozzle from CONTUR with characteristic lines separating the main flow regions in the nozzle.....	60
Figure 3.5: Inviscid and viscous flow geometries of a Mach 4 nozzle generated by CONTUR..	61
Figure 3.6: Mesh of Mach 6.13 nozzle with test section.....	63
Figure 3.7: Mesh of Mach 6.13 nozzle with test section and test article.	63
Figure 3.8: Mesh of Mach 3.64 nozzle with test section and test article.	63
Figure 3.9: Reference image used in BOS.....	65
Figure 3.10: Image of taken during run of Mach 3.64 nozzle.....	65
Figure 3.11: Experimental setup of nozzle and test section.....	66
Figure 3.12: Mach contour of Mach 6.13 nozzle	68
Figure 3.13: Reynolds number contour in Mach 6.13 nozzle.	68
Figure 3.14: Temperature contour for Mach 6.13 nozzle.....	68
Figure 3.15: Pressure contour of Mach 6.13 nozzle.....	69
Figure 3.16: Pressure and temperature on the nozzle wall for the Mach 6.13 contour.....	70
Figure 3.17: Mach number along nozzle centerline. The maximum Mach number is reached at the exit of the nozzle.	70
Figure 3.18: Pressure distribution at nozzle exit plane ($x/L = 1$) in the Mach 6.13 contour.....	71
Figure 3.19: Pressure contour of Mach 6.13 nozzle from $x/L = 0.95$ to $x/L = 1.02$	71
Figure 3.20: Mach number, momentum, and density distribution at nozzle exit plane for the Mach 6.13 contour. The local radius is $h = 4.078$ in.....	72
Figure 3.21: Density gradient magnitude of Mach 6.13 nozzle with test chamber and test article.	73
Figure 3.22: Density gradient magnitude of Mach 6.13 nozzle zoomed to view test article.	74
Figure 3.23: Temperature contour of Mach 6.13 nozzle with test chamber and test article.	74
Figure 3.24: Mach contour of the Mach 3.64 nozzle with a test section and test article.	76
Figure 3.25: Density gradient magnitude of the Mach 3.64 nozzle with a test section and test article.	76
Figure 3.26: Static pressure along nozzle wall in CFD simulation of Mach 3.64 nozzle.	77
Figure 3.27: Density gradient over test article 3 seconds into the run of Mach 3.64 nozzle.	77
Figure 3.28: Nozzle exit static pressure in the experiment of the Mach 3.64 nozzle.....	78
Figure 3.29: Species composition inside PFR with inflow values of 1100 K, 1000 psia, and 0.2 m/s.	79

Figure 3.30: Species decomposition at the exit of the PFR at constant velocity and pressures. ..	80
Figure 3.31: Temperature required for a complete reaction to occur at various pressures and velocities.	81
Figure 4.1: Surface mesh of conical missile.	85
Figure 4.2: Surface mesh on missile fin created by <i>Trex</i>	85
Figure 4.3: Surface mesh on blunt edge of missile fin and interface onto missile body created by <i>Trex</i>	86
Figure 4.4: <i>Trex</i> block of conical missile mesh.	86
Figure 4.5: Prism layers created by <i>Trex</i> on the symmetry line near the missile fin.	87
Figure 4.6: Slice of volume mesh around missile fins to view prism layers created by <i>Trex</i>	87
Figure 4.7: Main block of conical missile mesh.	88
Figure 4.8: Main block of conic missile mesh +1 configuration.	88
Figure 4.9: Slice of volume mesh in conic missile +1 configuration to view prism layers around missile fin.	88
Figure 4.10: Main block of ogive missile mesh.	89
Figure 4.11: Main block of ogive missile +1 configuration.	90
Figure 4.12: Surface y^+ value for the first cell spacing on the conic missile-fin configuration at $z = 0.003937 \text{ in.}$	92
Figure 4.13: Density gradient magnitude contours of conic missile configuration at various angles of attack.	95
Figure 4.14: Contours of the conical missile of Temperature (a)-(c) and Mach number (d)-(f) at various angles of attack.	96
Figure 4.15: Contours of the conical missile of Mach number (a)-(c) and density gradient magnitude (d)-(f) at various angles of attack with a slice at $x = 15.79 \text{ in.}$	97
Figure 4.16: Contours of the conical missile of Mach number (a)-(c) and density gradient magnitude (d)-(f) at various angles of attack with a slice at $x = 17.26 \text{ in.}$	98
Figure 4.17: Pressure distribution along slices parallel to the symmetry boundary (a) and 45° between fins (b) in conic missile configuration.	99
Figure 4.18: Temperature distribution along slices parallel to the symmetry boundary (a) and 45° between fins (b) in conic missile configuration.	99
Figure 4.19: Skin friction coefficient magnitude along slices parallel to the symmetry boundary (a) and 45° between fins (b) in conic missile configuration.	99
Figure 4.20: Mach number contour with a slice at $x = 14.8 \text{ in}$ and velocity streamtraces on conic missile-fin configuration.	100

Figure 4.21: Density gradient magnitude contours of conic missile +1 configuration at various angles of attack.	103
Figure 4.22: Contours of the conic missile +1 configuration of Temperature (a)-(c) and Mach number (d)-(f) at various angles of attack.....	104
Figure 4.23: Contours of the conic missile +1 configuration of Mach number (a)-(c) and density gradient magnitude (d)-(f) at various angles of attack with a slice at $x = 15.79 \text{ in.}$	105
Figure 4.24: Contours of the conic missile +1 configuration of Mach number (a)-(c) and density gradient magnitude (d)-(f) at various angles of attack with a slice at $x = 17.26 \text{ in.}$	106
Figure 4.25: Pressure distribution along slices parallel to the symmetry boundary in conic missile +1 configuration (a) and slices on Fin 1a and Fin 2a (b).	107
Figure 4.26: Temperature distribution along slices parallel to the symmetry boundary in conic missile +1 configuration (a) and slices on Fin 1a and Fin 2a (b).	107
Figure 4.27: Skin friction coefficient magnitude along slices parallel to the symmetry boundary in conic missile +1 configuration (a) and slices on Fin 1a and Fin 2a (b).	107
Figure 4.28: Mach number contour with a slice at $x = 14.8 \text{ in}$ and velocity streamtraces on conic +1 missile-fin configuration.....	108
Figure 4.29: Density gradient magnitude contours of ogive missile configuration at various angles of attack.....	110
Figure 4.30: Contours of the ogive missile of Temperature (a)-(c) and Mach number (d)-(f) at various angles of attack.....	111
Figure 4.31: Contours of the ogive missile of Mach number (a)-(c) and density gradient magnitude (d)-(f) at various angles of attack with a slice at $x = 15.79 \text{ in.}$	112
Figure 4.32: Contours of the ogive missile of Mach number (a)-(c) and density gradient magnitude (d)-(f) at various angles of attack with a slice at $x = 17.26 \text{ in.}$	113
Figure 4.33: Pressure distribution along slices parallel to the symmetry boundary (a) and 45° between fins (b) in ogive missile configuration.....	114
Figure 4.34: Temperature distribution along slices parallel to the symmetry boundary (a) and 45° between fins (b) in ogive missile configuration.....	114
Figure 4.35: Skin friction coefficient magnitude along slices parallel to the symmetry boundary (a) and 45° between fins (b) in ogive missile configuration.....	114
Figure 4.36: Mach number contour with a slice at $x = 14.8 \text{ in}$ and velocity streamtraces on ogive missile-fin configuration.....	115
Figure 4.37: Density gradient magnitude contours of ogive +1 missile configuration at various angles of attack.	117
Figure 4.38: Contours of the ogive +1 missile of Temperature (a)-(c) and Mach number (d)-(f) at various angles of attack.....	118

Figure 4.39: Contours of the ogive +1 missile of Mach number (a)-(c) and density gradient magnitude (d)-(f) at various angles of attack with a slice at $x = 15.79$ in.	119
Figure 4.40: Contours of the ogive +1 missile of Mach number (a)-(c) and density gradient magnitude (d)-(f) at various angles of attack with a slice at $x = 17.26$ in.	120
Figure 4.41: Pressure distribution along slices parallel to the symmetry boundary (a) and 45° clockwise and counterclockwise from symmetry boundary (b) in ogive +1 missile configuration.	121
Figure 4.42: Temperature distribution along slices parallel to the symmetry boundary (a) and 45° clockwise and counterclockwise from symmetry boundary (b) in ogive +1 missile configuration.	121
Figure 4.43: Skin friction coefficient magnitude along slices parallel to the symmetry boundary (a) and 45° clockwise and counterclockwise from symmetry boundary (b) in ogive +1 missile configuration.	122
Figure 4.44: Mach number contour and velocity streamtraces on ogive +1 missile-fin configuration.	122
Figure 4.45: Sample of solution dependency on mesh from Mach number contour.	123
Figure A.1: Contours of the conic missile of Mach number (a)-(c) and density gradient magnitude (d)-(f) at various angles of attack with a slice at $x = 10.77$ inches.	133
Figure A.2: Contours of the conic missile of Mach number (a)-(c) and density gradient magnitude (d)-(f) at various angles of attack with a slice at $x = 12.68$ inches.	134
Figure A.3: Contours of the conic missile +1 configuration of Mach number (a)-(c) and density gradient magnitude (d)-(f) at various angles of attack with a slice at $x = 10.77$ inches.	135
Figure A.4: Contours of the conic missile +1 configuration of Mach number (a)-(c) and density gradient magnitude (d)-(f) at various angles of attack with a slice at $x = 12.68$ inches.	136
Figure A.5: Contours of the ogive missile of Mach number (a)-(c) and density gradient magnitude (d)-(f) at various angles of attack with a slice at $x = 10.77$ inches.	137
Figure A.6: Contours of the ogive missile of Mach number (a)-(c) and density gradient magnitude (d)-(f) at various angles of attack with a slice at $x = 12.68$ inches.	138
Figure A.7: Contours of the ogive +1 missile configuration of Mach number (a)-(c) and density gradient magnitude (d)-(f) at various angles of attack with a slice at $x = 10.77$ inches.	139
Figure A.8: Contours of the ogive +1 missile configuration of Mach number (a)-(c) and density gradient magnitude (d)-(f) at various angles of attack with a slice at $x = 12.68$ inches.	140

ABBREVIATIONS

AEDC	Arnold Engineering Development Complex
AoA	Angle of Attack
AUSM	Advection Upstream Splitting Method
BOS	Background oriented schlieren
CEA	Chemical Equilibrium with Applications
CFD	Computational Fluid Dynamics
DoD	Department of Defense
FGMRES	Flexible Generalized Minimum Residual
FVM	Finite Volume Method
GMRES	Generalized Minimum Residual
HLL	Harten, Lax and van Leer
HLLE+	Harten, Lax, van Leer and Einfeldt
KCFD	Kestrel Computational Fluid Dynamics
LU-SGS	Lower-Upper Symmetric Gauss-Seidel
MOC	Method of characteristics
MOL	Method of Lines
MUSCL	Monotonic Upwind scheme for conservation law
ODE	Ordinary Differential Equation
PDE	Partial Differential Equation
PFR	Plug Flow Reactor
RANS	Reynolds-averaged Navier-Stokes
SA	Spalart-Allmaras
SBLI	Shock / boundary-layer interaction
SST	Shear Stress Transport

NOMENCLATURE

a	Speed of sound
A	Cross-sectional flow area
A_i	Pre-exponential factor in Arrhenius equation
$a_{i,m}$	Effective internal surface area per unit length of material m
c_{a2}, c_{e2}	Constants in Menter transition model
$c_{b1}, c_{b2}, c_{w1}, c_{v1}$	SA constants
C_D	Discharge coefficient
C_f	Skin friction coefficient
c_p	Specific heat at a constant pressure
\bar{C}_p	Mean heat capacity per unit mass
c_v	Specific heat at a constant volume
d	Smallest distance from field point to grid line
D	Coefficient in (2.15)
c_v	Specific heat at a constant volume
E	Total energy per unit mass
E_i	Activation energy
E_γ	Destruction source term
F	Drag force exerted from wall to gas
F_c	Factor used in Spalding-Chi method for a C_f correlation
\vec{F}^c	Convective flux term in main SU2 formulation
F_{length}	Constant in Menter transition model
F_{onset}	Function to active E_γ
F_{R_8}	Factor used in Spalding-Chi method for a Re correlation
$f_w, f_{v2}, f_{t2}, f_{v1}$	SA functions
\vec{F}^v	Viscous flux term in main SU2 formulation

F_1	SST blending function
H	Ratio δ^*/θ ; total enthalpy
h_k	Specific enthalpy of species k
k	Turbulent kinetic energy
K_g	Number of species
k_i	Reaction rate
k_{tot}	Total thermal conductivity
k_0, k_∞	Reaction rate for low and high-pressure dependent fall-off reactions
M	Mach number
P	Static pressure
Pr	Prandtl number
P_{red}	Reduced pressure in Lindemann's equation
P_γ	Transition source term
q	Velocity within boundary-layer
Q	Riemann invariant along ξ characteristic
Q	Source term in main SU2 formulation
Q_e	Heat flux from surroundings to outer wall
r	Radius
R	Riemann invariant along η characteristic
RC	Ratio of the throat radius of curvature to the throat radius
R_c	Radius of curvature
Re	Reynolds number
S	Sutherland's constant; strain rate
\dot{s}_k	Molar production rate of k species
S_1	RC+1
t	Time
T	Static temperature
T_{aw}	Temperature of the adiabatic wall
u	Velocity

u_τ	Friction velocity
\mathbf{U}	State variables in main SU2 formulation
W_k	Molecular weight of species k
X	Distance ratio, (2.18)
Y_k	Mass fraction
α	Condition defining distribution type in (2.25)
β, β^*	SST constants, temperature exponent in Arrhenius equation
γ	Specific heat ratio, c_p/c_v ; turbulent intermittency
δ^*	Displacement thickness in boundary-layer
δ_{ij}	Kronecker delta
ϵ	Turbulent dissipation rate
η	Transformed coordinate, designates left running characteristic
θ	Momentum thickness
λ	$\left(\frac{1+\sigma}{(\gamma-1)S_1}\right)^{1/2}$
μ	Mach angle, molecular viscosity
μ_t	Turbulent viscosity
μ_{tot}	Total viscosity
ν	Prandtl-Meyer function, kinematic viscosity
$\tilde{\nu}$	Scaled eddy viscosity
ξ	Transformed coordinate, designates right running characteristic
ρ	Density
σ	0 for planar flow, 1 for axisymmetric flow (Sivells); turbulent Prandtl number (SA)
σ_k, σ_ω	Damping coefficients in SST
σ_γ	Constant in Menter transition model
τ	Shear stress
φ	Flow angle
ω	Specific turbulent dissipation or turbulence frequency
Ω	Vorticity magnitude

Subscripts

e	Value at the temperature T_e at the boundary-layer edge
ref	Reference value for Sutherland's law
w	Value at the wall

ABSTRACT

An approach for designing a high-enthalpy wind tunnel driven by exothermic chemical reactions was developed. Nozzle contours were designed using CONTUR, a program implementing the method of characteristics, to design nozzle contours at various flow conditions. A reacting mixture including nitrous oxide has been identified as the best candidate for providing clean air at high temperatures. The nitrous oxide (N_2O) has a few performance factors that were considered, specifically the combustion of the gas. Initial CFD simulations were performed on the nozzle and test region to validate flow characteristics and possible issues. Initial results show a fairly uniform exit velocity and ability to perform testing.

In a second phase of the work, two generic, high-speed missile configurations were explored using numerical simulation. The mean flow was computed on both geometries at a 0° and 45° roll and 0° , 1° , and 10° angle of attack. The computations identified complex flow structures, including three-dimensional shock / boundary-layer interactions, that varied considerably with angle of attack.

1. INTRODUCTION

Hypersonic flight has been of strong interest in the aerodynamic community since the end of the Second World War [1]. The nature and application of hypersonic flow can be understood through careful experiments and simulations. Hypersonic testing, however, is limited by the experimental facility. The facility may induce flow disturbances that affect the flowfield and test results or the application of the experimental data.

One of the primary topics of investigation is shock / boundary-layer interaction around hypersonic vehicles. The three-dimensionality and complexity in these flow regions presents a challenge for both simulation and design. The following sections introduce the concept of creating a true enthalpy hypersonic test facility that can accommodate long run times, with clean air at a relatively low cost, and the examination of flow structure near the fins of two configurations of a hypersonic missile.

1.1 True Enthalpy Hypersonic Test Facility

The interest of high-speed flight has encouraged the creation of hypersonic test facilities. Initial testing was unable to confidently predict hypersonic flight due to technological limitations. Past hypersonic wind tunnels have had problems with flow uniformity, inadequate test times, contaminated flow, and/or high cost. Recent tunnels such as the H_2 arc-heated tunnel at the Arnold Engineering Development Complex (AEDC) can run for a significant duration of time but at a high cost [2]. Propulsion powered wind tunnels are more efficient, but often have contaminated flow due to combustion effects [3] in the form of condensation. Condensation can reduce the Mach number or disrupt the flow over the test article. A sudden expansion in the flow to achieve hypersonic Mach numbers may cause an uneven distribution of flow in the test region [4] and can lead to unacceptable flow quality. This distribution can be quantified by pressure or velocity. It is desired to have a clean-air, uniform flow for accurate representation of flight conditions.

1.1.1 Method of Characteristics

Supersonic wind tunnels have been of high interest in the aerodynamic community since the first nozzle design by de Laval in 1888 [5]. De Laval's innovation inspired future engineers

and scientists to study and characterize the flow through supersonic nozzles. Stodola was the first to publish definitive data on supersonic nozzle experiments in 1903 [6], which led to the method of characteristics (MOC) for nozzle design developed by Prandtl and Busemann in 1929. The intent was to design a nozzle with uniform flow at the exit to provide well-controlled supersonic wind tunnel test conditions. The original MOC was a solution to the wave equation through a graphical method [5]. Developments in technology permitted the implementation of numerical methods.

Several codes and methods exist to solve the MOC. In 1948, Cronvich described two methods, the lattice method and the field method, that could be used to solve the MOC. The lattice method, displayed in Figure 1.1, develops a solution for a bounded flow by progressing along the characteristic lines. A solution is found at each “lattice-point.” The field method, shown in Figure 1.2, uses the characteristic lines to partition the flow into patches in which the flow variables are assumed constant. It is assumed that crossing the characteristic lines accounts for some discontinuity in flow variables [7].

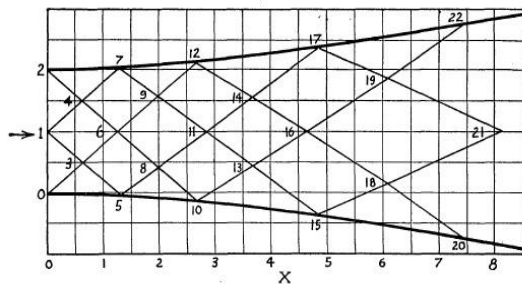


Figure 1.1: Lattice structure in a Mach 1.4 nozzle [7].

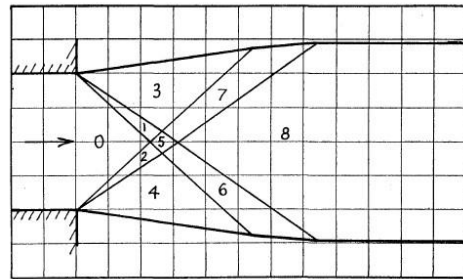


Figure 1.2: Nozzle separated by lines for characteristic field method in a Mach 1.4 nozzle [7].

The initial methods previously described did not account for boundary-layer growth, and hence were only accurate for very high Reynolds number flows with thin boundary-layers. The assumption was also made to neglect the transonic solution at the nozzle throat. This assumption caused the acceleration to be zero at the throat which results in a longer nozzle design when using the MOC. Sivells later developed a computer code to address the issue and shortcomings of an inviscid solution to provide a robust design [8]. Sivells' code can create a nozzle contour that is

capable of providing supersonic and hypersonic Mach numbers [8]. This code is used in the design of the hypersonic test facility.

1.1.2 Existing Tunnels

The test facility in discussion would be capable of replicating enthalpy, stagnation pressure, Mach number, and various static thermodynamic conditions (e.g., temperature). This capability is unlike “quiet” wind tunnels that attempt to mitigate the amount of turbulence in the nozzle. Quiet wind tunnels focus on creating a laminar, rather than turbulent, tunnel sidewall boundary-layer to reduce the level of noise in the freestream flow by retarding the flow expansion and implementing techniques such as bleed slots on the nozzle wall [9]. A nozzle with a slow expansion mitigates the risk of Görtler vortices in axisymmetric nozzles and promotes a favorable pressure gradient [9]. An unstable separation bubble may appear on the nozzle surface as a result of machining. It was believed by Schneider et al. that this separation bubble caused laminar flow to transition to turbulence [10]. The aim of a bleed slot is to remove disturbances in boundary-layer before transition occurs so laminar flow can be maintained [9].

A high-enthalpy test facility would allow experimental studies into reacting flow and non-equilibrium effects caused by the high energy within the flow [11]. There currently exist several options to create a true enthalpy hypersonic testing facility. Most of these tunnels can be classified as: foreign gas, impulse, arc-heated, and combustion heated [3].

A foreign gas facility utilizes gases other than air as a medium. The approach of these facilities is to use a foreign gas with a reduced ratio in specific heat, γ , and Mach and Reynolds numbers scaling to estimate real-gas effects. These tunnels typically investigate reentry phenomena on blunt objects where γ is relatively stable and can be compared with experimental data of flow over the same geometry, Mach, and Reynolds numbers in air; furthermore, the efficacy of this method for high-lift or slender bodies where γ varies considerably in the flowfield remains undetermined [3].

An impulse facility, such as shock tunnels and hotshot tunnels, targets high Mach numbers ($\text{Mach} > 15$) for a short interval (1-100 milliseconds). An impulse facility can provide realistic flow conditions at hypersonic and high-pressure flows; however, their restricted testing duration cause poor test repeatability and possible flow contamination [3].

Arc-heated facilities use a high-current discharge upstream of the throat to add enthalpy to the flow medium. These facilities can run for several minutes but are limited to moderate Mach numbers, often experience structural damage and consume a considerable amount of power [3]. The arc-heated tunnel at AEDC can run for 30 minutes at stagnation conditions of 0.3 MPa and 5300 K but requires a substantial amount of power (43 MW) [2].

Combustion heated facilities are typically used for their long run-time and high temperature capabilities. Current facilities typically use a combustion process involving gas species, often involving a hydrocarbon, that may contaminate and compromise the flow quality in the test section [3, 12]. The current project considers the drawbacks of these tunnels, and investigates and designs a suitable solution to mitigate the problems with conventional approaches.

1.1.3 Thermochemistry Modeling

The desire for clean air in a true-enthalpy hypersonic test facility led to the decision to utilize nitrous oxide, N_2O , as the main propellant. Nitrous oxide has advantage of producing species compositions that approximate air via thermal decomposition (with additional N_2). Nitrous oxide may decompose exothermically or endothermically; both require relatively high amounts of energy to occur. The exothermic produces the desired outcome. The endothermic reaction, however, has a lower activation energy and produces nitric oxide, NO , as byproduct. Nitric oxide contaminates the working gas in a wind tunnel in a manner similar to the way that carbon dioxide or water contaminate vitiated systems. It is desired to quantify the amount of NO created in the system and temperature required to initiate the reaction.

The temperature required to pre-heat the nitrous oxide to initiate thermal decomposition is relatively high, thus a catalyst must be considered to start the reaction. The selection of a catalyst may effectively lower the activation energy required to initiate a reaction and may mitigate the production of nitric oxide. The catalyst and nitrous oxide decomposition can be implemented into the nozzle design once the mechanisms are understood.

1.1.4 Project Scope

The current project researched possible methods for designing a nozzle that can account for viscous and thermochemical effects. A procedure was developed to easily create different

supersonic and hypersonic nozzles for use in a high enthalpy facility. This procedure can be modified by changing gas properties such as γ and the gas constant and various geometry conditions used in the Sivells' MOC code, CONTUR. It is important to define a process that can quickly create nozzle geometries that can accommodate to different chemical kinetics upstream of the nozzle and select the optimal design. Simulations of nozzle designs visualize the flow inside the nozzle and in a test chamber with a pressure corresponding to 95,000 feet in altitude so that the quality of the flow can be confirmed and the compared with the design criteria. Additionally, simulations are compared with experimental results to validate the numerical computations. The simulations and experiment serve to validate the selected design method.

1.2 Hypersonic Missile

Flow unsteadiness and shock / boundary-layer interactions (SBLI) have been extensively researched since the 1960's [13]. The resulting three-dimensionality and unsteady flow in high-speed flight affect many areas such as flight mechanics, material fatigue, and heat transfer rates [13]. Shock / boundary-layer interactions were noted by many to be complex, unsteady 3D structures [14, 15, 16, 17, 18]. The interactions in these regions produced several areas of research to identify the causation and effects which include investigations on possible forcing mechanisms upstream and downstream of the SBLI [18] and analysis of the mean flow on simple geometries [14, 15].

1.2.1 General Behavior of SBLI

Shock / boundary-layer interactions are viscous flow interactions which occur when a shock created by the object of study or generated by some disturbance in the flowfield upstream of the interaction impinges on a boundary-layer [18]. The SBLI phenomenon studied on basic geometries such as ramps and blunt fins can show similar features: a separation shock which firsts impinges on the boundary-layer followed by a high-pressure region where a recirculation bubble forms and a reattachment shock downstream of the bubble where the boundary-layer reattaches.

Geometry significantly affects the behavior of SBLI. Separation bubbles are most easily visualized in low Reynolds number flows where the shear force cannot overcome the adverse pressure gradient created by the SBLI. A blunt fin creates a bow shock that causes the upstream

flow to separate. A separation shock forms as a result of the separated flow and impinges on the bow shock which causes extreme heating and pressure on the fin's leading edge [15]. This interaction is visualized in Figure 1.3.

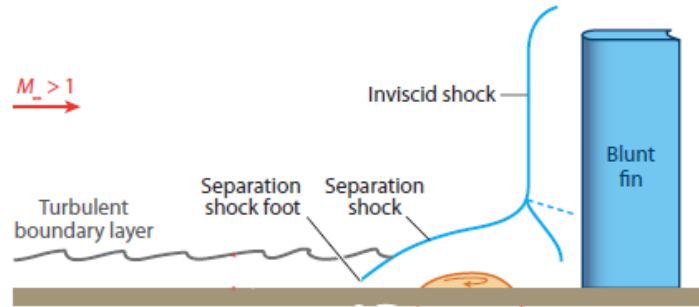


Figure 1.3: Diagram of a SBLI on a blunt fin [18].

In 1984, Hung and Buning simulated supersonic flow over a blunt fin and compared the results with the experiments performed by Dolling and Bogdonoff in [14] and Dolling et al. in [19] [15]. The simulations were performed using a Reynolds-averaged Navier-Stokes formulation with an algebraic, eddy-viscosity turbulence model, Baldwin & Lomax, to examine the SBLI and mean flow characteristics on a blunt fin. The simulations displayed good overall agreement with the experiments by comparing the pressure on the surface of the fin. Hung and Buning observed the rise in pressure from a separation shock and the flow reattachment and the general effects of an incoming turbulent boundary-layer.

A compression ramp in high-speed flow can have a SBLI with or without separated flow. Settles et al. performed experiments to investigate the separation on 2D ramp at various angles of attack of 8° , 16° , 20° , and 24° in supersonic, high Reynolds number flow [20]. The study showed that the size of the separation bubble increased with the ramp angle. The flow transitioned from fully attached flow on the 8° ramp to significantly separated flow on the 24° ramp. Settles et al. concluded that the experiments confirmed a prior theory suggested in [21] that separation in a shock / boundary-layer interaction is delayed or avoided at high Reynolds numbers [20]. A diagram showing a SBLI on a compression ramp without separation is shown in Figure 1.4. The shock is refracted by the boundary-layer, creating weaker waves depicted by the dashed lines [22]. A recirculation region appears when the oblique shock upstream of the compression ramp produces

a significant adverse pressure gradient [20]. Figure 1.5 shows a schematic of a SBLI on a 15° compression ramp. The oblique shock upstream of the ramp causes the separation bubble indicated by the recirculating region. The boundary-layer reattaches after the reattachment shock on the ramp.



Figure 1.4: SBLI on a compression ramp without flow separation [22].

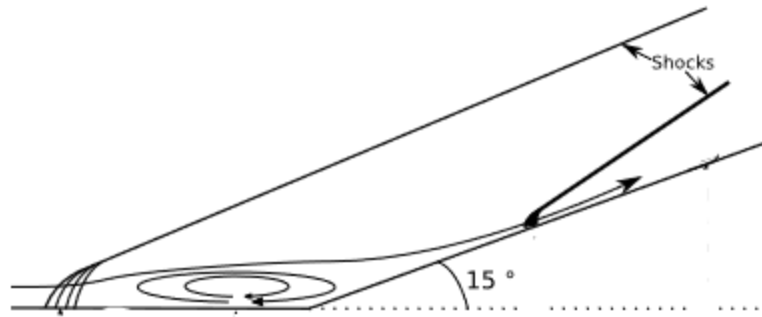


Figure 1.5: SBLI on a compression ramp with flow separation [23].

Clemens and Venkateswaran reviewed results obtained by several authors to form a conclusion on the mechanism impacting low-frequency unsteadiness in the SBLI separation. A large portion of former investigations found that unsteadiness was caused by the upstream fluctuations in the boundary-layer or large-scale instability inherent in the separated flow [18]. Clemens and Venkateswaran viewed that both driving mechanisms existed in SBLI where separation exists, "...the downstream mechanism dominates for strongly separated flows, and a combined mechanism dominates for weakly separated flows," [18]. Strong separation is expected to occur in flow with strong shock waves and low Reynolds numbers. The strong shocks interfere with the boundary-layer and the low Reynolds number flow cannot overcome the adverse pressure

gradient. Conversely, weak separation is expected in flow with high Reynolds numbers where flow is more resistant to separation.

1.2.2 Scope of Project

The study of SBLI and the resulting flow unsteadiness have been extensively researched on basic geometries, as described in the previous sections. The current study examines the mean flow structure of the SBLI around the four fins generic high-speed missile configurations at an angle of attack (AoA) of 0° , 1° and 10° in numerical simulations. Drawings of the missile configurations are shown in Figure 1.6 and Figure 1.7, and are provided courtesy of Joseph Vasile at the US Army Research Laboratory. The two missile geometries considered have matching geometries for the cylindrical portion of the body, but one has a conical and the other an ogive nose. The identified complex 3D flow of the hypersonic missiles can be used for future comparison with experiments. The simulations described are the first step to understanding the flow physics on a hypersonic missile-fin configuration.

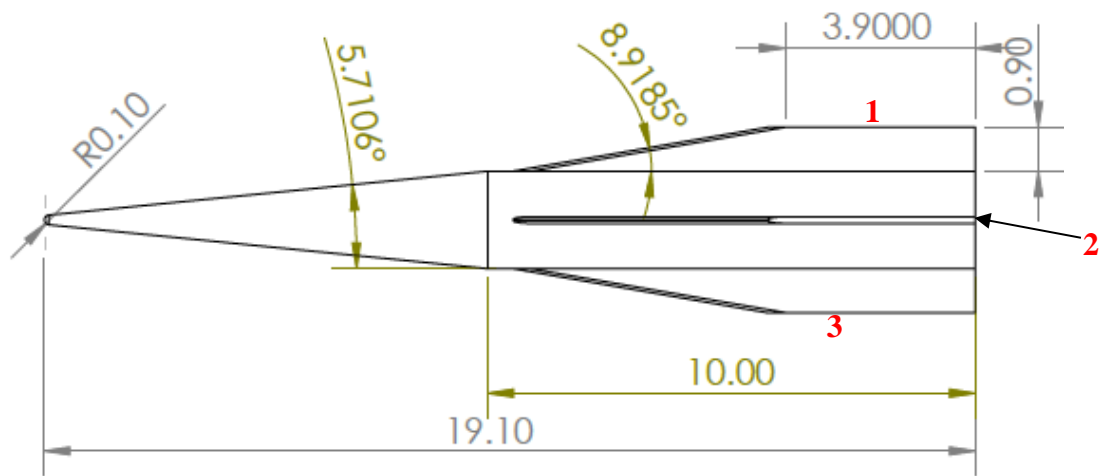


Figure 1.6: Drawing of conic missile configuration with fins number for reference.

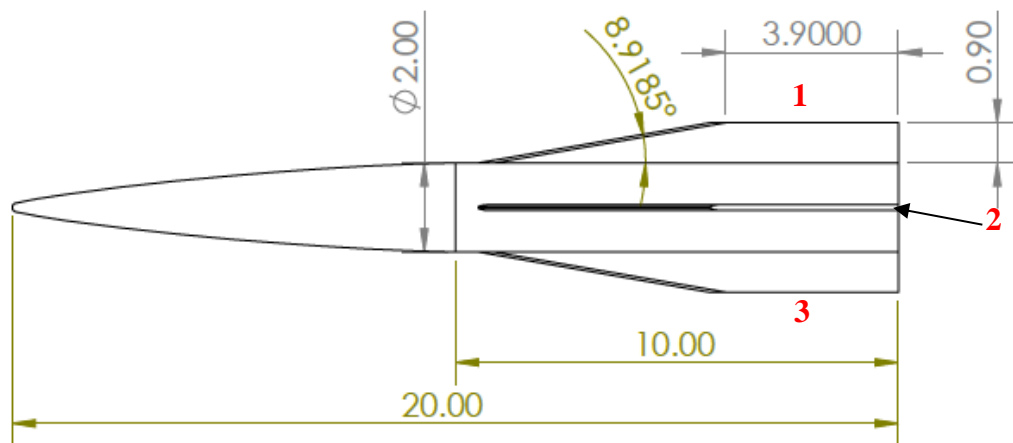


Figure 1.7: Drawing of ogive missile configuration with fins numbered for reference.

2. METHODOLOGY

This section discusses the general methods used in each project. The methods used to design and simulate the nozzle contour and simulate the hypersonic missile configurations are explained. Detail about each method is provided when appropriate and the details of each project can be easily distinguished; however, most of the specific applications of the methods used are described in subsequent chapters.

The nozzle design procedure used an existing method of characteristics program, CONTUR, to create a contour capable of producing high-quality, hypersonic flow. The various inputs of CONTUR made the program quite robust and required knowledge of the variable inputs before creating a successful contour. The contours created were meshed in Pointwise® and simulated in CFD codes to examine the flowfield using a Reynolds-averaged Navier-Stokes formulation and a two-equation turbulence model, shear-stress transport model. The computations assumed a perfect gas to simplify calculations. A hypersonic nozzle was simulated in SU2, and a supersonic nozzle was simulated in Kestrel. The calculation of the supersonic nozzle was compared with experimental results.

Hypersonic missile configurations were meshed in Pointwise® and simulated in Kestrel using a Reynolds-averaged Navier-Stokes formulation. A 5-species model was used to simulate possible nonequilibrium effects in air. Calculations were computed with a freestream Mach number of 5.9 and a unit Reynolds number Re/L of 6.1 million. The mean flowfield was examined in Tecplot to visualize SBLI's and flow structures.

2.1 Nozzle Contour Design

Two general nozzle designs exist: a gradual expansion nozzle, seen in Figure 2.1, and a minimum length nozzle, seen in Figure 2.2. A minimum length nozzle has a sharp expansion at the throat with ϕ_w equal to ϕ_{max} from the Prandtl-Meyer function. These nozzles are typically used on rocket nozzle applications in order to reduce weight while achieving maximum exit velocity. A gradual expansion has two sections – an expansion section and a straightening section – that are separated by an inflection point. The inflection point is defined where $\phi_w = \phi_{max}$.

Gradual expansion nozzles are typically used in wind tunnels where a good flow quality is desired at the nozzle exit [24].

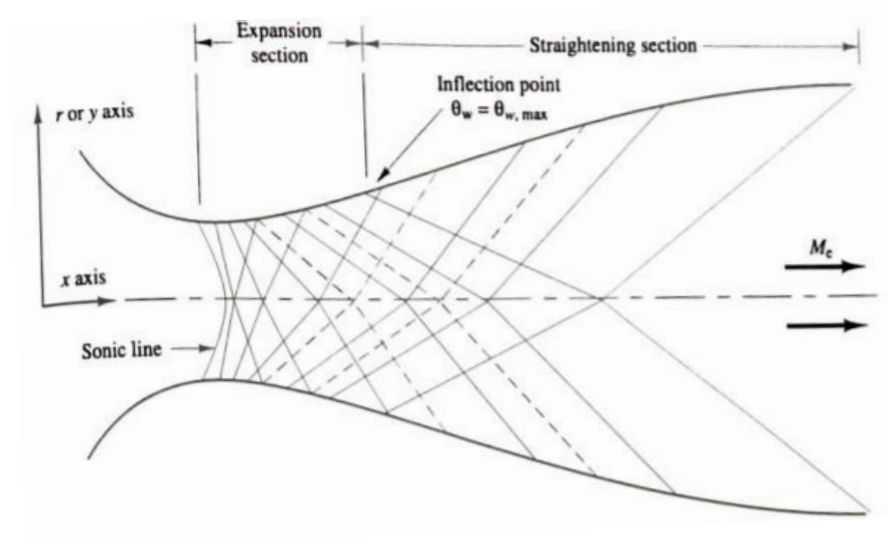


Figure 2.1: A gradual expansion nozzle with characteristic lines designed for an exit Mach number, M_e . The straightening section and expansion section are separated by the inflection point [24].

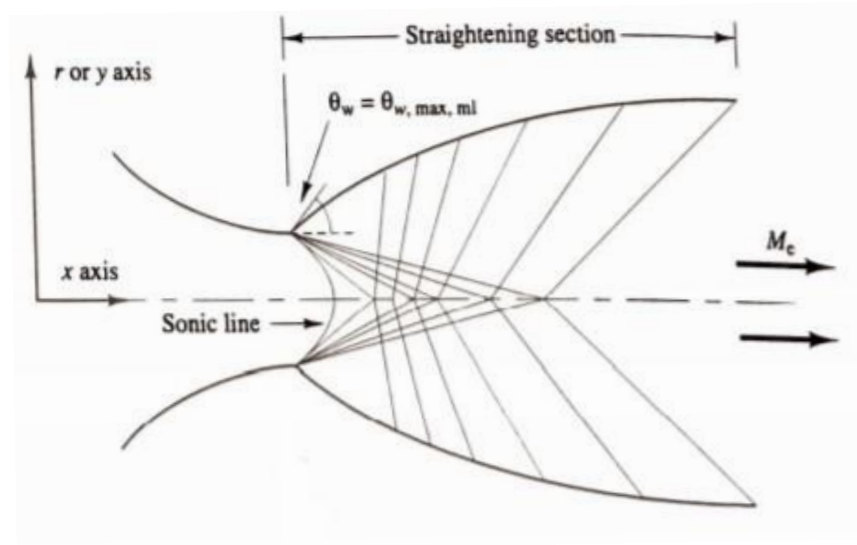


Figure 2.2: Minimum length nozzle with characteristic lines [8].

Two gradual expansion nozzle designs are considered: asymmetric and axisymmetric. An asymmetric nozzle is advantageous in the design of a variable Mach number wind tunnel. Asymmetric nozzles are not typically used in hypersonic wind tunnel applications since undesired flow characteristics are produced. An uneven pressure distribution exists between the flat and contoured walls which produces an uneven velocity at the nozzle exit. Additionally, the boundary-layer growth along the two walls may contribute to undesired flow behavior [25]. The axisymmetric nozzle alleviates these problems since the flow is evenly distributed along the tunnel; however, the curved walls in the axisymmetric option may lead to streamwise vortices through a centrifugal instability (Görtler type). This instability is avoided on the flat walls of an asymmetric configuration [26].

Various wind tunnel designs exist depending on application. The “optimum” hypersonic wind tunnel utilizes a blowdown type facility with a uniform velocity distribution in the test section. The blowdown tunnel allows for a continuous flow without a requirement for large amounts of electricity or complicated exhaust systems to handle the exiting flow [2].

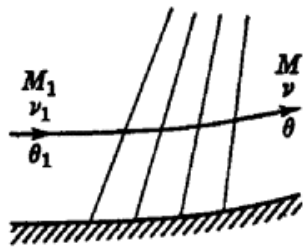
2.2 Method of Characteristics

It is known that an expansion fan or a shock wave forms when supersonic flow encounters a convex or concave turn respectively. Shock waves describe a sharp discontinuity in the flow in which variables such as pressure, temperature, and velocity abruptly change [5]. Shock waves and expansion fans consist of Mach lines, or characteristic lines, that are associated with deceleration or acceleration and turning of the flow [24]. If the flow is supersonic and an upstream Mach number is known, then the downstream flow angle, ϕ , can be found by using the Prandtl-Meyer function, v , provided in (2.1). The flow turning angle is related to v by (2.2) and (2.3) for isentropic compression and expansion, respectively.

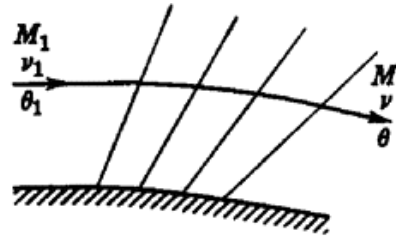
$$v(M) = \int \frac{\sqrt{M^2-1}}{1+\frac{\gamma-1}{2}M^2} \frac{dM}{M} \quad (2.1)$$

$$v = v_1 - |\varphi - \varphi_1| \quad (2.2)$$

$$v = v_1 + |\varphi - \varphi_1| \quad (2.3)$$



(a) Isentropic compression through a turn.



(b) Isentropic expansion through a turn.

Figure 2.3: Isentropic flow as it behaves in compression and expansion [27].

The characteristic lines hold information about the flow along the line, e.g., the Mach angle and the velocity. The Mach angle, μ , is the angle between the flow streamline and a Mach line given as shown in (2.4). Characteristic lines in a region where isentropic expansion and compression can be defined by a single wave are known as *simple waves*. These waves can be characterized by the Prandtl-Meyer function and maintain constant conditions along the wave. Flow with waves sourced from two walls contains what is known as a *nonsimple region* where these characteristic lines intersect. These characteristic lines are called left or right running characteristic lines which are defined by the wall that produces it, i.e., if that wall is to the left or right of the flow. A nonsimple region is where left and right running waves intersect and cannot be determined by (2.1). This region is solved by the method of characteristics. An example of a nonsimple region is displayed in Figure 2.4.

The method of characteristics is based on a relationship between φ and v . The coordinate system used to derive the MOC is converted onto ξ and η for convenience. If one were to solve for the change in ξ and η from P to P^0 shown in Figure 2.5, then one would find a compatibility

relation along the characteristics, given by R and Q in (2.5) and (2.6) [27]. The compatibility relations show that the relation between the velocity magnitude and flow direction is invariant along a characteristic line; hence, R and Q are also known as *Riemann invariants*. (Many textbooks list the compatibility equations as relations between ϕ and μ [6], [24]; however, the values of v or ϕ can be converted into M or μ once a solution is found [27].) The compatibility relations R and Q are constant along the characteristics η and ζ respectively and guarantee that ϕ on the lines are compatible with the momentum equation shown in (2.7) and (2.8) [28]. Equations (2.7) and (2.8) describe the flow for two-dimensional, inviscid, irrotational flow [27]. This knowledge allows flow variables to be calculated at any point in the flow.

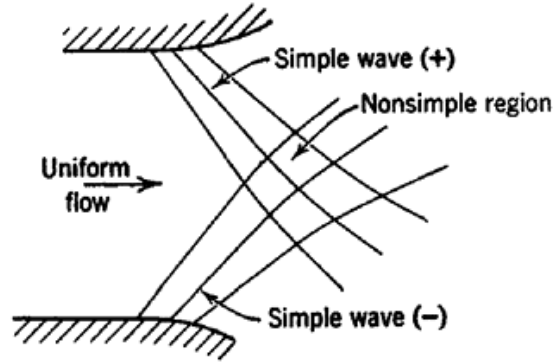


Figure 2.4: Regions of simple waves and nonsimple region [27].

$$\mu = \sin^{-1} \frac{1}{M} \quad (2.4)$$

$$R = \phi - v \quad (2.5)$$

$$Q = \phi + v \quad (2.6)$$

$$(u_1^2 - a^2) \frac{\partial u_1}{\partial x_1} + u_1 u_2 \left(\frac{\partial u_1}{\partial x_2} + \frac{\partial u_2}{\partial x_1} \right) + (u_2^2 - a^2) \frac{\partial u_2}{\partial x_2} = 0 \quad (2.7)$$

$$\frac{\partial u_2}{\partial x_2} - \frac{\partial u_1}{\partial x_2} = 0 \quad (2.8)$$

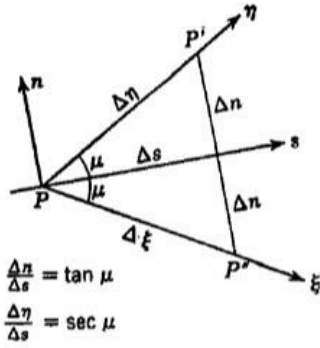


Figure 2.5: Mach angle, μ , along an infinitesimal streamline [27].

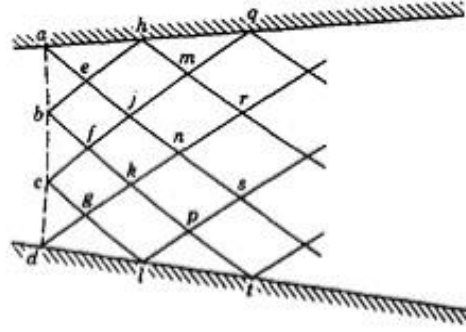


Figure 2.6: Sample mesh in bounded flow for the MOC [27].

The typical method is to create a mesh as shown in Figure 2.6. The angle of the characteristic lines is solved from the initial boundary and variables are found at each point in the mesh, marching downstream. The basic idea is to use information known at two points to solve for the flow parameters at a third intersecting point. For example, say that velocity and flow angles; ϕ_1 , ϕ_2 , v_1 , and v_2 ; are known along intersecting Mach lines. The values at the third point for v_3 and ϕ_3 are determined by relating R and Q on the first two points to Reimann invariants at the third point. The result is seen in (2.9) and (2.10). Flow variables such as temperature and pressure are determined from the known Mach number and isentropic flow relations [27].

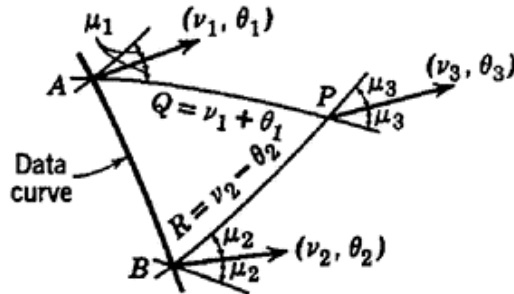


Figure 2.7: Sample of graphical solution to solving for point mesh point downstream of data curve [27].

$$\phi_3 = \frac{1}{2}(Q + R) \quad (2.9)$$

$$v_3 = \frac{1}{2}(Q - R) \quad (2.10)$$

The MOC uses information given to design a nozzle contour by examining the flow variables on each characteristic line, specifically Mach number, μ , and ϕ , to decide the wall angle, ϕ_w . (The maximum ϕ_w is given by the Prandtl-Meyer function.) The contour is designed to reflect the weak expansion waves and prevent strong ones. A contour with a ϕ_w too large will experience a strong shock in the expansion. The sonic surface just downstream of the throat is prescribed, and the calculation marches downstream in a typical supersonic nozzle design calculation. Iteration on the shape of the nozzle wall contour and small meshes in the flowfield is used to achieve the design goals, such as flow uniformity and avoidance of shocks.

2.2.1 Sivells' Computer Program for the Method of Characteristics

Sivells [8] created a computer program in 1978 for the purpose of designing axisymmetric and planar nozzles for wind tunnels. The code was published in his report, "A computer program for the aerodynamic design of axisymmetric and planar nozzles for supersonic and hypersonic wind tunnels," and was written in Fortran 77. The source code was adapted to be used by modern computers and compiled by L.F. Zavalan and A. Rona [29]. Sivells' code was made to be reusable for different wind tunnel applications allowing the user to input key parameters such as the desired Mach number, the inflection angle, and the ratio of the throat radius of curvature to the throat radius. The displacement thickness, for example, can be computed by either Cole's transformation, a modified version of Spalding-Chi's method, or a combination of the two. Each method can assume either a quadratic or parabolic temperature distribution in the boundary-layer [8].

The program is based on advancements of the Foelsch nozzle design. Foelsch simplified Prandtl and Busemann's MOC by assuming the flow is partitioned into three sections within the nozzle as seen in Figure 2.8 [30]:

1. Radial flow, which is upstream of curve AC
2. Flow is converted into parallel stream, bounded by ACD
3. Flow downstream of curve CD is parallel and uniform

Beckwith et al. [25] showed that Foelsch's assumptions had undesirable results. Foelsch's assumption created discontinuities in the contour; therefore, Sivells used the additional assumption made by Beckwith et al. which assumed a fourth region of flow as seen in Figure 2.9: the transition from radial to parallel flow. Sivells' program has been shown to be reliable within an acceptable amount of error [31].

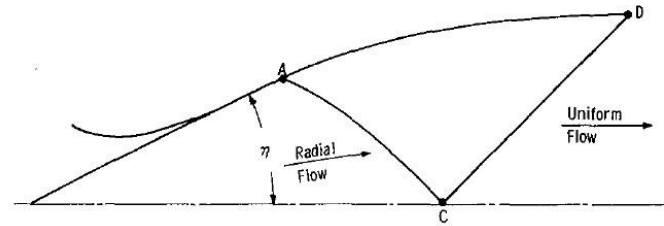


Figure 2.8: Foelsch nozzle design with three flow regions [8].

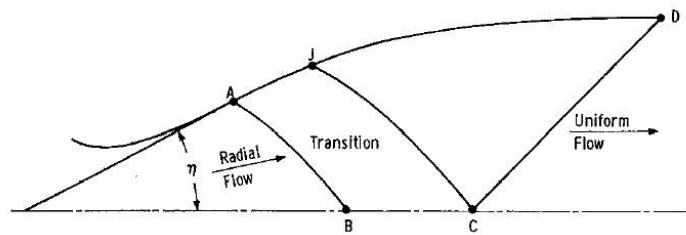


Figure 2.9: Adapted Foelsch nozzle design with transitional flow [8].

Several key features were considered when designing the nozzle contour. These include the boundary-layer growth, transonic solution, and achieving uniform flow at the nozzle exit with a reliable prediction of the Mach number. Sivells' computer program for the MOC implements various methods to accommodate for these requirements. Figure 2.10 describes the process of the code [32]. Each feature will be briefly explained; a thorough description can be found in [8].

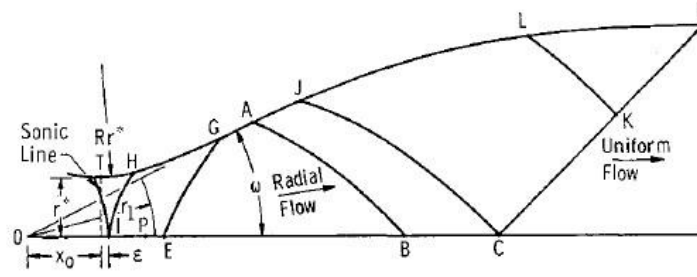


Figure 2.10: Graphic that describes the basic method of Sivells' code. The labeled design points are used for reference [8].

Transonic solution

Basic models for the MOC assume a straight sonic line at the throat. This assumption can affect the nozzle length as mentioned in Section 1.1.1. Sivells' program has the option to include the transonic solution. The solution was formulated based on the work of Hall [33], Kliegel and Levine [34], and Mary et. al [35]. A solution is found for the normal and axial velocity components along the sonic line that is largely dependent on the inverse of RC , the ratio of the radius of curvature at the throat to the throat radius, and is of the form in (2.12) and (2.13) for axisymmetric flow, where y_0 is the throat radius and σ is 0 for planar flow and 1 for axisymmetric flow. It should be noted that the mass flow is reduced by a factor of the discharge coefficient, C_D , as given in (2.15).

$$S_1 = RC + 1 \quad (2.11)$$

$$u = 1 + \frac{1}{4S_1} - \frac{14\gamma-5}{288S_1^2} + \dots \quad (2.12)$$

$$\frac{du}{dx/y_0} = \lambda \left(1 + \frac{7}{8S_1} - \frac{64\gamma^2+117\gamma-1026}{11525S_1^2} + \dots \right) \quad (2.13)$$

$$\lambda = \left(\frac{1+\sigma}{(\gamma-1)S_1} \right)^{1/2} \quad (2.14)$$

$$C_D = 1 + \frac{\gamma+1}{96S_1^2} \left(1 + \frac{8\gamma-27}{24S_1} + \dots \right) \quad (2.15)$$

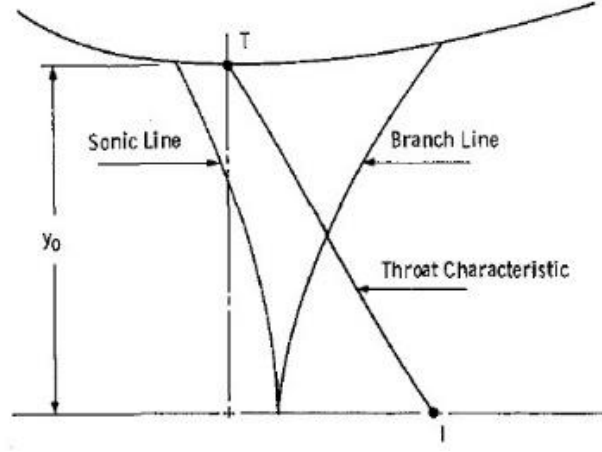


Figure 2.11: Section of a nozzle contour at the throat displaying the sonic line for a transonic solution [8].

Centerline distribution

Defining the Mach distribution along the centerline for axially symmetric flow serves two purposes: to ensure the continuity of the nozzle contour and to provide an immediate calculation of the nozzle length from a calculation. It is desired to maintain continuity of the Mach gradient, dM/dx , and second derivative, d^2M/dx^2 , along the centerline [36]. CONTUR allows the option to define a centerline distribution at various sections of the nozzle. Sivells included the option to define the conical region by radial flow or a centerline distribution. It should be noted that the centerline distribution is initialized with the solution from radial flow defined by (2.16) where D is a coefficient and X is the ratio of distances defined by (2.18). A Mach (or velocity) distribution can be chosen of a different degree polynomial in the form of (2.17). In general, a higher order polynomial distribution is more accurate for higher Mach numbers [37].

$$\left(\frac{r}{r_1}\right)^{1+\sigma} = M^{-1} \left(\frac{2}{\gamma+1} + \frac{\gamma-1}{\gamma+1} M^2 \right)^{\frac{\gamma+1}{2(\gamma-1)}} \quad (2.16)$$

$$M = D_1 + D_2X + D_3X^2 + D_4X^3 + D_5X^4 + D_6X^5 \quad (2.17)$$

$$X = \frac{x-x_B}{x_C-x_B} \quad (2.18)$$

Inviscid contour

An inviscid solution of the nozzle contour is found prior to boundary-layer calculations and contour smoothing. A solution is found from a few characteristic lines: the throat characteristic; the characteristic bounding the radial flow, EG and AB; and characteristic CD as seen in Figure 2.10. The remaining characteristics and flow parameters are then solved propagating downstream. The inviscid solution maintains $\varphi = 0$ at the nozzle exit.

Boundary layer correction

The boundary-layer is assumed to be turbulent for the entire nozzle except for very low stagnation pressures. The momentum thickness, θ , is calculated using the von Karman equation shown in (2.19) for axisymmetric flow. A numerical solution is found by iteration using the new wall radius, r_w , for each iteration. A few methods are included in the program for implementing different correlations of C_f and Re to find a solution: Coles' transformation [12] and a modification of Spalding-Chi (Van Driest) method [38]. The present work used the Spalding-Chi method since its solution is the closest to experimental results [38] and the most conservative (estimates the largest boundary-layer of the options available). The Spalding-Chi correlations are listed in (2.20) and (2.21). The skin friction coefficient is related to the incompressible skin friction coefficient, C_{f_i} ; and the Reynolds number, Re_θ is related to the incompressible Reynolds number, Re_{θ_i} by a factor of F_c and F_{R_δ} respectively. Here, μ_e , ρ_e , and q_e are the viscosity, density and velocity at the boundary-layer edge given at temperature T_e , and ϕ_w and μ_w are the flow angle and viscosity values at the wall. These correlations have a significant effect in the convective heat transfer of the fluid near the wall.

$$\frac{d\theta}{dx} + \theta \left(\frac{2-M^2+H}{M(1+(\gamma-1)M^2/2)} \frac{dM}{dx} + \frac{1}{r_w} \frac{dr_w}{dx} \right) = \frac{C_f}{2} \sec \phi_w \quad (2.19)$$

$$F_c C_f = C_{f_i} \quad (2.20)$$

$$F_{R_\delta} Re_{\theta_c} = Re_{\theta_i} \quad (2.21)$$

$$F_c = \left[\int_0^1 (\rho/\rho_e)^{\frac{1}{2}} d(q/q_e) \right]^{-2} \quad (2.22)$$

$$F_{R_\delta} = \mu_e/\mu_w \quad (2.23)$$

Input Parameters

Sivells created a robust program with 54 user inputs. The key inputs will be covered here – more information on the different inputs can be found in [8]. The original Fortran 77 code used input cards; a sample input card is shown in Figure 2.12. The modernized code was adapted to accept the input of a plain text file with the same spacing; furthermore, a MATLAB wrapper was used to create the text file and automatically populate the parameters.

The first line (Card 1) of the input card includes the name of the job and the option of an axisymmetric or planar nozzle. Card 2 primarily contains the fluid properties. This includes the specific heat ratio, gas constant, and necessary values for Sutherland’s law for viscosity. The turbulent boundary-layer recovery factor, RO , is calculated by (2.24) [39]. The third card contains the main design inputs of the nozzle – specifically the angle of the wall angle at the inflection point, $ETAD$; the ratio of the radius of curvature to the throat radius, RC ; the Mach number at point B , $BMACH$; the Mach number at point C (also the design Mach number), CMC ; the scale factor, SF , which dictates the throat radius or exit radius; and centerline distribution, XC . Card 4 controls the number of characteristic lines computed and distribution of points on the contour. Card 5 controls the smoothing parameters for the inviscid contour. Card 6 dictates the convective heat transfer and boundary-layer effects. Card 7 controls the output points on the contour.

The overall size of the nozzle is dependent on the input parameters on Card 3. A smaller inflection angle will increase the length of the nozzle, but an inflection angle that is too large will cause the code to fail due to the formation of a shock in the flow. The same principle applies to RC – except that the value of RC has a greater impact on the Mach gradient near the throat. The Mach number at point B controls the nozzle length because a smaller Mach number will cause the point to be moved upstream and point C downstream. The ideal values for $BMACH$ are within 75 – 85% of CMC , though larger values are acceptable. The $BMACH$ parameter largely impacts the flow angle at the nozzle exit. All the equations in the source code are nondimensionalized. The parameter SF changes the throat or exit radius (user input) to the corresponding value in inches. The parameter XC is dependent on other parameters, but can permit a 3rd, 4th, or 5th order distribution of the Mach number or velocity on the centerline. The temperature distribution in the nozzle is determined by $ALPH$ and is calculated using (2.25) where T_w is the wall temperature, α is a condition parameter, T_{aw} is the adiabatic wall temperature, T_e is the freestream temperature at the edge of the inviscid contour, u is the velocity, and u_e is the velocity at the edge of the inviscid

contour. The contours were assumed to be adiabatic, thus the adiabatic wall temperature and wall temperature are the same, which simplifies (2.25) to (2.26).

$$r_{turb} = Pr^{1/3} \quad (2.24)$$

$$T = T_w + \alpha(T_{aw} - T_w) \left(\frac{U}{U_e} \right) + [T_e - \alpha(T_{aw} - T_w) - T_w] \left(\frac{U}{U_e} \right)^2 \quad (2.25)$$

$\alpha = 1 \rightarrow$ quadratic distribution

$\alpha = 0 \rightarrow$ parabolic distribution

$$T = T_w + (T_e - T_w) \left(\frac{u}{u_e} \right)^2 \quad (2.26)$$

```

CARD 1
  TITLE      JU
  M A C H 4

CARD 2
  GAM      AH      ZO      RO      VISC      VISM      SFOA      XBL
  1.4      1716.563  1.      0.896  2.26968E-8  198.72      60.      1000.

CARD 3
  8.67      6.      3.      4.      -12.25      60.
  ETAD      RC      FMACH  BMACH  CMC      SF      PP      XC

CARD 4
  MT      NT      IX      IN      IQ      MD      ND      NF      MP      MQ      JB      JX      JC      IT      LR      NX
  41      21      10      41      49      -61      1      10      -21  13

CARD 5
  NOUP      NPCT      NODD
  50      85      50

CARD 6
  PPQ      TO      TWT      TWAT      OFUN      ALPH      IHT      IR      ID      LV
  200.      1638.  900.  540.  .38      1      1      5

CARD 7
  XST      XLOW      XEND      XINC      BJ      XMID      XINC2      CN
  1000.      46.  172.  2.

```

Figure 2.12: Sample inputs for Sivells' computer program [8].

2.3 Mesh Generation

Each mesh was generated using Pointwise®, a commercial grid generation computer program. The mesh quality was measured by the aspect ratio, area ratio (ratio of a cell's area to the adjacent cells), and maximum/minimum included angle. The area ratio was maintained below 1.2 for structured grids and below 5 for unstructured grids. An aspect ratio below 1000 was maintained on all grids. The cells with the highest aspect ratio were located near walls where a small wall spacing was required to resolve the boundary-layer. This initial spacing was determined

by solving for a $\Delta y^+ = 1$ in (2.27) where u_τ is the friction velocity, μ_w is the viscosity at the wall, and Δy is the corresponding distance from the wall [39].

A sponge-layer was created when applicable. A sponge-layer is a region where the grid spacing is made larger to help prevent reflection of sound waves on a boundary. The larger cells allow for dissipation of energy provided the length of the sponge-layer is sufficiently long, which causes incoming waves to be absorbed into the sponge-layer [40].

Structured grids present many advantages, e.g., increased control on grid quality, cell orthogonality, and cell count, and were the preferred method for mesh generation. Unstructured grids were only used when the maximum included angle for an applied structured grid was above 150° . The unstructured grids are able to improve grid quality to accommodate for the complex geometry.

$$\Delta y^+ = \Delta y u_\tau / \mu_w \quad (2.27)$$

$$u_\tau = \sqrt{\tau_w / \rho_w} \quad (2.28)$$

$$\tau_w = \frac{c_f \rho u_\infty}{2} \quad (2.29)$$

2.3.1 Structured Grids

Pointwise® possesses a few grid solvers for structured meshes to aid grid quality. The solvers used for the nozzle implemented Steger-Sorenson's algorithm which ensures orthogonality on a boundary curve and Thomas-Middlecoff which use elliptic equations defined grid points on the boundary to assist in establishing cell spacing in the mesh interior [41]. The elliptic equations allow for interior grid points to be solved locally at each grid point while accounting for the point distribution along the boundary curve. This is accomplished by a grid transformation to the (ξ, η) plane as seen in Figure 2.13. Dirichlet boundary conditions are enforced to solve the Laplace equations created to iterate to a solution [41]. Thomas and Middlecoff proposed the idea of using source terms to cluster grid points at a boundary and promote orthogonality at the boundary [42]. Steger and Sorenson noted that it was difficult to determine of the value of the source terms that could restrict the initial spacing and ensure orthogonality. This issue was addressed by adding

boundary relations to the governing equations. The initial spacing, $\Delta\xi$, was specified at the boundary of η which is shown in (2.30).

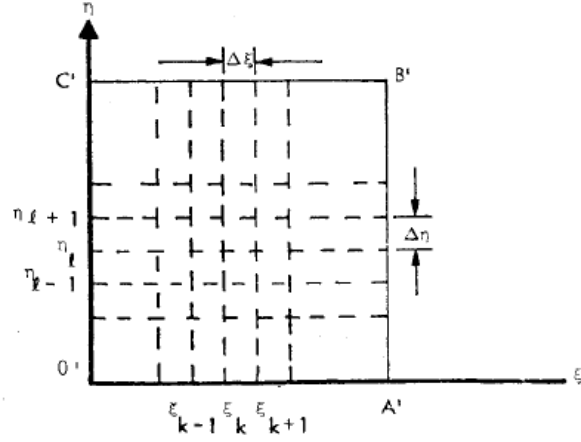


Figure 2.13: Coordinate transformation onto a rectangular (ξ, η) grid.

$$\Delta s = \sqrt{(\Delta x)^2 + (\Delta y)^2} \big|_{\xi=\text{const}} \quad (2.30)$$

$$ds = \sqrt{(dx)^2 + (dy)^2} \quad (2.31)$$

If (2.31) is transformed to the (ξ, η) plane, and since ξ is constant, then

$$ds = \sqrt{(x_\eta)^2 + (y_\eta)^2} d\eta \quad (2.32)$$

Orthogonal grid lines are enforced by equating to the dot product between ξ and η to zero [42].

2.3.2 Unstructured Grids

Unstructured grids were used to accommodate for the high sweep angle of the missile fins. Unstructured grids are highly dependent on automation; therefore, in order to achieve a high-quality grid, several iterations may be required. Pointwise® can use hybrid meshing algorithms that can minimize the number of unstructured cells (i.e., cells that are not hexahedral). The same

method is used for two-dimensional and three-dimensional grids. Triangular cells (in 2D) are created and then merged to form quadrilaterals when possible. The specific algorithm used is known as *Advancing Front Ortho* which creates right triangles that propagate from the boundaries and combine into quadrilateral elements. The size of a cell is determined by the edge length on the boundary. Pointwise® has the capability to control the growth from selected boundary curves with an algorithm known as *Trex* (anisotropic tetrahedral extrusion). The *Trex* algorithm first extrudes points normal to the boundary at a specified growth rate. These points are checked to ensure they do not collide with another extrusion front. The points are connected to the adjacent cells and the process repeats until the specified number of layers are met or cells become isotropic, and hence failing the collision test. The remaining cells are created using the selected algorithm (Advancing Front Ortho in 2D and Delaunay in 3D for this project). The *Trex* meshing was advantageous for controlling 2D grid spacing on the surface near areas of high surface curvature and face boundaries and adding a prism layer to resolve the boundary-layer [43]. The surface boundaries of the resulting *Trex* mesh were then algebraically extruded to accompany various incoming angles of attack on the flowfield.

2.4 Computational Fluid Dynamics (CFD) Code Configuration

Different CFD programs were used based on access and necessity. The codes used include SU2 and Kestrel. All CFD programs described were used in the simulation of the high enthalpy test facility. The simulations conducted on the hypersonic missiles were performed using Kestrel. Steady-state computations performed in Kestrel were completed on supersonic and hypersonic nozzles and two missile configurations (conical and ogive) at various angles of attack. The convergence of Reynold's-averaged Navier-Stokes (RANS) simulations was determined by examining the skin friction coefficient, which is highly sensitive to convergence and may continue to change after the residuals seem to converge. The schemes and methods used within each program are described in this section; specific input parameters are described in the following chapters.

2.4.1 SU2

SU2 (Stanford University Unstructured) is an open-source, numerical partial differential equations (PDEs) solver for unstructured meshes. The main source code is written in C++, and it references several Python scripts. The primary solver utilizes a (RANS) solver with the capability of simulating viscous supersonic and hypersonic compressible flow [44]. SU2 has shown reliability in simulating compressible flow within nozzles as shown in [45]. SU2 has the option to implement various numerical schemes to accommodate different purposes in order to solve convective and viscous fluxes. The SU2 RANS solver can account for turbulent effects with either the Spalart-Allmaras (SA) model, Menter shear stress transport (SST) model, or variations of the two. The simulations presented here used version 7.0.4.

The general formulation for steady-state compressible flow in SU2 is given by (2.33) where \mathbf{U} is a vector of the conservative variables, $\vec{\mathbf{F}}^c$ is the convective fluxes, and $\vec{\mathbf{F}}^v$ is the viscous fluxes given in (2.34); and \mathbf{Q} is a generic source term. E is the energy per unit mass, u_i indicates the flow velocity in a Cartesian coordinate system, H is the total enthalpy, and τ_{ij} is the viscous stress as given in (2.36). The turbulent and molecular viscosities and conductivities are summed into one term, μ_{tot} and k_{tot} , to provide the total viscosity and total conductivity respectively [46].

$$\frac{\partial \mathbf{U}}{\partial t} + \nabla \cdot \vec{\mathbf{F}}^c - \nabla \cdot \vec{\mathbf{F}}^v = \mathbf{Q} \quad (2.33)$$

$$\mathbf{U} = \begin{pmatrix} \rho \\ \rho u_1 \\ \rho u_2 \\ \rho u_3 \\ \rho E \end{pmatrix}, \quad \vec{\mathbf{F}}_i^c = \begin{pmatrix} \rho u_i \\ \rho u_i u_1 + P \delta_{i1} \\ \rho u_i u_2 + P \delta_{i2} \\ \rho u_i u_3 + P \delta_{i3} \\ \rho u_i H \end{pmatrix}, \quad \vec{\mathbf{F}}_i^v = \begin{pmatrix} \tau_{i1} \\ \tau_{i2} \\ \tau_{i3} \\ u_j \tau_{ij} + k_{tot} \partial_i T \end{pmatrix}, \quad i = 1, \dots, 3. \quad (2.34)$$

$$\mathbf{Q} = \begin{pmatrix} q_\rho \\ q_{\rho u_1} \\ q_{\rho u_2} \\ q_{\rho u_3} \\ q_{\rho E} \end{pmatrix} \quad (2.35)$$

$$\tau_{ij} = \mu_{tot} \left(\partial_j u_i + \partial_i u_j - \frac{2}{3} \delta_{ij} \nabla \cdot \vec{v} \right) \quad (2.36)$$

SU2 calculates the viscous boundary-layer by splitting the viscosity into a laminar viscosity, μ , and a turbulent viscosity, μ_t . SU2 assumes that μ adheres to Sutherland's law [44].

The μ_t is calculated using turbulence models. The present work used the shear-stress transport (SST) turbulence model.

The SST model is a two-equation model which considers the traditional $k - \omega$ and $k - \epsilon$ models, where ω is the specific turbulent dissipation, or turbulence frequency, and ϵ is turbulent dissipation. Menter recognized the inadequacies of both two-equation models: $k - \omega$ models had reasonable results in the viscous sublayer and were more sensitive to adverse pressure gradients than $k - \epsilon$ models but were highly dependent on the freestream values of ω , and $k - \epsilon$ models were reasonably sufficient with free-shear layers but had a tendency to over-predict the skin friction and thus delayed separation [47]. The SST model attempts to utilize the formulation of the $k - \omega$ model in the viscous sublayer and the independence of the $k - \epsilon$ model in the region around the outer layer of the boundary-layer by using a blending function, F_1 , to control the effects of the equations within the boundary-layer. Menter transformed the $k - \epsilon$ model into a modified $k - \omega$ formulation shown in (2.37) and (2.38).

$$\frac{\partial \rho k}{\partial t} + \frac{\partial \rho u_j k}{\partial x_j} = P_k - \beta^* \rho \omega k + \frac{\partial}{\partial x_j} \left[(\mu + \sigma_k \mu_t) \frac{\partial k}{\partial x_j} \right] \quad (2.37)$$

$$\frac{\partial \rho \omega}{\partial t} + \frac{\partial \rho u_j \omega}{\partial x_j} = \gamma P_\omega - \beta \rho \omega^2 + 2(1 - F_1) \sigma_\omega 2 \frac{\mu_t}{k} \frac{\partial k}{\partial x_j} \frac{\partial \omega}{\partial x_j} + \frac{\partial}{\partial x_j} \left[(\mu + \sigma_\omega \mu_t) \frac{\partial \omega}{\partial x_j} \right] \quad (2.38)$$

$$P_k = \mu_t \frac{\partial u_i}{\partial x_j} \left(\frac{\partial u_i}{\partial x_j} + \frac{\partial u_j}{\partial x_i} \right) - \frac{2}{3} \rho k \delta_{ij} \frac{\partial u_i}{\partial x_j} \quad (2.39)$$

$$P_\omega = \rho \frac{\partial u_i}{\partial x_j} \left(\frac{\partial u_i}{\partial x_j} + \frac{\partial u_j}{\partial x_i} \right) - \frac{2}{3} \rho \omega \delta_{ij} \frac{\partial u_i}{\partial x_j} \quad (2.40)$$

The SST model has proven to accurately predict the flowfield in response to an adverse pressure gradient, providing a more accurate solution for the pressure distribution and boundary-layer [47]. The SST model additionally provides better accuracy for turbulent heat transfer as opposed to one-equation models [48].

The model was computed using an implicit Euler time discretization and a first order upwind scheme. The nature of the problem was hypersonic flow, which generally require upwind schemes to carry flow information downstream and readily predict flow around discontinuities such as shocks [49], whereas central differencing schemes often display oscillations in regions with a severe pressure gradient [50]. Upwinding is generally more stable in hypersonic flow since

it does not rely on information from outside of the domain. The Advection Upstream Splitting Method (AUSM) was used for simulations performed in SU2. The AUSM scheme uses the formulation shown in (2.41) for a two-dimensional Euler equation assuming a perfect gas where \mathbf{U} contains the state variables and \mathbf{F} and \mathbf{G} are the inviscid fluxes given in (2.42).

$$\frac{\partial \mathbf{U}}{\partial t} + \frac{\partial \mathbf{F}}{\partial x_i} + \frac{\partial \mathbf{G}}{\partial x_j} = 0 \quad (2.41)$$

$$\mathbf{U} = \begin{pmatrix} \rho \\ \rho u_1 \\ \rho u_2 \\ \rho E \end{pmatrix}, \quad \mathbf{F} = \begin{pmatrix} \rho u_1 \\ \rho u_1^2 + P \\ \rho u_1 u_2 \\ \rho u_1 H \end{pmatrix}, \quad \mathbf{G} = \begin{pmatrix} \rho u_2 \\ \rho u_2 u_1 \\ \rho u_2^2 + P \\ \rho u_2 H \end{pmatrix} \quad (2.42)$$

The AUSM scheme separates \mathbf{F} and \mathbf{G} into convective and pressure terms. This process conveniently allows the scalar quantities to be passively defined by u_i . The pressure term is determined by using information on acoustic waves (following a general procedure of the MOC). This method retains the simplicity and efficiency of flux-vector splitting schemes while achieving the accuracy of flux-difference splitting schemes [51].

The Green-Gauss method was selected for calculating spatial gradients. SU2 uses the Green-Gauss method to average the flow variables at the nodes to find the gradients at the cell faces [44]. The Green-Gauss method has been proven to provide better results than other options such as the Least-Squares method when boundary-layer calculations are considered [52].

The transport equation is solved using the Flexible Generalized Minimum Residual (FGMRES) linear solver using a lower-upper symmetric Gauss-Seidel (LU-SGS) preconditioner and a van-Albada-edge slope limiter. The FGMRES solver is a modification of the Generalized Minimum Residual (GMRES) method and is typically more stable and converges faster [53]. The GMRES solver is an iterative method for solving large, sparse asymmetric matrices [54]. SU2 utilizes the preconditioner to accelerate and stabilize convergence [50]. The van-Albada-edge slope limiter and LU-SGS preconditioner were more stable than other options available in SU2.

SU2 contains several key input parameters to describe the flowfield. The relevant input parameters that are dependent on the boundary conditions are pressure, temperature, and velocity (or Mach number). The nozzle was simulated with the compressible, axisymmetric solver in SU2. The simulations run in SU2 assumed an ideal gas to simplify computations. An adiabatic wall assumption for the nozzle simulations provided a conservative estimate to the flow since the wall

is forced to be the same temperature as the local gas (assuming a constant temperature would remove heat from the flow and thus reduce the thermal boundary-layer thickness). Thermal conductivities (laminar and turbulent), thermal diffusivity, γ , and μ are not dependent on the boundary conditions. The SU2 version used maintains a constant γ and thermal diffusivity through the simulation. SU2 implemented constant laminar and turbulent Prandtl numbers to solve for the thermal respective thermal conductivities. The molecular viscosity is solved with Sutherland's law to accommodate for temperature affects in the flow defined by (2.43) where the subscript *ref* indicates a reference value and S is Sutherland's constant [55].

$$\frac{\mu}{\mu_{ref}} = \left(\frac{T}{T_{ref}} \right)^{\frac{3}{2}} \frac{T_{ref} + S}{T + S} \quad (2.43)$$

It is worth noting that, during the simulation, the input freestream values only affect a farfield boundary condition that is used as a flow inlet, which is defined by the flow vector. The flowfield is extrapolated in the event the exit boundary condition is set to farfield. The freestream values do, however, affect the non-dimensional values, e.g., C_f and Δy^+ . SU2 determines the magnitude of the non-dimensional terms using the input freestream values rather than a local value, that is, the resulting freestream value normal to the wall. The values may be considered useful when considering convergence – if an incorrect magnitude of the skin friction coefficient is displayed, then the consistency of the magnitude between iterations of a steady state simulation can determine convergence of a solution.

2.4.2 CREATE Kestrel

The CREATE Kestrel is a physics flow solver which contains packages that aid CFD simulations. The main CFD source code is the Kestrel CFD solver (KCFD). The present work used version 10.4.1rc3 for nozzle simulations and 11.1rc5 for missile simulations. The KCFD solver is an unstructured, cell-centered, finite-volume solver for two-dimensional and three-dimensional flows [56]. Kestrel uses the Method of Lines (MOL) to separate the temporal and spatial schemes. The MOL breaks down the spatial terms in a PDE by replacing the derivatives with algebraic approximations, leaving a system of ODE's [57]. The gradients are computed using

the Godunov based schemes using exact or approximate Riemann methods with a Green-Gauss scheme. The Gauss-Seidel method is used for solving linear equations.

Kestrel was created with an emphasis on simulation stability to prevent divergence and promote ease of use for new users, but also contains additional flow solver options for advanced users [56]. This stability is accomplished by adding advection damping terms on the diagonal of the left-hand side matrix of the governing equations. Although the additional terms may improve the stability of a simulation, a damping term with a large magnitude can slow the convergence of steady-state problems and reduce the accuracy of unsteady simulations [56]. Kestrel provides the option to select different schemes to solve for turbulence, inviscid flux, viscous flux, and temporal flux. The turbulence models considered were the Spalart-Allmaras (SA) model and the SST model. Refer to Section 2.4.1 for a description of the SST model. In general, one-equation models perform better in external flow and two-equation models perform better in internal flow. Thus, the SA model was used for simulations on the missile-fin configurations and the SST model was used in the nozzle flow simulations. The quadratic constitutive relation (QCR) model was used in conjunction with SST to replace the linear Boussinesq hypothesis to improve the RANS turbulence model [56].

A one-equation Menter transition model (known as the γ -model) was used in conjunction with the SST model for nozzle simulations. There are several mechanisms that can cause transition. The γ -model is a Galilean invariant method that utilizes turbulent intermittency to model regions of transition [58]. A Galilean invariant model is not affected by movement of the grid. Though Galilean invariance is not required for this research, it is important in general CFD applications where the mesh is in motion. The formulation uses a source terms to identify transition points and encourage re-laminarization shown in (2.45) and (2.46) that are fed into the transport equation (2.44) where γ is the turbulent intermittency, S is the strain rate, P_γ is the transition source term, E_γ is the destruction source term, Ω is the vorticity rate magnitude, c_{a2} , c_{e2} , σ_γ , and F_{length} are constants, and F_{onset} is function that activates E_γ . The transition source term is designed to maintain the laminar boundary-layer upstream of transition until the transition criteria is met. The destruction term encourages laminarization of transitional and turbulent flow.

$$\frac{\partial(\rho\gamma)}{\partial t} + \frac{\partial(\rho U_j \gamma)}{\partial x_j} = P_\gamma - E_\gamma + \frac{\partial}{\partial x_j} \left[\left(\mu + \frac{\mu_t}{\sigma_\gamma} \right) \frac{\partial \gamma}{\partial x_j} \right] \quad (2.44)$$

$$P_\gamma = F_{length}\rho|S|(1 - \gamma)F_{onset} \quad (2.45)$$

$$E_\gamma = c_{a2}\rho\Omega\gamma F_{turb}(c_{e2}\gamma - 1) \quad (2.46)$$

The Spalart-Allmaras model is a one-equation turbulence model which solves for the eddy viscosity. The SA model adapts to near-wall and free-shear flows by blending a viscous sublayer to a logarithmic formulation based on y^+ . The model uses the scaled eddy viscosity, $\tilde{\nu}$, as a working variable which is solved using (2.47) where \tilde{S} is given by (2.48); ν is the kinematic viscosity; c_{b1} , c_{b2} , and c_{w1} are constants; Pr_t is the turbulent Prandtl number; d is the minimum distance from the field point to the nearest grid line; k is the turbulent kinetic energy; and f_w and f_{t2} are control functions. The scaled eddy viscosity is given by (2.49). The SA model contains a production term which contains the constant c_{b1} , a diffusion term containing the constant c_{b2} , and a destructive term containing the constant, c_{w1} . Each constant was calibrated via experimental comparison [59].

$$\frac{D\tilde{\nu}}{Dt} = c_{b1}[1 - f_{t2}]\tilde{S}\tilde{\nu} + \frac{1}{Pr_t}[\nabla \cdot ((\nu + \tilde{\nu})\nabla\tilde{\nu}) + c_{b2}(\nabla\tilde{\nu})^2] - [c_{w1}f_w - \frac{c_{b1}}{k^2}f_{t2}] \left[\frac{\tilde{\nu}}{d}\right]^2 \quad (2.47)$$

$$\tilde{S} = \Omega + \frac{\tilde{\nu}}{k^2 d^2} f_{v2}, \quad f_{v2} = 1 - \frac{\chi}{1 + \chi f_{v1}} \quad (2.48)$$

$$\mu_t = \tilde{\nu} f_{v1}, \quad f_{v1} = \frac{\chi^3}{\chi^3 + c_{v1}^3}, \quad \chi = \frac{\tilde{\nu}}{\nu} \quad (2.49)$$

The SA model has consistently proven to provide accurate results with the advantage of the simplicity of a one-equation model; however, the model has a difficulty resolving flow in an adverse pressure gradient – particularly after a shock [59].

The Harten–Lax–van Leer (HLL), an improved Harten, Lax, van Leer and Einfeldt (HLLE+), and LDD+ schemes were selected to solve the convective, inviscid, and viscous fluxes respectively using a Venkatakrishnan flux limiter. The HLL scheme is an approximate Riemann solver which assumes that an intermediate state exists between the fastest and slowest characteristic waves in a local domain [60]. This state is used as an approximate solution to the Riemann problem which has proven to be consistent to the exact solution of the conservation laws [61]. The HLL scheme has proven to be dissipative in regions where discontinuities exist and

cannot resolve contact discontinuities [60], thus the scheme is only implemented for the inviscid fluxes. A complete derivation of the HLL scheme can be found in [62]. The HLLE+ scheme is an extension of the HLLE scheme (which was based on the HLL scheme). The HLLE+ scheme has proven to resolve sharp discontinuities such as normal shocks and provide satisfactory results for a boundary-layer solution [63]. The HLLE+ scheme controls the diffusion by using an anti-diffusion coefficient. This coefficient is controlled by analysis of the pressure gradient term which increases or reduces the coefficient in the vicinity of discontinuities and high viscous interactions; additionally, the control of the anti-diffusion term improved stability and accuracy around discontinuous flow and removed erroneous features such as carbuncles that were present in the solutions of previous HLL related schemes [63]. The Venkatakrishnan slope limiter is an evolution of the Beth and Jespersen limiter that promotes convergence as a relatively easy addition to the flux schemes [64] and is typically provides a smoother solution when compared to Beth and Jespersen but loses the ability to enforce monotonicity and has difficulty resolving boundary-layers [65].

Real gas models were used in the steady-state simulations of the hypersonic missile. The gas was specified as a mixture in chemical non-equilibrium which opts to solve transport equations based on the Arrhenius equation in (2.50) where k_i is the reaction rate for the i^{th} reaction, A_i is the pre-exponential factor, β_i is the temperature exponent, and T_{act_i} is the activation temperature described in (2.51) where E_i is the activation energy. Five species were selected for the model: N_2 , O_2 , O , N , and NO (with M used to indicate a third-body reaction) and a starting species mass fractions of 0.767, 0.233, 0.0, 0.0, and 0.0 respectively. The reaction mechanism is based on the Park model (a pre-defined model in Kestrel) and is described in Table 2.1.

$$k_i = A_i T^{\beta_i} \exp\left(-\frac{T_{act_i}}{T}\right) \quad (2.50)$$

$$T_{act_i} = \frac{E_i}{R_c} \quad (2.51)$$

Table 2.1: Reaction mechanism for real gas using Kestrel’s predefined 5-species air. Units are in *cm*, *g*, *s*, and *K*.

Reaction	A_i	β_i	T_{act_i}	Third Body Efficiencies
$O_2(+M) \rightarrow 2O(+M)$	$2.9e23$	-2.0	$5.975e4$	$N_2: 0.0, N: 1.0, O_2: 0.0, O: 1.0, NO: 0.0$
$O_2(+M) \rightarrow 2O(+M)$	$9.68e22$	-2.0	$5.975e4$	$N_2: 1.0, N: 0.0, O_2: 1.0, O: 0.0, NO: 1.0$
$N_2 + N \rightarrow 3N$	$1.6e22$	-1.6	$1.132e5$	
$N_2 + O \rightarrow 2N + O$	$4.98e22$	-1.6	$1.132e5$	
$N_2(+M) \rightarrow 2N(+M)$	$3.7e21$	-1.6	$1.132e5$	$N_2: 1.0, N: 0.0, O_2: 1.0, O: 0.0, NO: 0.0$
$N_2 + NO \rightarrow 2N + NO$	$4.98e21$	-1.6	$1.132e5$	
$NO(+M) \rightarrow N + O(+M)$	$7.95e23$	-2.0	$7.55e4$	$N_2: 1.0, N: 1.0, O_2: 1.0, O: 1.0, NO: 1.0$
$NO + O \rightarrow N + O_2$	$8.37e12$	0.0	$1.945e4$	
$N_2 + O \rightarrow N + NO$	$6.44e17$	-1.0	$3.837e4$	

2.5 Thermochemistry modeling

Nitrous oxide may decompose exothermically or endothermically following the global reactions (2.52) and (2.53) respectively. The full reaction mechanism is given in Table 2.2 and has been documented in Röhrig et al. [66]. The mechanism was modeled using ANSYS Chemkin-Pro.



Table 2.2: Kinetic reaction mechanism for thermal decomposition of N_2O . Units are in cm^3 , mole, and kJ.

	A_i	β_i	E_i
1. $N_2O = N_2 + O$	1.258E12	0.0	262.0
2. $N_2O + O = N_2 + O_2$	1.0E14	0.0	117.2
3. $N_2O + O = 2NO$	6.92E13	0.0	111.4
4. $NO + M = N + O + M$	9.64E14	0.0	620.9
5. $NO + O = N + O_2$	1.13E12	1.0	173.2
6. $NO_2 + O = NO + O_2$	3.92E12	0.0	-0.996
7. $NO_2 + M = NO + O + M$ (high-pressure limit)	1.4E14	0.0	296.9
(low-pressure limit)	4.0E16	0.0	293.3
8. $O_2 + M = 2O + M$	6.08E15	-1.0	494.4
9. $NO_3 + M = NO_2 + O + M$ (high-pressure limit)	2.2E15	0.0	207.2
(low-pressure limit)	1.0E18	0.0	200.3

Prior to any thermochemistry modeling, the user must provide thermodynamic data of each of the species involved in the reactions. A file included with the Chemkin installation contained the thermodynamic polynomial coefficients for the species used. Chemkin calculates reaction rates using the Arrhenius equation for a forward reaction. The seventh and ninth reactions are considered unimolecular/recombination fall-off reactions which are characterized using Lindemann's expression of low- and high-pressure limits. The reaction rate of this fall-off reaction is dependent on temperature and pressure. Different reaction rate expressions are formed as shown in (2.54) and (2.55) where the subscripts "0" and " ∞ " denote the low and high-pressure reactions respectively. Lindemann's equation is used to calculate the rate constant at any pressure with (2.56) where P_{red} is the reduced pressure given by (2.57) where $[M]$ is the concentration of the mixture [67].

$$k_0 = A_0 T^{\beta_0} \exp(-E_0/R_c T) \quad (2.54)$$

$$k_\infty = A_\infty T^{\beta_\infty} \exp(-E_\infty/R_c T) \quad (2.55)$$

$$k = k_\infty \left(\frac{P_{red}}{1 + P_{red}} \right) \quad (2.56)$$

$$P_{red} = \frac{k_0 [M]}{k_\infty} \quad (2.57)$$

The thermal decomposition of N_2O was modeled in Chemkin using a plug flow reactor (PFR). The PFR is a natural choice for testing thermochemical reactions in a continuous flow. A PFR assumes that flow does not mix in the axial direction – only the traverse direction [67]. This assumption allows the achievement of the maximum allowed reactant conversion. Chemkin models a PFR with simplified version of the conservation equations that are reduced to first-order ODE's [67]. The conservation of mass, energy, and momentum in a PFR are described in (2.58), (2.59), and (2.60) respectively. Here K_g is the number of species, W_k is the molecular weight of species k , \dot{s}_k is the molar production rate of k species by all surface reactions, A is the cross-sectional flow area, $a_{i,m}$ is the effective internal surface area per unit length of material m , Y_k is the mass fraction, h_k is the specific enthalpy of species k , \bar{C}_p is the mean heat capacity per unit mass, Q_e is the heat flux from the surroundings to the outer wall, and F is drag force exerted from the wall to the gas [67].

$$\rho u \frac{dA}{dx} + \rho A \frac{du}{dx} + uA \frac{d\rho}{dx} = \sum_{m=1}^M a_{i,m} \sum_{k=1}^{K_g} \dot{s}_{k,m} W_k \quad (2.58)$$

$$\begin{aligned} \rho u A \left(\sum_{k=1}^{K_g} h_k \frac{dY_k}{dx} + \bar{C}_p \frac{dT}{dx} + u \frac{du}{dx} \right) + \left(\sum_{k=1}^{K_g} h_k Y_k + \frac{1}{2} u^2 \right) \sum_{m=1}^M a_{i,m} \sum_{k=1}^{K_g} \dot{s}_{k,m} W_k = \\ a_e Q_e \sum_{m=1}^M a_{i,m} \sum_{k=1}^{K_g} \dot{s}_{k,m} W_k h_k \end{aligned} \quad (2.59)$$

$$A \frac{dP}{dx} + \rho u A \frac{du}{dx} + \frac{dF}{dx} + u \sum_{m=1}^M a_{i,m} \sum_{k=1}^{K_g} \dot{s}_{k,m} W_k = 0 \quad (2.60)$$

Since the mechanism modeled does not include surface reactions, the governing equations can be further reduced by removing all terms with \dot{s}_k :

$$\rho u \frac{dA}{dx} + \rho A \frac{du}{dx} + uA \frac{d\rho}{dx} = 0 \quad (2.61)$$

$$\rho u A \left(\sum_{k=1}^{K_g} h_k \frac{dY_k}{dx} + \bar{C}_p \frac{dT}{dx} + u \frac{du}{dx} \right) = 0 \quad (2.62)$$

$$A \frac{dP}{dx} + \rho u A \frac{du}{dx} + \frac{dF}{dx} = 0 \quad (2.63)$$

Chemkin provides several options that dictate how the governing equations are solved in a PFR – most of which are available as to simplify the model if applicable. All governing equations were solved (there exists a feature in Chemkin that turns off the momentum equation calculation and/or assumes isothermal flow throughout the reactor).

3. HIGH ENTHALPY HYPERSONIC TEST FACILITY

Several methods were considered for the nozzle design. The method selected, CONTUR, used the method of characteristics to create an inviscid flow design and boundary-layer transformation equations to create a viscous flow design from the inviscid nozzle. Several iterations were performed to establish a procedure for designing a hypersonic nozzle. Initial iterations were simulated with SU2 and more recent iterations with Kestrel. There were several elements to consider – some of which were determined by trial and error. All simulations assumed an ideal gas in 2D-axisymmetric flow. Initial properties of the gas along the nozzle centerline were obtained from a CEA calculation performed by Utkarsh Pandey. Iterations progressed from defining a nozzle geometry to attain the correct exit Mach number to establishing a nozzle with an acceptable length. Two nozzle contours are presented: a Mach 6.13 nozzle and a Mach 3.64 nozzle. The Mach 6.13 nozzle is simulated using a mixture of N_2 and O_2 gas. The Mach 3.64 nozzle is simulated using cold N_2 gas. The latest simulation compares CFD computations to experimental results to aid the process validation.

3.1 CONTUR

The nozzle design began with Sivells' CONTUR program. Several iterations of the program were required before a contour was selected. A MATLAB script was created as a wrapper to supply inputs to CONTUR (see APPENDIX C: MATLAB wrapper for Sivells' MOC computer program for code). This wrapper automated the generation of a text file that could be used to supply the "cards" needed for CONTUR. An example of the inputs used for the Mach 6.13 and Mach 4 nozzle are shown in Figure 3.1 and Figure 3.2 (see APPENDIX B: Description of input parameters to CONTUR for description of each input parameter). The values correspond to the respective variable locations. A blank value in Figure 3.2 corresponds to a 0 value. All configurations assume ideal gas, a turbulent Prandtl number of 0.9 [39], adiabatic flow, and an average γ between the nozzle throat and nozzle exit as calculated by NASA's Chemical Equilibrium with Applications (CEA) code. The values for Sutherland's law for viscosity were acquired from a curve fit from a CEA calculation of viscosity for a gas mixture of O_2 and N_2 and

from [39] for N_2 gas. Assumptions were made for the throat wall temperature and exit wall temperature based on experience.

```

MACH 6      0
1.3448      1692.3      1.      0.89      8.3338E-7      0.      0      1000.
6.0         6.0         0         4.8         6.13         -4.      0.      0
61  41      0      10      0      41      49      -61      0      0      1      0      0      0      -21      13
50  85      50
524.8336    3427.9      2500.      540.      0.      0      0      0      1      5
1000.       5.         0.         .01      0      0      0      0      0

```

Figure 3.1: Sample input parameters for a Mach 6.13 nozzle with high temperature gas mixture of N_2 and O_2 .

```

MACH 4      0
1.3504      1720.0      1.      0.904      2.5144E-08      252.5979      0      1000.
10.6        11.1        0         3.208      4.01         -1.9        0.0        1
41  71      0      10      0      51      49      -41      0      0      1      0      -10      0      -41      13
50  85      50
500.0       536.4       550.0      175.00      0.         0         0      1      1      5
1000.       0.         0.         0.0        0         0         0      0      0

```

Figure 3.2: Sample input parameters used for design of Mach 4 nozzle for cold N_2 gas.

Different viscosities of the gas mixture were computed by CEA at temperatures 273 K and 300 K to 2500 K every 0.5 K. The viscosity was plotted against the temperature in MATLAB as a target. Constants used in Sutherland's law were computed numerically – this is accomplished by calculating viscosity with an initial guess of the Sutherland's constant, estimating a polynomial curve with the *fit* command in MATLAB with the initial guess, and comparing it to the baseline curve. If the estimated curve did not meet the convergence criteria, the guess was altered until the relative error was less than 0.01 or 150 iterations were reached. The converged curve-fit to estimate Sutherland's constant for the gas mixture is shown in Figure 3.3 with the resulting coefficients in Table 3.1 where C is a constant in (3.1) and (3.2).

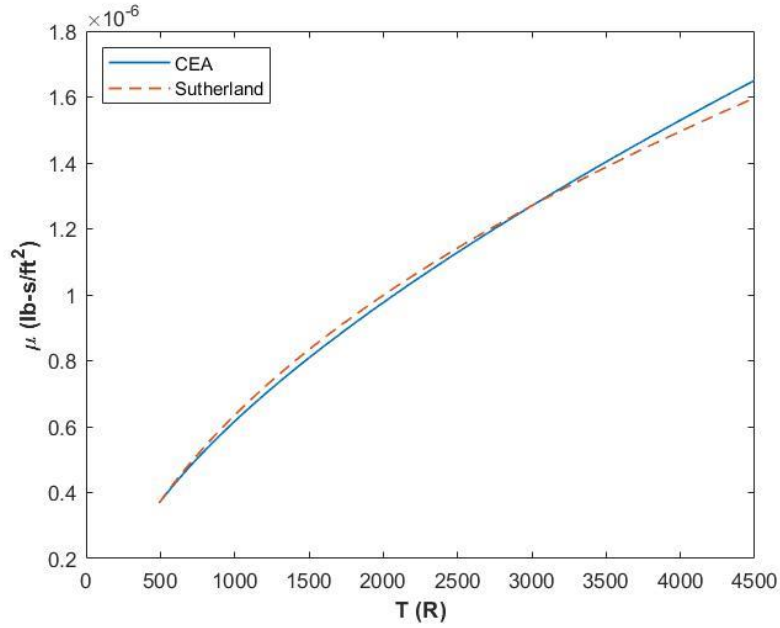


Figure 3.3: Curve fit to estimate Sutherland's constant for a N_2 - O_2 gas mixture. The blue curve traces the data supplied by CEA. The dashed, red curve is the polynomial fit estimated by MATLAB using a solution for Sutherland's constant.

$$\mu = \frac{(C*T^{3/2})}{T+S} \quad (3.1)$$

$$C = \frac{\mu_{ref}}{T_{ref}^{1.5}} \times (T_{ref} + S) \quad (3.2)$$

Table 3.1: Values to estimate viscosity of an N_2 - O_2 gas mixture using Sutherland's law of viscosity.

μ_{ref}	$3.68E - 07 \frac{lb*s}{ft^2}$
T_{ref}	$491.4 \text{ } ^\circ R$
S	$252.6 \text{ } ^\circ R$
C	$2.51E - 08$

The main input parameters considered for the inviscid nozzle were the design Mach number, inflection angle, and throat radius of curvature. The parameters on card 6 have the largest impact on the viscous flow geometry and dimensions. This card determines the transformation method which accommodates for the displacement thickness, the temperature distribution calculation, and the heat transfer from the wall. The modification of Spalding-Chi was selected for the inviscid to viscous flow calculation, a quadratic distribution was selected to calculate the temperature distribution, and the wall was assumed to be adiabatic. The stagnation pressure and temperature were calculated from isentropic relations to match a back pressure equal to the atmospheric pressure at 95,000 feet. Longer nozzles promoted stability in the code – conditions that resulted in a diverging solution or invalid geometry either entered an infinite loop or neglected to display the nozzle coordinates in the output file. (In the event of an infinite loop, the program must be forced to exit, which can be done within MATLAB.) The runs with the best solutions provided coordinates to the inviscid and viscous flow contours. (Note: the option to view coordinates of the inviscid and viscous flow geometries must be selected in the input cards.) The design Mach number, inflection angle, throat radius of curvature, and *BMACH* had the largest impact on the contour geometry. Shorter nozzles had a higher Mach gradient which may allow discontinuities to exist in the flow; however, longer nozzles displayed a large boundary-layer which caused the maximum Mach number to exist before the nozzle exit. In addition, longer nozzles would require more materials and space to construct. Trial and error were required before a suitable nozzle geometry could be used. The general trend of select inputs from card 2 for CONTUR are as follows:

- Increased nozzle length with increased design Mach number
- Increased nozzle length with lower inflection angle
- Increased nozzle length with lower throat radius of curvature

The primary input parameters used to create the Mach 6.13 and Mach 4 nozzles are listed in Table 3.2. The main output parameters that were monitored were the nozzle length and the Mach gradient. The author found that it was best to maintain a Mach gradient at or below one to avoid discontinuities within the nozzle flow. The target exit radius was 4 inches to allow for small scale experiments of objects about the size of a soda can. This radius would be large enough to prevent the boundary-layer from interfering with flow over a test article.

The following describes the steps taken for the selected nozzle once iterations of CONTUR were completed:

1. Input the nozzle coordinates and derivatives into MATLAB. The number of points that CONTUR outputs is limited and there is no guarantee that the derivatives at the points would be the maintained.
2. Use a second-order Taylor series expansion to ensure the contour's derivatives are maintained at each point. Hand-check the contour and remove any discontinuities.
3. Remove a portion of the contour near the throat. This will cause the simulation to start fully supersonic and improve numerical stability.
4. Output the nozzle coordinates and create a mesh.
5. Export the mesh and run a CFD simulation.
6. Compare the solution with the design Mach number (if available). If a shock occurs in the nozzle or the Mach lines are too visible, then most likely the Mach gradient from CONTUR was too high.

The inputs in CONTUR limit the number of points that are exported. More points are added within MATLAB to ensure a smooth contour when the points are imported into Pointwise®. If the exported points are immediately plotted within MATLAB, then the nozzle contour may not have a wall angle of 0° at the throat – or the correct wall angle at any other point since MATLAB interpolates the points to create a spline. It is unknown how Pointwise® would determine the shape of the wall from the coordinates exported directly from CONTUR; therefore, the best course of action is to enforce a condition that would maintain the derivatives at each point via a Taylor series expansion. A Taylor series is used to estimate the coordinate immediately in front of and behind the targeted coordinate which ensures the slope of the wall is maintained at all points on the nozzle wall.

Table 3.2: Primary input parameters for CONTUR. Variables are listed as used in CONTUR.

	<i>Mach 6.13</i>	<i>Mach 4</i>
CMC	6.13	4
ETAD	13.7°	10.6°
RC	15.3	11.1
BMACH	(0.98)CMC	(0.99)CMC

The result of CONTUR of a Mach 6.13 nozzle is shown in Figure 3.4 and shows the inviscid and viscous flow geometries along with two characteristic lines from the inviscid design. These characteristic lines separate show the general zones of flow in the nozzle:

1. Radial flow
2. Transition
3. Parallel flow

The right running characteristic intersects the nozzle at the inflection point and separates the radial flow from the transition region. It is favorable to start with fully supersonic flow to encourage stability in CFD simulations. Thus, a design point was selected slightly downstream of the nozzle throat where the Mach number is just above one. The design and inflection points are marked in Figure 3.4.

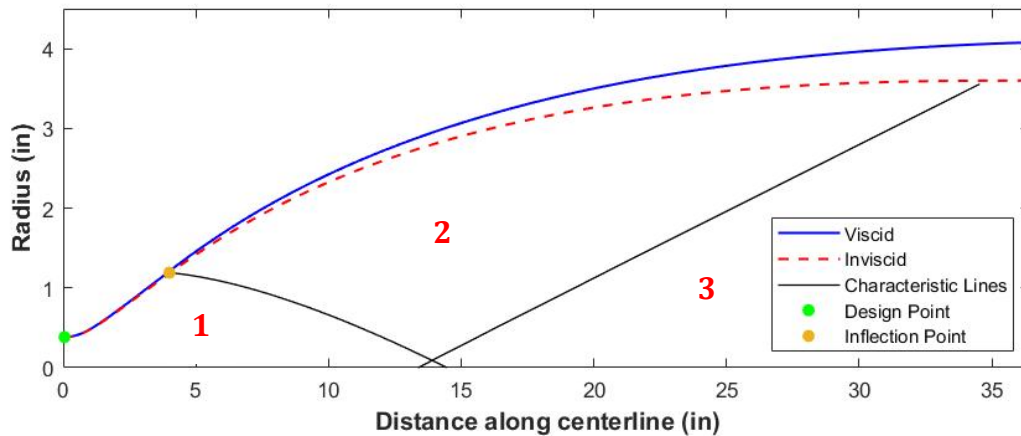


Figure 3.4: Inviscid and viscous flow nozzle geometry for the Mach 6.13 nozzle from CONTUR with characteristic lines separating the main flow regions in the nozzle.

A small Mach 4 nozzle was designed for a quick experiment with cold N_2 gas to confirm the design approach using CONTUR and validate the CFD simulations. The results of the Mach 4 geometry is shown in Figure 3.5. The boundary-layer did not affect the viscous flow design as significantly as the Mach 6.13 nozzle because of the cold flow conditions. The high temperature and high Mach number in the Mach 6.13 nozzle caused the boundary-layer to transition from laminar to turbulent. The full geometry could not be tested due to time and facility limitations; therefore, the nozzle was cut back to an area ratio of 7.72 for the experiment in order to match atmospheric pressure at the nozzle exit. The resulting nozzle had an exit radius of 1.02 inches and exit Mach number of 3.64 according to isentropic relations.

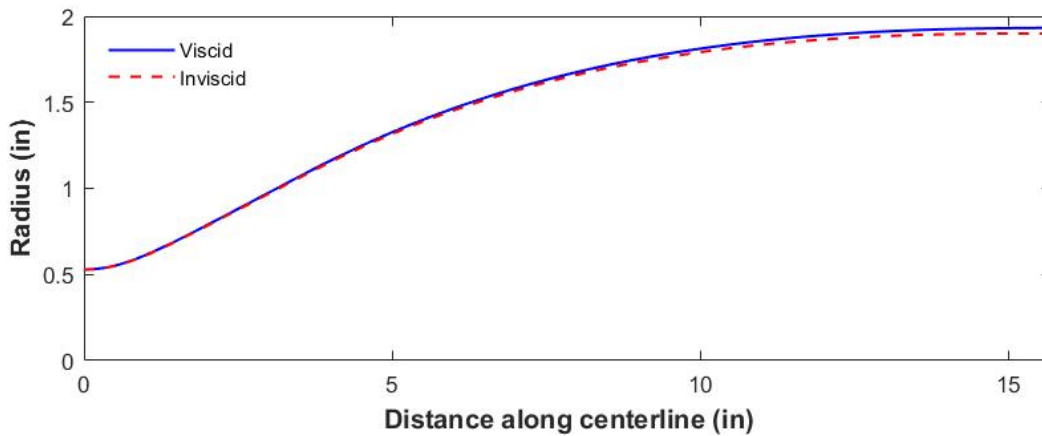


Figure 3.5: Inviscid and viscous flow geometries of a Mach 4 nozzle generated by CONTUR.

3.2 CFD Approach

Each set of simulations started with a basic simulation of the contour to understand flow within the nozzle and at the nozzle exit plane. Additional features were added after a successful run to simulate flow in a test chamber and over a test article. Each simulation used a structured mesh. The contour geometry was imported after the data were formatted in MATLAB. A hyperbolic tangent spacing distribution was applied to all connectors. The hyperbolic tangent spacing function in Pointwise® clusters grid points to connector break point and captures the high curvature of the nozzle better than other options available. Modifications or additions were made to the basic mesh consisting of only the nozzle contour for subsequent meshes. A box to represent the test chamber was added adjacent to the nozzle exit plane and a triangle along the centerline to

represent a conic test article. The spacing along the walls were held constant throughout the mesh in the event the wall ended – spacings along these regions were determined by the position of the nearest wall. Figure 3.6 and Figure 3.7 show a mesh of the Mach 6.13 nozzle with the addition of a test chamber and test article. The test article was set 0.5 inches from the nozzle exit. The nozzle was created with 600,000 grid points with a sponge layer that added 6,000 points at the nozzle exit. The boundary wall of the sponge layer was set as an inviscid wall to avoid additional growth of the boundary-layer that could affect the solution. The sponge layer at the nozzle exit was removed with the addition of the test article and test section. An additional 900,000 grid points were added to the nozzle with the addition of the test chamber and the mesh was further modified when the test article was created. The addition of the test chamber brings the number of grid points to 1.5 million, and the addition of the test article brings the number of grid points to 1.6 million. The connectors in the freestream seen in Figure 3.7 are the lines along which the spacing is constant in the y-direction in order to maintain orthogonality and mitigate the risk of diverging grid lines. The grid spacing at the edge of the farfield increased to 1 centimeter to create a sponge layer for the Mach 6.13 simulations. The Mach 3.64 nozzle had 350,000 grid points with 465,000 points added with the test chamber and test article. The maximum spacing in the sponge layer in the Mach 3.64 nozzle simulation was set to 5 centimeters. The boundary conditions in the Mach 6.13 and Mach 3.64 nozzle simulations using the meshes displayed in Figure 3.6, Figure 3.7, and Figure 3.8 are as follows:

- Supersonic inlet at the throat
- Adiabatic wall (constant heat flux = 0) on the nozzle and test article walls
- Farfield for the test chamber boundary lines
- Symmetry along $y = 0$

An adiabatic wall is considered an appropriate assumption since the nozzle is intended to run for a relatively long duration of time. The farfield boundary condition allows for the pressure in the test chamber to be enforced on the nozzle while allowing flow to exit any farfield boundary via extrapolation and hence removing the risk of over-defining the simulation.

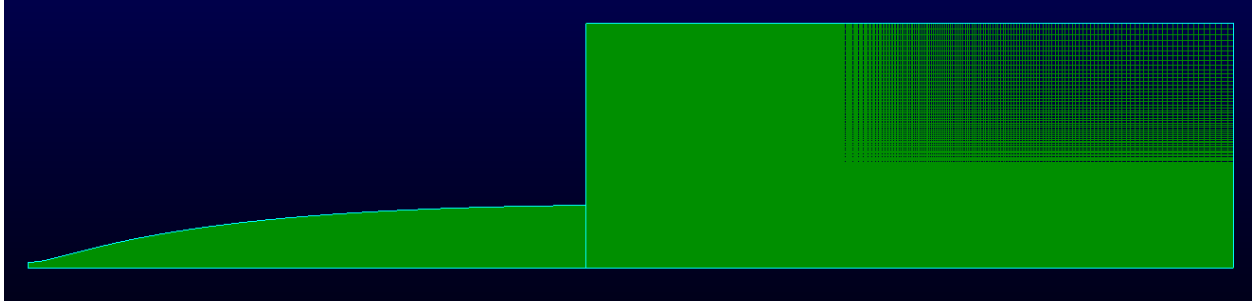


Figure 3.6: Mesh of Mach 6.13 nozzle with test section.

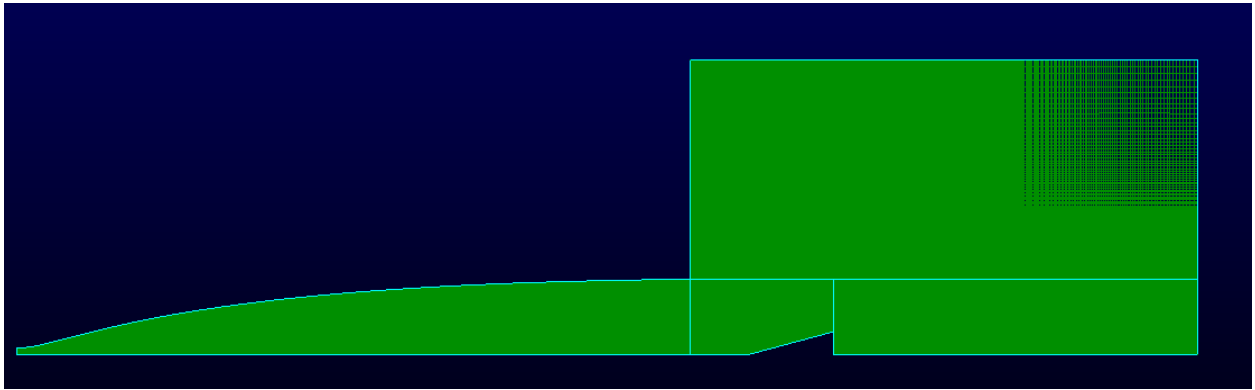


Figure 3.7: Mesh of Mach 6.13 nozzle with test section and test article.

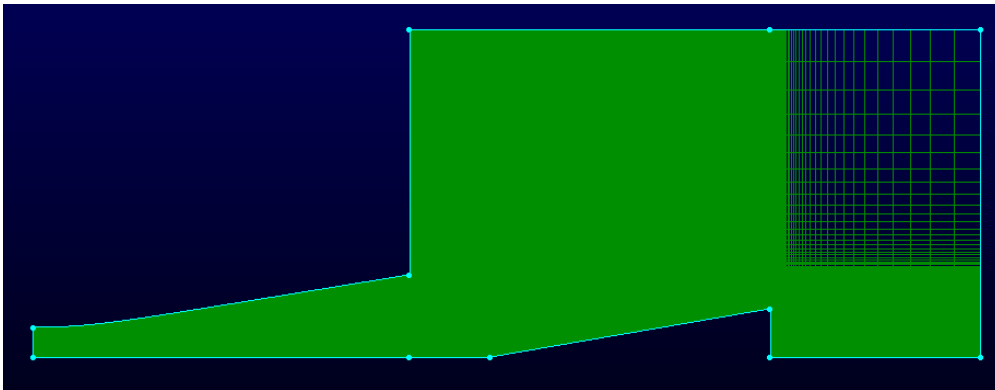


Figure 3.8: Mesh of Mach 3.64 nozzle with test section and test article.

The Mach 6.13 nozzle was simulated RANS calculation using SU2 version 7.0.4. A summary of select options are listed in Table 3.3 for the simulation on the nozzle with a test section and test article added. A CFL number of 15 provided the best balance of optimal convergence speed and stability. The convective scheme was solved with a first order scheme (i.e., MUSCL

option turned off); an attempt was made to perform a simulation with a second-order scheme, but the solution proved to be unstable and diverged. Other parameters such as thermal diffusivity and Prandtl number were input according to the state of the $N_2 - O_2$ mixture.

Table 3.3: Select input parameters in SU2 for a simulated Mach 6.13 nozzle with a test article and test section.

Solver	RANS
Turbulence model	SST
Freestream pressure	1277 Pa
Freestream temperature	226 K
γ	1.3448
Gas constant	$283.22845 \frac{J}{kg \cdot K}$
Inlet velocity	834.85 m/s
Inlet temperature	1639.4 K
Inlet pressure	1853.9 kPa
Slope limiter	Van Albada Edge
Convective scheme	AUSM

The Mach 3.64 nozzle was simulated using Kestrel version 10.4.1rc3. Kestrel proved to be more stable than SU2 which allowed for other options to be used to increase convergence speed; however, most options were input as the same as in SU2 for consistency. A summary of key inputs for simulating the nozzle with a test section and test article are listed in Table 3.4. The native perfect gas option was selected using N_2 . A constant CFL number of 10 was used for stability.

The Mach 3.64 nozzle simulation results were compared to experimental results provided courtesy of Utkarsh Pandey. The experiment implemented a background-oriented schlieren (BOS) system to characterize the density change in the flowfield. A dot pattern is placed in the background to aid the BOS imaging process. During a run, fluid flow accompanied with large density gradients such as shock waves and expansion fans distort the light over the dot pattern which is captured by changes in the pixel shifts of the background image. A resulting density gradient image compares a reference image with an image from the flow. Sample images used for

BOS are shown in Figure 3.9 and Figure 3.10. The reference image used in the BOS is shown in Figure 3.9. An image taken during one of the runs with the dot pattern distorted is shown in Figure 3.10.



Figure 3.9: Reference image used in BOS.



Figure 3.10: Image of taken during run of Mach 3.64 nozzle.

The axisymmetric nozzle was machined from aluminum with the same dimensions used in the CFD simulation. The nozzle was mounted on a rocket test stand with the flow direction moving down vertically onto a mounted cone measuring 2.44 inches in length and a half angle of 7° as seen in Figure 3.11. The flowfield was captured using a Phantom v1212 high-speed camera setup approximately five feet from the nozzle exit. The N_2 gas was supplied at room temperature and a maximum stagnation pressure of 600 psia. The N_2 gas was contained in a pressure chamber and released through a valve at 400 *psia* and allowed to run for 5 seconds. A pressure transducer was set 0.5 inches upstream of the nozzle exit plane.

Table 3.4: Key inputs simulating the Mach 3.64 nozzle with a test section and test article in Kestrel.

Model	RANS
Turbulence model	SST
Transition model	Menter 1-equation
P0	3447.4 kPa
T0	298 K
Inlet Mach number	1
Freestream pressure	3497.9 Pa
Freestream temperature	219.51 K
Spatial accuracy	2 nd -order
Transition temporal accuracy	1 st -order
Turbulence spatial accuracy	1 st -order
Slope limiter	Venkatakrishnan
Inviscid flux scheme	HLLE+
Viscous flux scheme	LDD+
Convective flux scheme	HLL

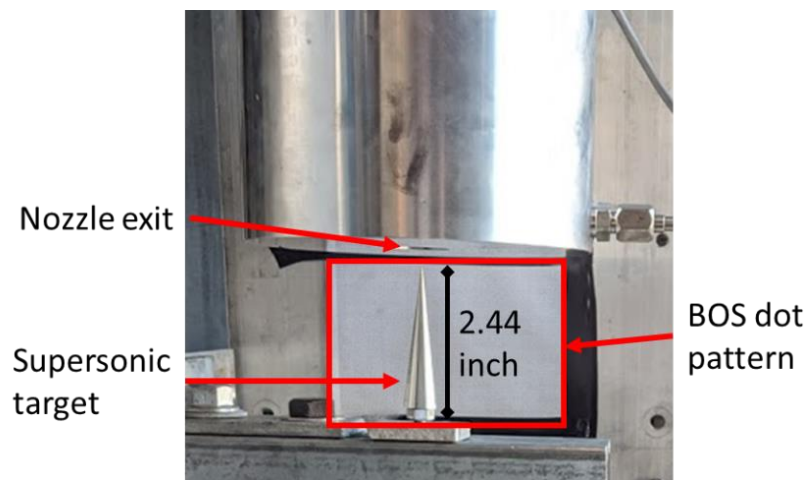


Figure 3.11: Experimental setup of nozzle and test section.

3.3 Results

This section discusses the nozzle simulation results from SU2 and Kestrel and the thermochemistry modeling code Chemkin. The nozzle simulations supported Sivells' approach [8] to create a viscous flow contour. The approach is validated with a comparison of experimental results. The simulations implement a basic RANS calculation of a perfect gas mixture of N_2 and O_2 . Additional modeling must wait until the detailed thermochemistry can be incorporated. The primary gas to be used in the test facility is nitrous oxide gas. The thermal decomposition of N_2O is modeled in Chemkin to gain insight to the thermochemistry of the test facility.

3.3.1 Nozzle Simulations

The Mach 6.13 simulations provide a check of the hypersonic nozzle design obtained with CONTUR. The resulting data were analyzed in MATLAB to view specific flow phenomena and flowfield visualization. The distances are nondimensionalized by the nozzle length, $L = 36.45$ inches, and local radius, h . Figure 3.12 shows a Mach contour of a converged solution of the Mach 6.13 nozzle calculated with SU2. The Mach number contour ranges from 0 to 6.5 to capture the boundary-layer and maximum values in the flowfield. The boundary-layer is clearly apparent as the contour transitions from the freestream value to zero. The boundary-layer growth is also easily seen in the Mach contour, which gives a relative picture of the displacement thickness added to the inviscid contour. The displacement thickness is strongly influenced by the thermal boundary-layer thickness since $Pr_t < 1$. Close inspection of the Mach number contour and temperature contour in Figure 3.12 and Figure 3.14 reveals that the momentum thickness and thermal boundary-layer thickness are approximately the same. The skin friction on the nozzle wall is expected to increase with the increase in freestream velocity. Despite the decrease in temperature and pressure on the nozzle wall from the throat to the nozzle exit seen in Figure 3.16 (a) and (b), the skin friction is high enough due to the accelerating flow to remain attached to the adiabatic wall. The Mach 6.13 nozzle is designed to perform under turbulent conditions, which is confirmed by the Reynolds number Figure 3.13. The Reynolds number is the largest at the throat where $\rho \times u$ is the highest as a result of the high temperature. The temperature and value of $\rho \times u$ decrease as the flow accelerates, as seen in Figure 3.12 and pressure decreases, as seen in the pressure contour in Figure 3.15.

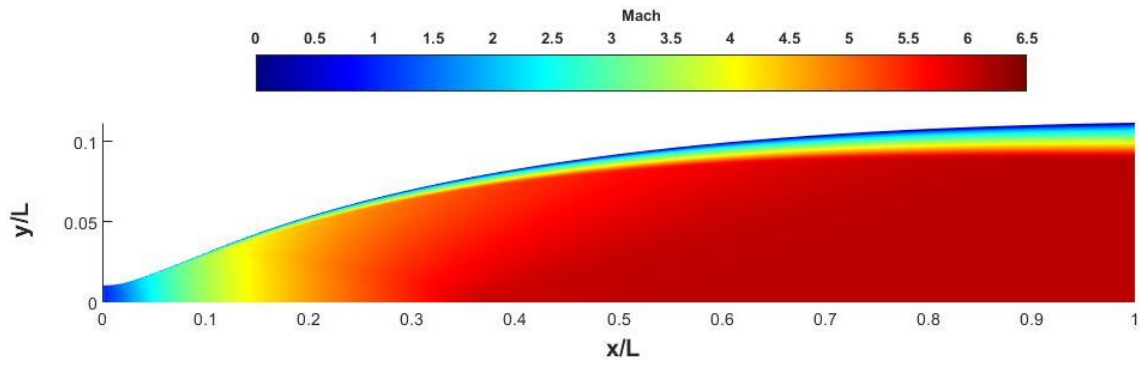


Figure 3.12: Mach contour of Mach 6.13 nozzle

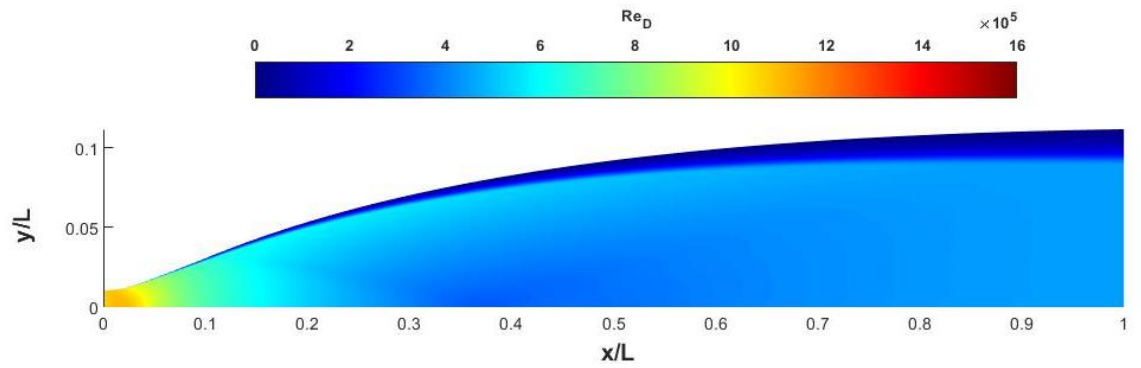


Figure 3.13: Reynolds number contour in Mach 6.13 nozzle.

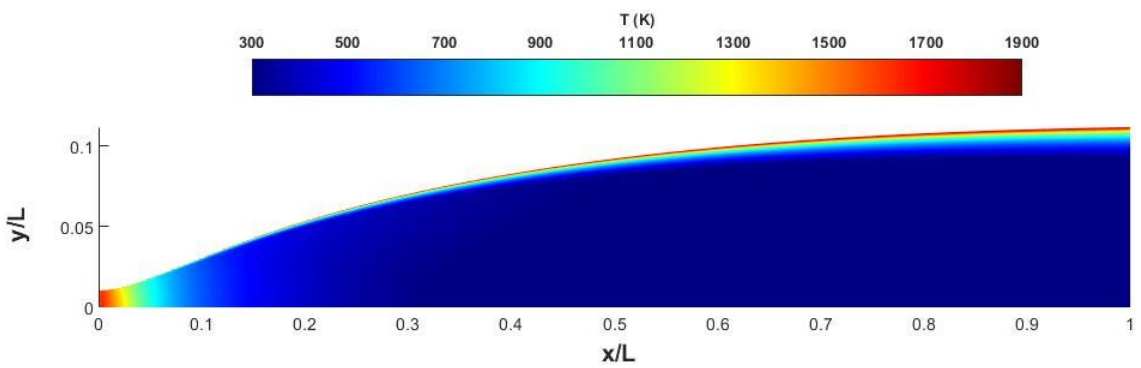


Figure 3.14: Temperature contour for Mach 6.13 nozzle.

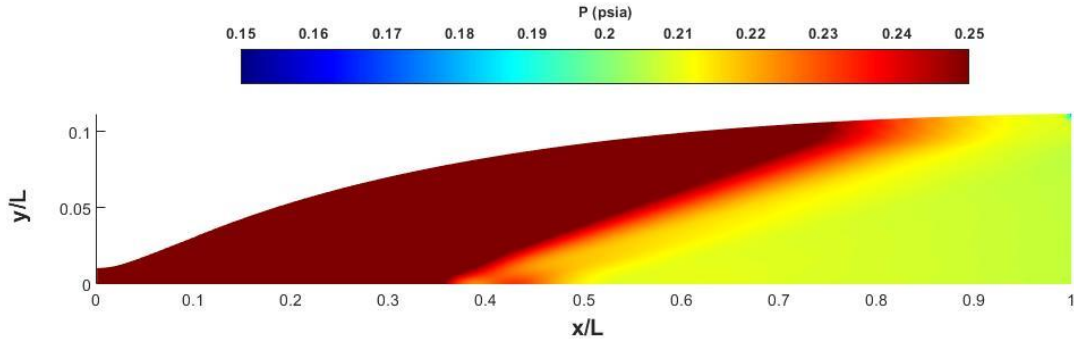
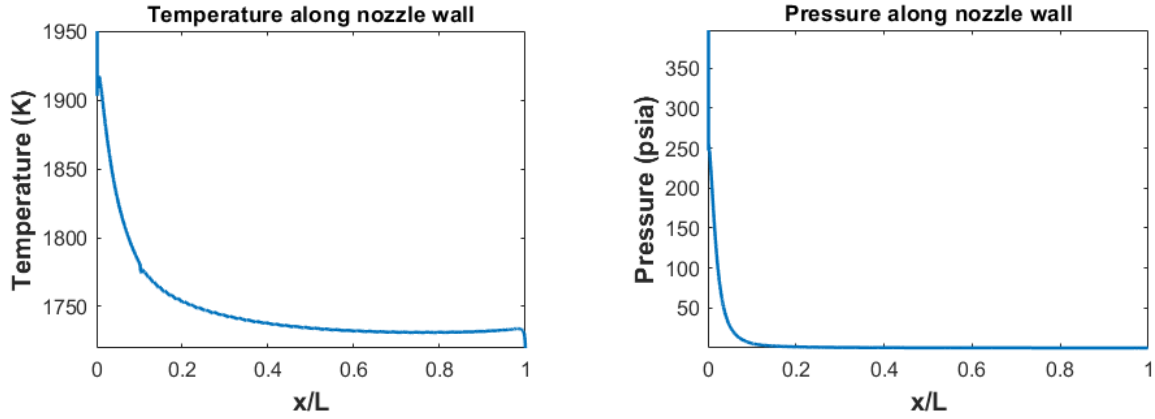


Figure 3.15: Pressure contour of Mach 6.13 nozzle.

The Mach number along the centerline was plotted to confirm that the maximum Mach number reached was at the exit of the nozzle as seen in Figure 3.17. Several previous iterations exhibited a maximum Mach number before the nozzle exit due to the increasing thermal boundary-layer height caused by an excessive nozzle length. The primary objective of this nozzle is to achieve uniform flow before reaching the test article and test section. Uniform flow can be measured by examining flow parameters such as the Mach number, velocity, or pressure at the nozzle exit. The flow is expected to exhibit some fluctuations from freestream values near $y/h = 1$ because of the boundary-layer. Figure 3.20 (a) shows the Mach distribution at the nozzle exit plane ($x/L = 1$). The Mach number increases from the wall to the edge of the boundary-layer and reaches a uniform flow at Mach 6.115 in the main flowfield at the nozzle exit plane which is a 0.24% deviation from the design criterion. The Mach number appears to be uniform outside of the boundary-layer; however, a closer inspection seen in Figure 3.20 (b) shows that the Mach number increases again at $y/h = 0$ to 6.12. This sudden increase is also exhibited in other parameters such as density and momentum shown in Figure 3.20 (c)-(f). These issues are created by the boundary conditions enforced in SU2. SU2 is an FVM solver; henceforth, the calculations are performed at the cell center and extrapolation is required to acquire values at the nodes. The symmetry line is a special case that exhibits this behavior.



(a) Temperature profile on adiabatic nozzle wall

(b) Pressure profile on adiabatic nozzle wall

Figure 3.16: Pressure and temperature on the nozzle wall for the Mach 6.13 contour.

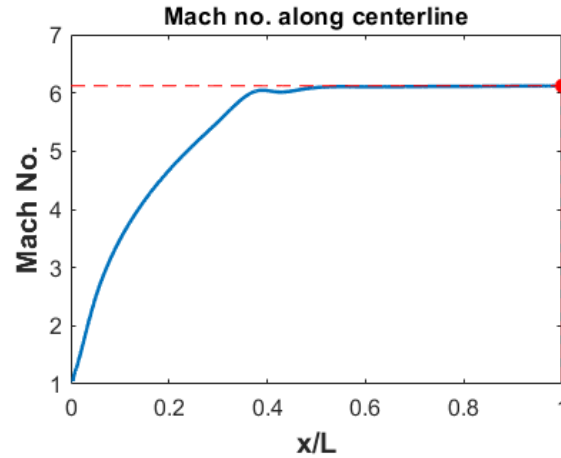


Figure 3.17: Mach number along nozzle centerline. The maximum Mach number is reached at the exit of the nozzle.

The pressure at the nozzle exit plane in Figure 3.18 exhibits the pressure distribution at the nozzle exit plane where $x/L = 1$, the wall angle is 0.54° , and the ratio to the radius of curvature is undefined (the radius of curvature at the point before the end of nozzle is 294.1 inches) as calculated by (3.3). The pressure increases from the wall and reaches a relatively steady freestream value around $y/L = 0.6$. The pressure variation in the boundary layer is assumed to be caused by the sponge layer added to the nozzle in the mesh (where $x/L > 1$) and the applied boundary condition was an inviscid wall since the curvature at $x/L = 1$ is 0. (It is possible in some high-speed nozzle flow cases for pressure variation in the boundary layer to be attributed to a combination of the longitudinal curvature of the mean streamlines and the increased impact of the

Reynolds stress terms to the normal stress perpendicular to the wall at increasing Mach number [67].) The assumption made is supported the pressure contour in Figure 3.19 where a sudden decrease in pressure occurs near the nozzle wall where the boundary conditions change.

$$R_c = \frac{\left(1 + \frac{dy^2}{dx}\right)^{1.5}}{\left|\frac{d^2y}{dx^2}\right|} \quad (3.3)$$

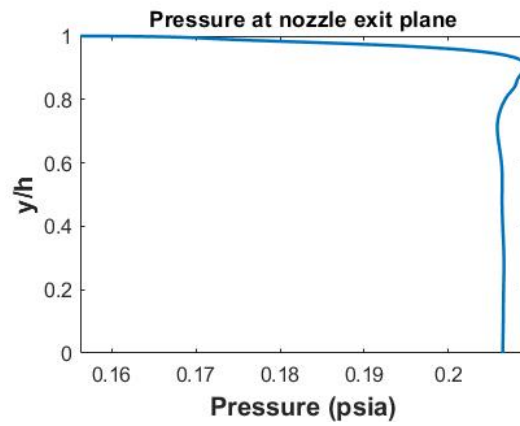


Figure 3.18: Pressure distribution at nozzle exit plane ($x/L = 1$) in the Mach 6.13 contour.

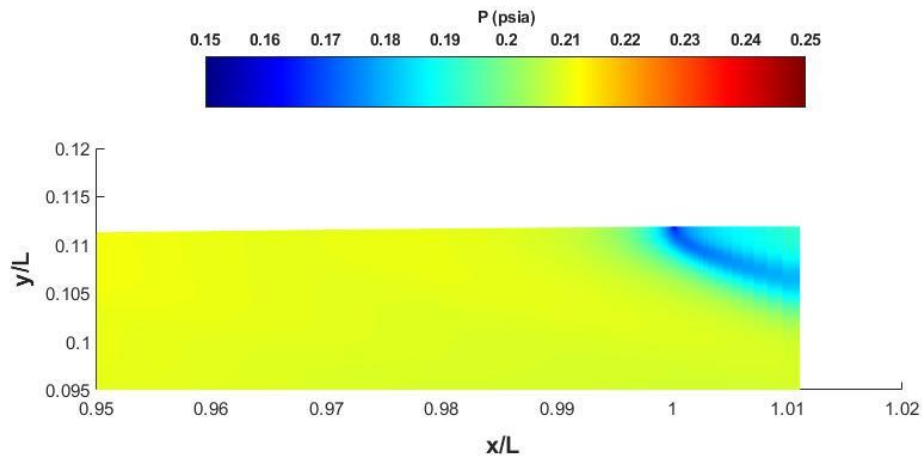
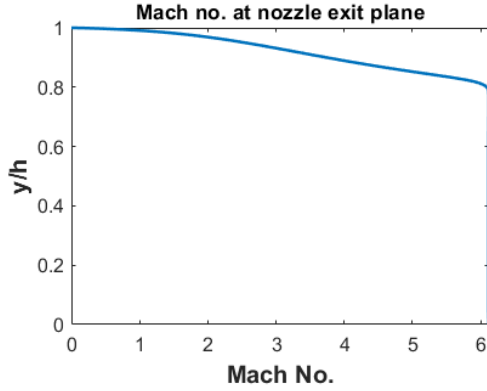
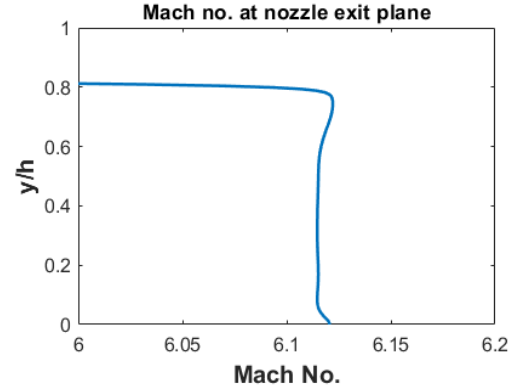


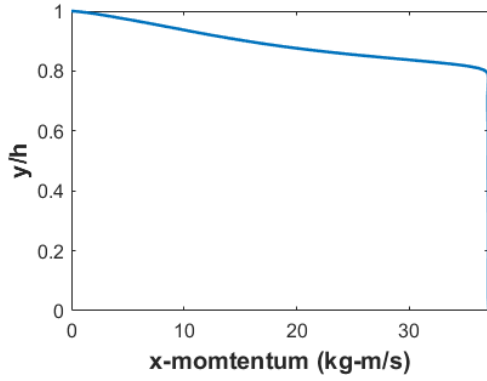
Figure 3.19: Pressure contour of Mach 6.13 nozzle from $x/L = 0.95$ to $x/L = 1.02$.



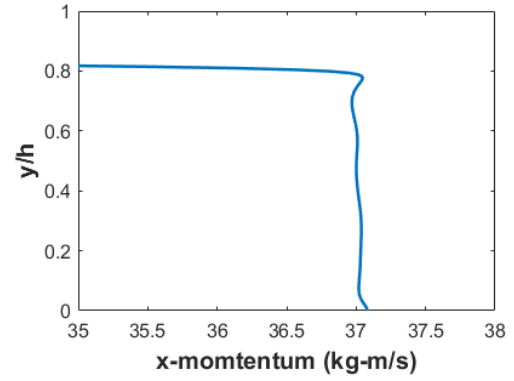
(a) Mach number distribution at the nozzle exit plane ($x/L = 1$).



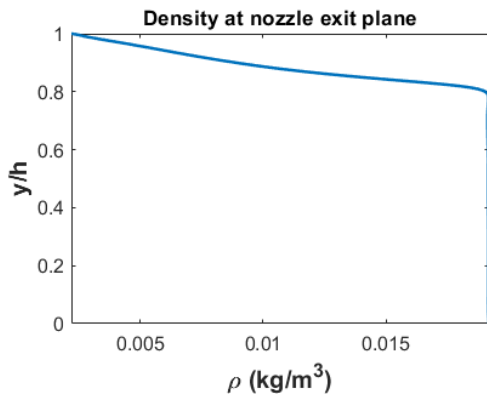
(b) Zoomed view of Mach number distribution at the nozzle exit plane ($x/L = 1$).



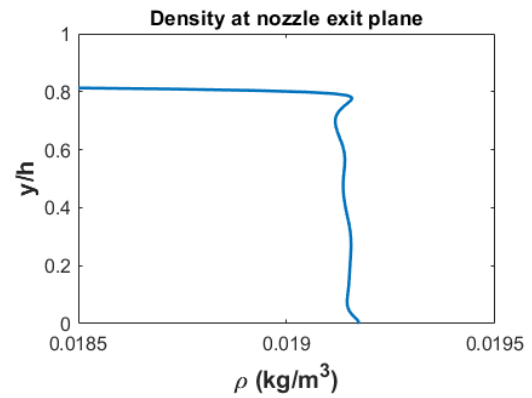
(c) x-momentum distribution at nozzle exit plane ($x/L = 1$).



(d) Zoomed view of x-momentum distribution at nozzle exit plane ($x/L = 1$).



(e) density distribution at nozzle exit plane ($x/L = 1$).



(f) Zoomed view of density distribution at nozzle exit plane ($x/L = 1$).

Figure 3.20: Mach number, momentum, and density distribution at nozzle exit plane for the Mach 6.13 contour. The local radius is $h = 4.078$ in.

Simulations proceeded with the addition of a test chamber and test article to simulate the flowfield in potential experiments. The density gradient magnitude and temperature contours in Figure 3.21, Figure 3.22, and Figure 3.23 show the resulting flowfield calculated by SU2. The density gradient magnitude shows some points of interest. From Figure 3.21:

1. The edge of the plume from the nozzle exit, corresponding to slightly under-expanded flow.
2. The diffusion of the mixing layer also exhibits behavior of an under-expanded flow.
3. The shock wave and expansion fan from the test article interact with the plume.

Figure 3.22 shows a closer look at the flow phenomena occurring on the test article. The shock wave and expansion fan diffuse into the flowfield around $x = 44$ inches. The temperature contour in Figure 3.23 shows a clear edge to the nozzle plume and boundary-layer edge. The temperature increases behind the test article in the wake region which extends through the outlet of the test section.

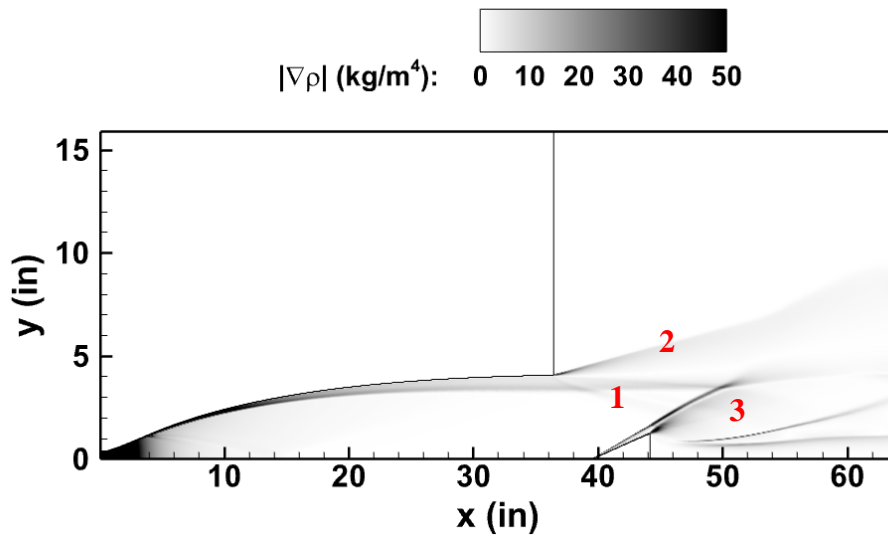


Figure 3.21: Density gradient magnitude of Mach 6.13 nozzle with test chamber and test article.

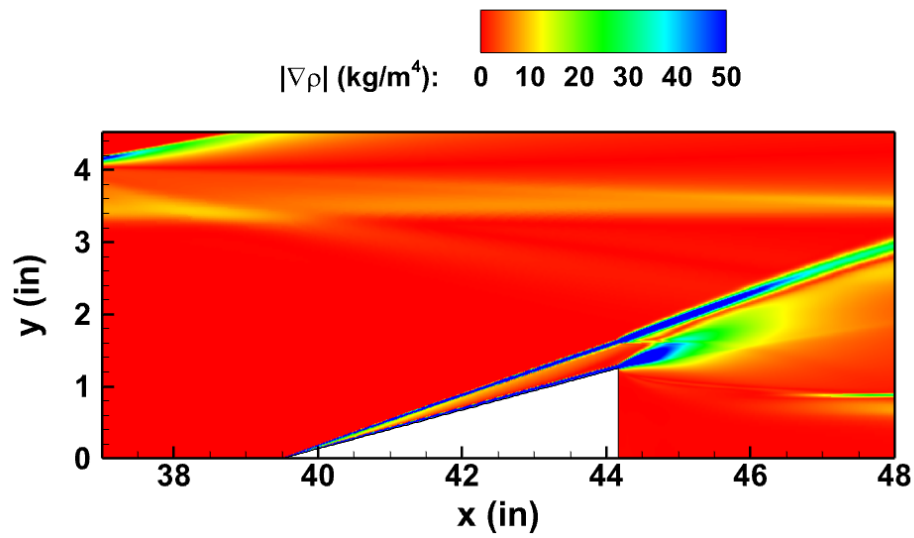


Figure 3.22: Density gradient magnitude of Mach 6.13 nozzle zoomed to view test article.

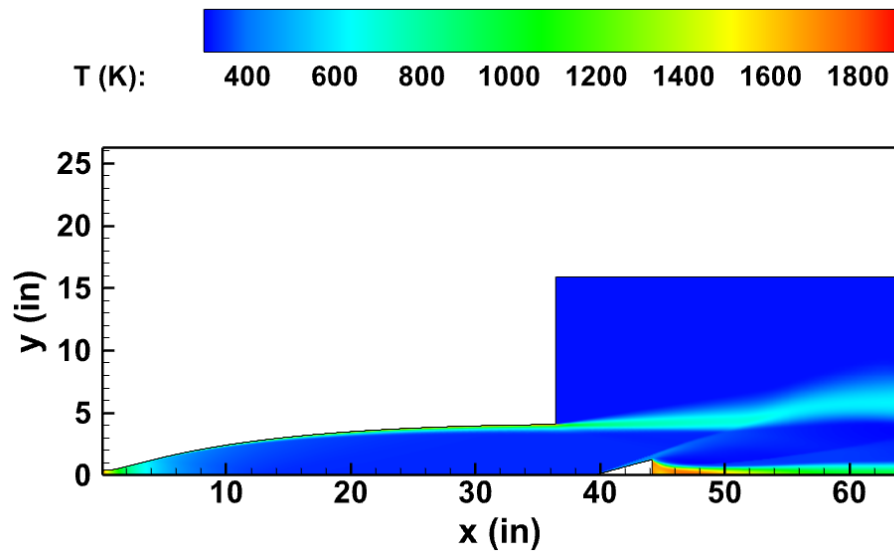


Figure 3.23: Temperature contour of Mach 6.13 nozzle with test chamber and test article.

The simulation results of the Mach 3.64 nozzle are discussed below. General flow features are visualized in the Mach contour in Figure 3.24 and the density gradient magnitude contour in Figure 3.25. The Mach contour shows an oblique shock and expansion fan on the test article and

an under-expanded flow plume exiting the nozzle. A wake region also exists behind the test article. Other flow features are readily visualized in the density gradient magnitude contour. The density gradient magnitude contour shows a clear edge to the plume and the dissipation of the boundary-layer exiting the nozzle.

The experiment with the Mach 3.64 nozzle produced a BOS image of the density gradient at 3 seconds and a static pressure outlet measurement. Figure 3.25 was compared to the Figure 3.27 to match significant flow features. The density gradient shown in Figure 3.27 is the normalized displacement of each pixel between the reference image and flow image and can be considered relative and scaled. The results look similar at first glance; however, the flow structures in the BOS image are not symmetric and therefore cannot be compared with the CFD computations. The reason for this phenomenon is most likely caused by a test article at a slight angle of attack, the nozzle at a slight angle causing the flow to enter at a small angle, or some disturbance upstream of the nozzle exit.

Figure 3.28 shows the exit static pressure as it was measured in the experiment with a vertical line indicating the inflow of N_2 gas. The pressure starts at the ambient pressure before the test begins, experiences an immediate pressure drop once flow enters the nozzle and steadily decreases until the gas flow is halted. The static pressure in the experiment was measured 0.5 inches from the nozzle exit for the duration of the experiment. The static pressure at the same location in the CFD results in Figure 3.26 must be determined for an accurate comparison. The static pressure measured 0.5 inches upstream of the nozzle exit in the CFD simulation is 9.4 *psia*. This value agrees with the pressure measured approximately 3.5 seconds into the experimental run. If the maximum stagnation pressure in the experiment is considered ($P_0 = 600$ *psia*), then a direct comparison can be made with the CFD simulation using P/P_0 . The CFD simulations used a stagnation pressure of 500 *psia*, which results in $P/P_0 = 0.0188$. The maximum exit pressure recorded is around 12 *psia*, which results in $P/P_0 = 0.02$, which shows good agreement with the CFD simulations.

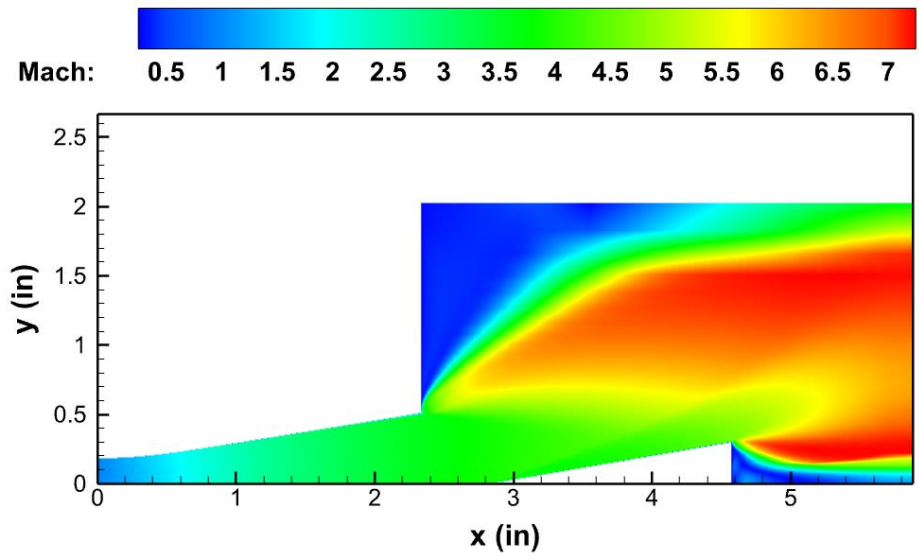


Figure 3.24: Mach contour of the Mach 3.64 nozzle with a test section and test article.

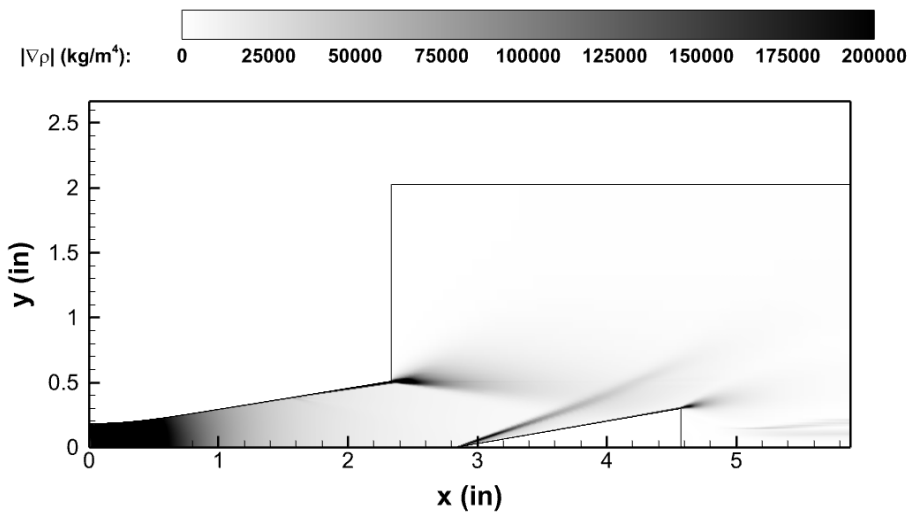


Figure 3.25: Density gradient magnitude of the Mach 3.64 nozzle with a test section and test article.

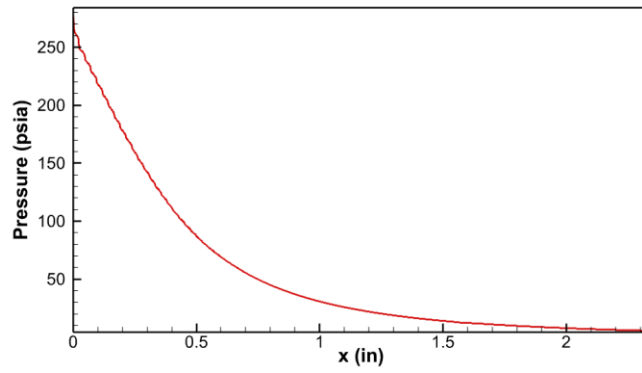


Figure 3.26: Static pressure along nozzle wall in CFD simulation of Mach 3.64 nozzle.

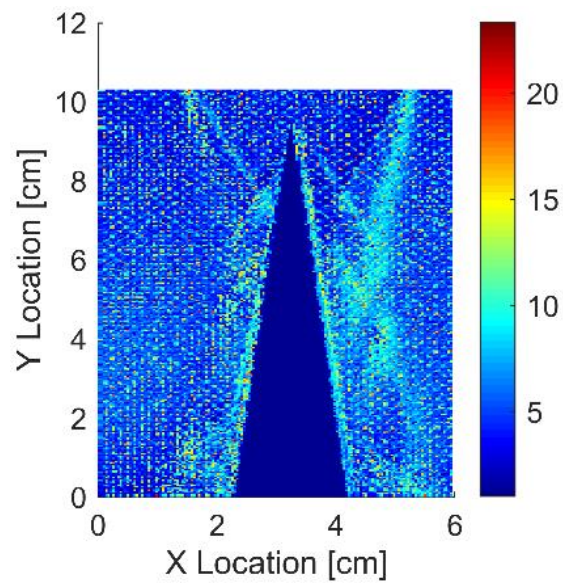


Figure 3.27: Density gradient over test article 3 seconds into the run of Mach 3.64 nozzle.

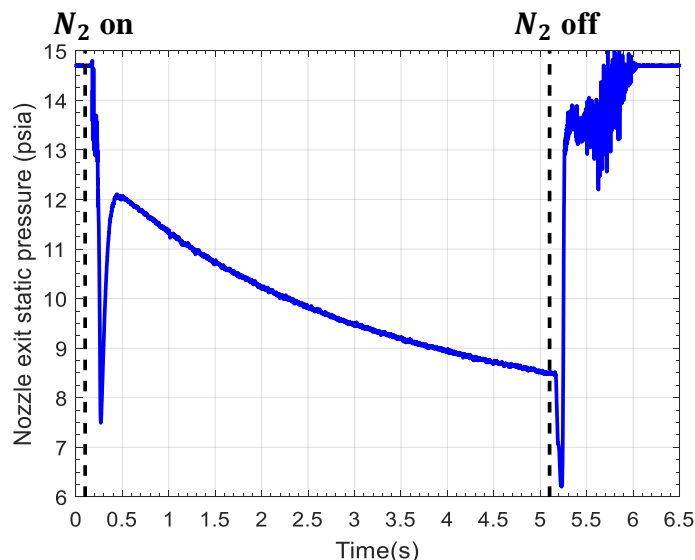


Figure 3.28: Nozzle exit static pressure in the experiment of the Mach 3.64 nozzle.

3.3.2 Thermodynamic Decomposition of N_2O

The reaction mechanism was simulated using a plug flow reactor (PFR) in Chemkin to quantify the production of NO_x and understand the thermochemistry of N_2O gas. The PFR is modeled with constant diameter and length of 0.02 and 0.1 meters respectively and a parametric study of inlet pressure, temperature, and velocity at 1500 – 2500 psia, 1000 – 1200 K, and 0.2 – 2 m/s respectively. Figure 3.29 plots the species composition and temperature in the PFR with nitrous oxide gas at an initial 1100 K, 1000 psia, and 0.2 m/s. The temperature steadily increases and jumps over 2000 K just before 0.2 meters, at which point the reaction rate substantially increases. The NO mass fraction peaks at this point and steadily decreases to a constant value as temperature increases to a constant value at approximately 2550 K. The reaction reaches equilibrium when the temperature reaches this value.

The overall species composition after the reaction can be seen in Figure 3.30 (a)-(d) at the velocity and pressure extrema tested. The reactions resemble a similar solution to the species composition within the PFR in Figure 3.29. There exists a local extremum of the NO produced at the temperature where the reaction starts. This extremum quickly decreases as the temperature increases enough to allow equilibrium to be reached. The reaction has the best quantities of N_2

and O_2 at the lowest temperature requirement for the reaction to occur – this value also produces the lowest amount of NO . Comparing Figure 3.30 (a) to Figure 3.30 (b) and Figure 3.30 (c) to Figure 3.30 (d), one can see the effect of the pressure on the reaction: the reaction rate increases after the spike in temperature and progresses to equilibrium faster at higher pressure. In Figure 3.30 (c), the NO mass fraction peaks and steadily decreases as temperature increases. Figure 3.30 (d) shows the same behavior; however, the equilibrium is acquired at a lower temperature than in Figure 3.30 (c). The velocity and species composition of the reaction are independent of each other; therefore, the velocity has no effect on the amount of NO produced once equilibrium is reached. Figure 3.31 shows the minimum temperature required for a complete reaction to occur. A complete reaction was defined when the mass fraction of N_2O dropped below 10^{-5} . The minimum temperature required for a complete reaction is approximately 1022 K and increases with velocity and decreases with increasing pressure. Pressure has little effect on the reaction temperature – the lowest and highest pressures tested are separated by a low of 0.5 K, a high of 1 K, and an average of 0.68 K.

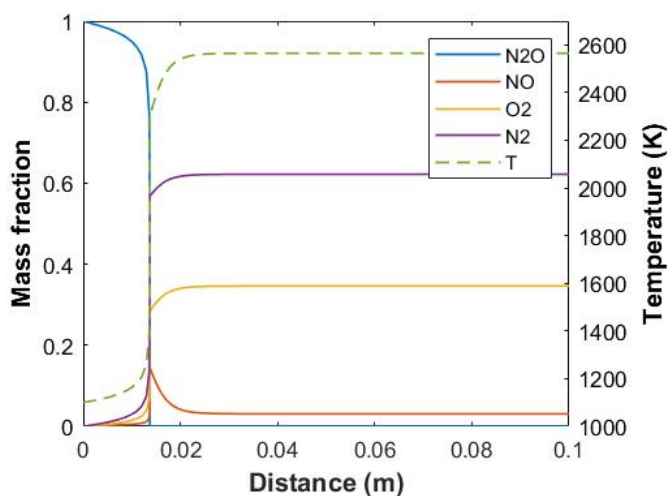


Figure 3.29: Species composition inside PFR with inflow values of 1100 K, 1000 psia, and 0.2 m/s.

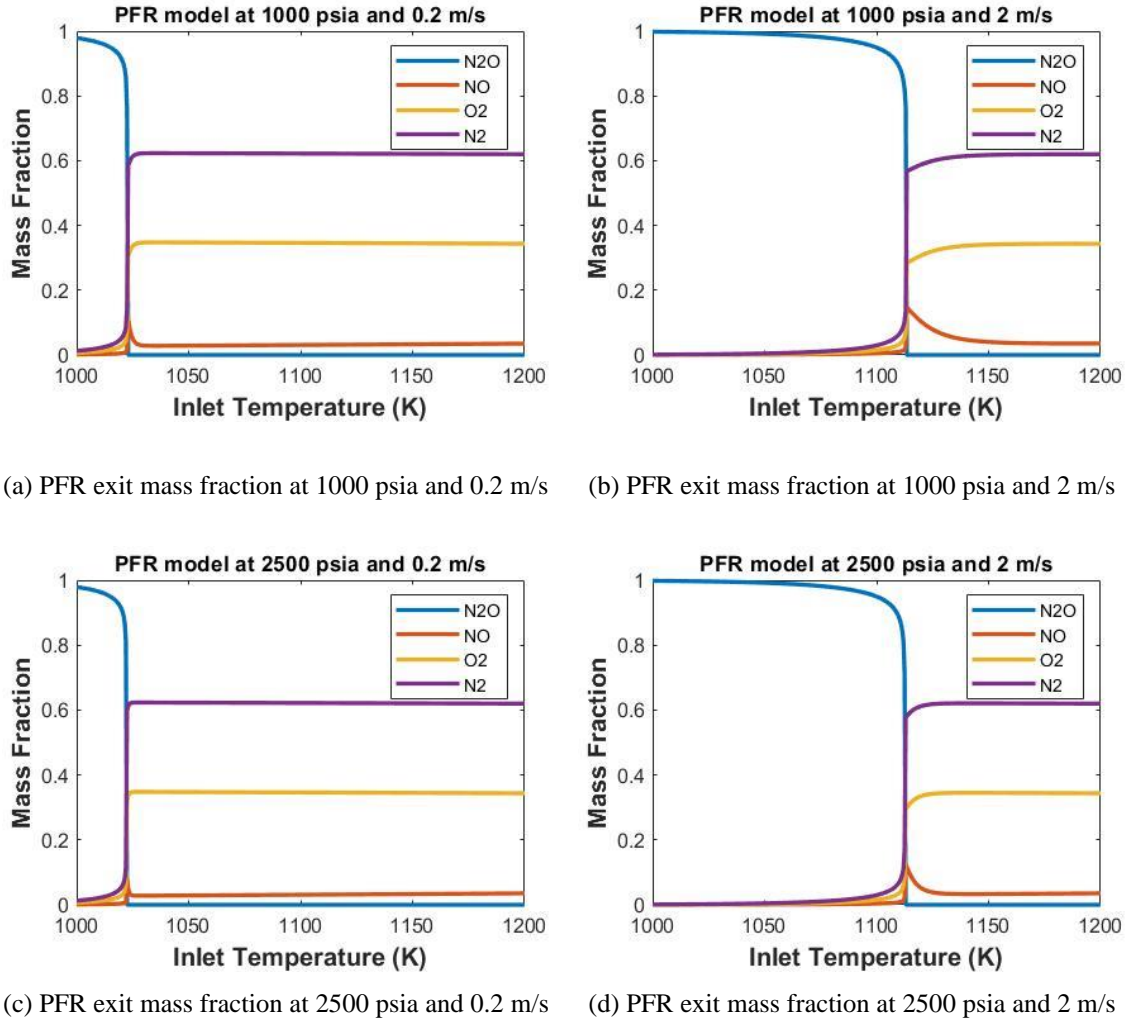


Figure 3.30: Species decomposition at the exit of the PFR at constant velocity and pressures.

A preheated temperature greater than 1000 K is required for nitrous oxide to decompose at a sufficient rate, and the pressure of the reactant has an insignificant effect on the temperature requirement. Nitrous oxide also produces undesired levels of nitric oxide. The level of heating required to initiate thermal decomposition and achieve the desired exothermic reaction is impractical and costly. It thus desired and appropriate to utilize a catalyst as a means to mitigate the NO production and lower the temperature required for N₂O to decompose. Thermal decomposition is expected to occur in a facility utilizing a catalyst since temperatures are expected to increase above 1000 K at the throat of the nozzle. Fortunately, the high temperatures produced

in a hypersonic test facility will promote the lowest amount of NO_x created in the thermal decomposition.

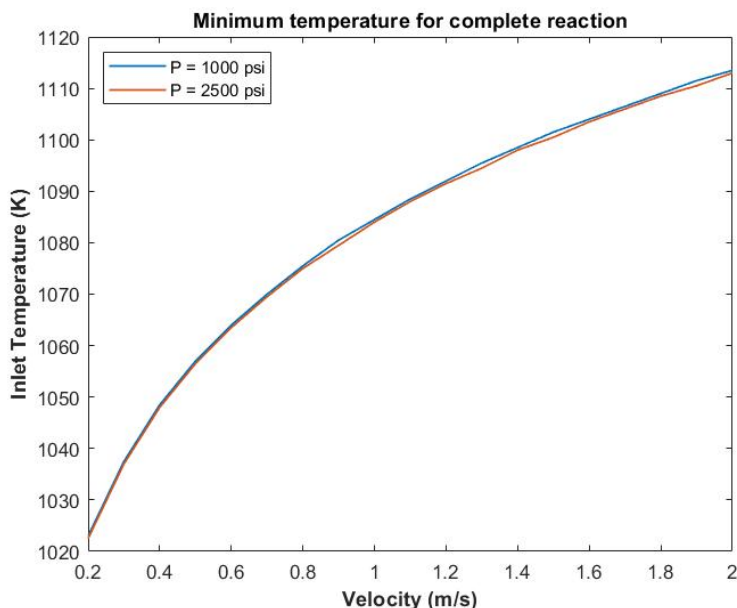


Figure 3.31: Temperature required for a complete reaction to occur at various pressures and velocities.

The addition of a catalyst will effectively lower the activation energy of the global reaction and permit the reactant to undergo decomposition at a lower temperature. An effective catalyst may also mitigate the level of nitric oxide produced; however, thermal decomposition may still occur.

3.4 Conclusions and Future Work

An investigation into the conceptual design of a high enthalpy hypersonic wind tunnel was performed. Sivells' computer program, CONTUR, was selected for initial nozzle contour design. Key performance factors were identified and a design process for creating a hypersonic nozzle was created. Nozzle contours were created at two design criteria with a given Mach number. The CFD simulations of the Mach 6.13 nozzle were performed in SU2 to provide results in the hypersonic realm and validate CONTUR's capability to produce high-quality nozzle contours for the

hypersonic regime. The Mach 6.13 nozzle showed adequate agreement with the design criteria and proved CONTUR's ability to account for a compressible turbulent boundary-layer. Simulations of the flowfield in a test chamber at an altitude of 95,000 feet was completed with the Mach 6.13 nozzle. The flow exiting the nozzle showed no interference with the flow over the test article and maintained enough uniformity over the test article to simulate a real experiment.

A simulation of a Mach 3.64 nozzle was completed to validate the design process and tools used via comparison with experimental results. The Mach 3.64 nozzle was originally designed as a Mach 4 nozzle that was altered due to time limitations in experiments; however, the results are still a useful step towards verification. It was not possible to compare the density gradient produced by the BOS image in the experiment to the density gradient magnitude contours produced by the CFD simulations because of limitations in the current experimental setup. The CFD simulations of the Mach 3.64 nozzle was thus checked by comparing static pressure on the nozzle wall 0.5 inches upstream of the nozzle exit.

The comparison and confirmation of experimental results with CFD results and the expected design criteria validates the design process created; however, the process has only included nozzles with a perfect gas flow at low hypersonic numbers. More investigation is required to confirm the robustness of CONTUR and the design process. The simulations of the Mach 6.13 nozzle showed good flow uniformity at the nozzle exit when considering the Mach number and pressure distribution which verifies CONTUR's ability to produce a nozzle used for a test facility. The Mach 3.64 nozzle showed good agreement with experimental results which validated the CFD results.

A mixture of nitrous oxide gas and nitrogen gas was selected to simulate air in the hypersonic test facility. Nitrous oxide decomposes into nitrogen and oxygen; the additional nitrogen in the mixture allows more control over the final species composition after N_2O decomposes to resemble the species composition in air. Furthermore, the reactants are free of hydrogen which mitigates the risk of water droplets condensing in the nozzle and test chamber. The thermal decomposition of N_2O was modeled in Chemkin to gain insight into the species composition resulting from the reaction and the requirements needed to initiate the reaction. The endothermic reaction of nitrous gas produced undesired levels of nitric oxide that would contaminate the flow. The temperature required to initiate the desired exothermic reaction is impractically high and the pressure has little effect on the temperature prerequisite. A carefully

designed catalyst can mitigate the amount of NO produced and remove the high temperature requirement to initiate the exothermic reaction of N_2O . The thermal decomposition of nitrous oxide may still occur in the nozzle in regions of high temperature – especially at the throat. Additional CFD modeling can implement the effect of a catalyst and thermochemical reactions into the solution of a nozzle once a catalyst is selected and the mechanism is understood. This thesis does not include research into the selection of a catalyst – that investigation is ongoing.

4. SHOCK / BOUNDARY-LAYER INTERACTION IN A HYPERSONIC MISSILE-FIN CONFIGURATION

Mean flow calculations were completed on hypersonic missile-fin configurations. The configurations were a conical and ogive missile as seen in Figure 1.6 and Figure 1.7 respectively. The missile fins will be referenced by Fin 1, 2, or 3 as labeled in the drawings. Additionally, the configuration simulated as given and with a 45° roll – this configuration will be referred to as “+1”. The +1 configuration rotated the location of the fins so that two complete fins were present instead of one full fin and two half fins on the symmetry boundary. These fins will be referred to as Fin 1a and 2a from top to bottom.

The missile-fin configurations were simulated using Kestrel’s CFD solver using a RANS formulation. The gas was simulated using a 5-species model to simulate possible nonequilibrium effects in air. The different configurations were simulated at three angles of attack: 0°, 1°, and 10°. Shock / boundary-layer interactions and complex 3D flow structures are visualized in the mean flow.

4.1 CFD Approach

The geometry of the missiles could not be meshed with a single surface mesh by quadrilateral elements due to the high sweep angle of the fins; thus, a hybrid structured-unstructured grid is used. The *Advancing Front Ortho* algorithm was used in Pointwise® to create a hybrid surface mesh. The size of the grid elements in an unstructured solver are determined by the edge length. The grid spacing distribution on the connectors will cause an uneven cell height growth from the boundary in order to match the spacing between each node. The *Trex* algorithm is used to force an even growth rate on essential boundary curves for a fixed number of cells or until Pointwise® is unable to create/resolve anisotropic cells.

It should be noted that structured mesh of overset grids is possible but not currently feasible for this research. The current CFD solver, Kestrel, is able to calculate solutions for dual mesh and overset grids; however, it cannot treat an overset mesh boundary on no-slip boundary surfaces. It is not recommended to use overset grids in Kestrel unless a single block is able to resolve the surface and boundary-layer mesh.

The quality of the surface mesh was measured by the area ratio of the grid. The area ratio for the surface meshes was maintained at or below 5. It is advisable to run further simulations with a maximum area ratio around 1.2, which is the recommended maximum value for structured grids. A higher quality grid is needed for a grid-independent solution to be confirmed.

The surface mesh of the conic missile is represented in Figure 4.1. The surface mesh of the conic missile configuration contains 366,000 quadrilateral elements and 5800 triangular elements resulting in 371800 total surface elements. The maximum area ratio measured on the surface mesh is 4.8. Images of the surface mesh are captured in Figure 4.2 in Figure 4.3. The surface mesh on the conic missile-fin configuration is representative of surface meshes generated on the other missile-fin configurations. As seen in the figures of the surface mesh, grid points and cell density were focused on the fin region of the missile and reduced on the nose to reduce the overall number of grid points and reduce computation expense. The *Trex* algorithm is used to capture the curvature of the fin's blunt leading edge. The connectors where *Trex* enforced a specified growth rate are located on the tips of all of the fins, the trailing edges of the fins, connectors on the symmetry line, and connectors at the back of the missile. The initial cell height for all connectors on the conic missile-fin configurations was 0.11 mm.

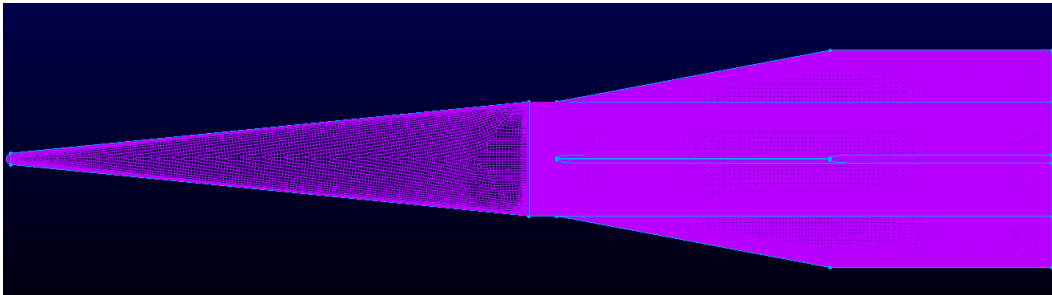


Figure 4.1: Surface mesh of conical missile.

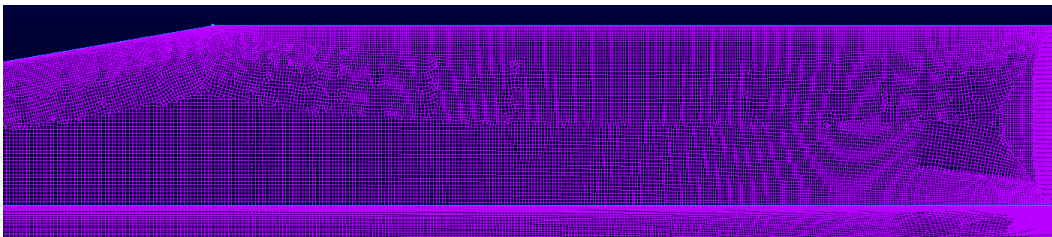


Figure 4.2: Surface mesh on missile fin created by *Trex*.

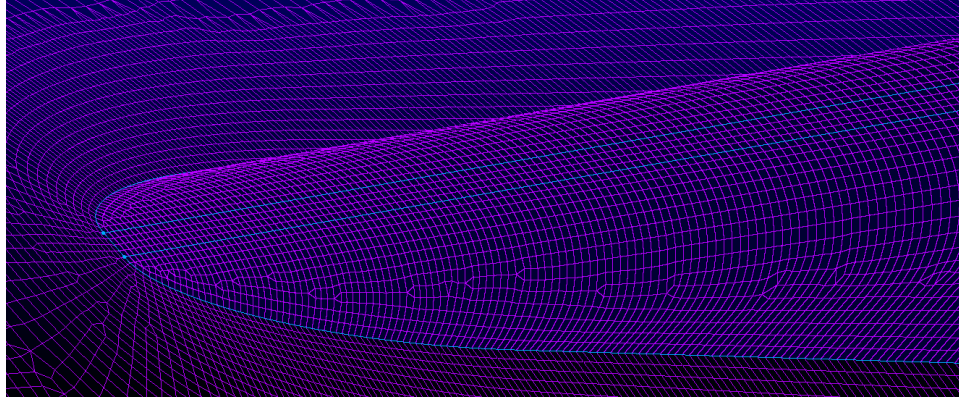
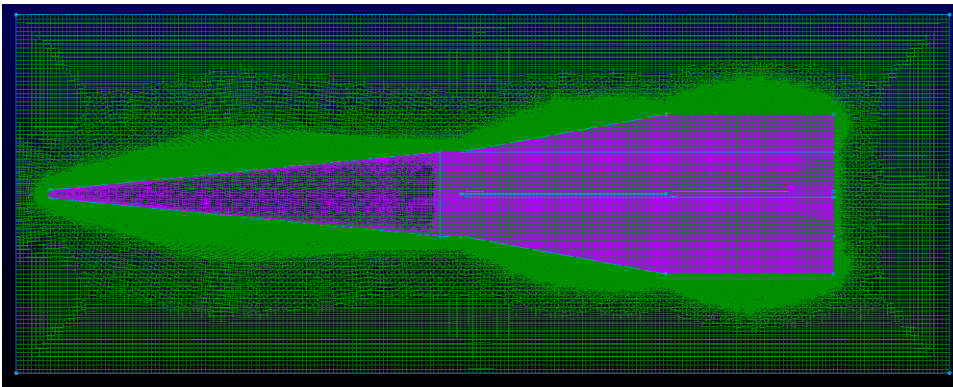
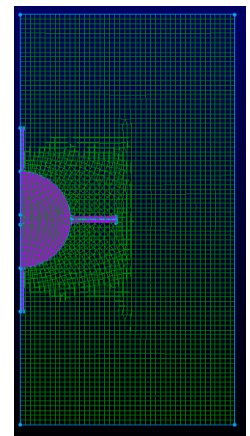


Figure 4.3: Surface mesh on blunt edge of missile fin and interface onto missile body created by *Trex*.

Once an adequate surface was created, the *Trex* scheme was used to generate a 3D block as seen in Figure 4.4. A prism layer was generated with anisotropic cells with a fixed growth rate of 1.03 and an initial height of $9\text{ }\mu\text{m}$. Isotropic cells were created outside of the prism layer until a smooth, fixed cell size was obtained, which is clearly seen in Figure 4.4. (a). The resulting prism layers can be viewed on the symmetry boundary in Figure 4.5 and on a slice of the volume mesh in Figure 4.6. The *Trex* algorithm appears to have difficulty maintaining anisotropic cells near abrupt changes in the geometry. Anisotropic cell generation halts early on the grid line extending from the missile-fin interface. The block generated by the *Trex* scheme contained 64,200,000 elements.



(a) x-y plane view of conical missile mesh.



(b) y-z plane view of conical missile mesh.

Figure 4.4: *Trex* block of conical missile mesh.

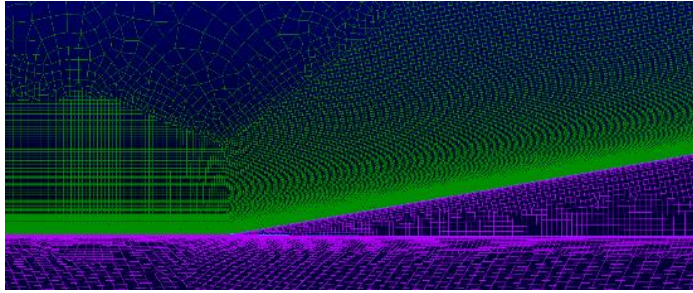


Figure 4.5: Prism layers created by *Trex* on the symmetry line near the missile fin.

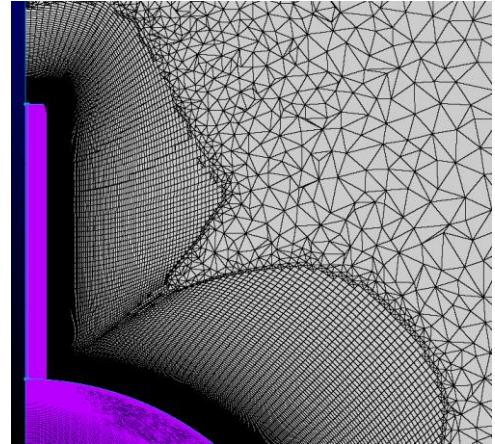


Figure 4.6: Slice of volume mesh around missile fins to view prism layers created by *Trex*.

An additional block was extruded from the boundaries of the block created from the *Trex* scheme. All of the boundaries except for the outflow and symmetry boundary were selected for extrusion. The extruded mesh contained hexagonal elements and allowed for the same mesh to be used for all angles of attack. The extruded block also served to align the flow with the internal block. The resulting 3D grid contained a total of 64,600,000 cells with 49,600,000 hexahedral cells and 1,000,000 triangular prism cells with the remaining cells consisting of tetrahedral and pyramid elements.

The images taken from the conic missile-fin configuration are representative of other configurations. An additional mesh was made for the conic missile-fin +1 configuration, shown in Figure 4.8. The anisotropic cell growth on the surface mesh from the connectors is the same as the base conic configuration. The generated surface mesh contained 390,000 quadrilateral elements and 6300 elements, totaling 396,300 surface elements. The maximum area ratio was maintained below 4.85. Parameters for the growth of the prism layer were the same as the base conic configuration. The block generated by *Trex* totaled 61,300,000 cells. An extruded block was generated from the *Trex* block boundaries. The resulting grid totaled 61,900,000 cells containing 44,500,000 hexahedrals and 900,000 triangular prisms with the remaining cells of tetrahedral and pyramid type. Although the general form of the mesh is the same as the base conic missile configuration, a slice through the volume block seen in Figure 4.9 shows that the prism

layer growth stopped early on the symmetry boundary, revealing another issue the *Trex* algorithm has: resolving anisotropic cells on symmetry boundaries.

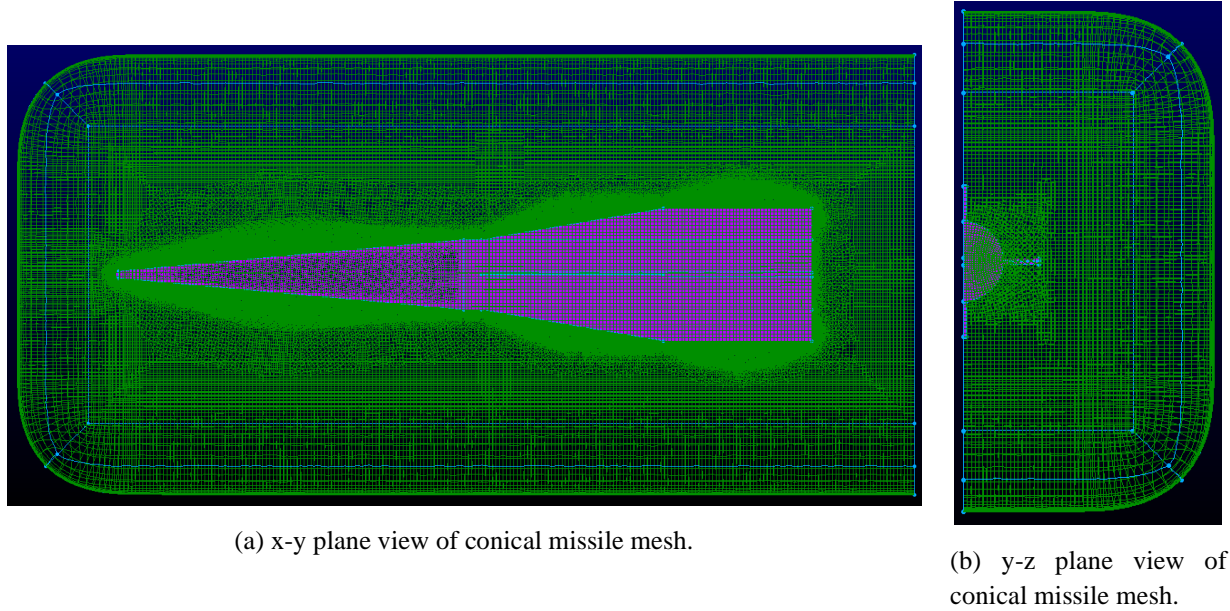


Figure 4.7: Main block of conical missile mesh.

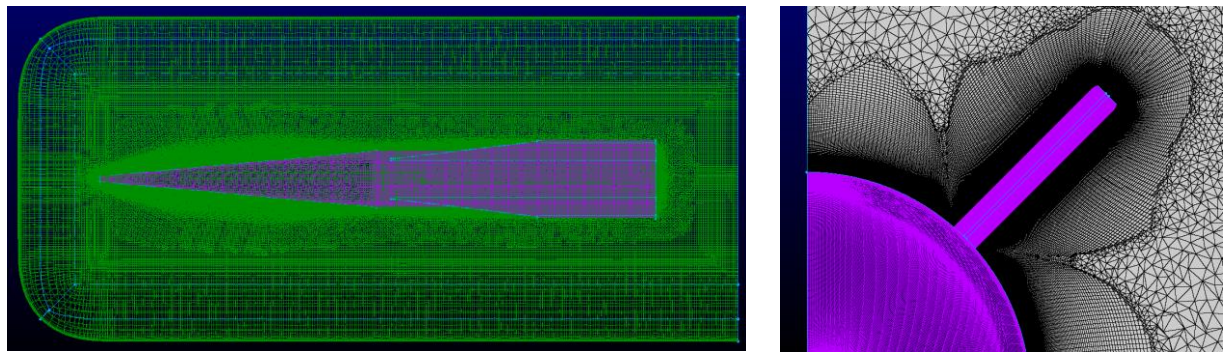


Figure 4.8: Main block of conic missile mesh +1 configuration.

Figure 4.9: Slice of volume mesh in conic missile +1 configuration to view prism layers around missile fin.

The mesh generated for the ogive missile-fin configuration is similar to the conic missile except for the discontinuity the conic missile configuration has that signifies the end of the nose cone. The ogive missile curve is tangent to the remaining missile geometry at this point. This alleviates issues from *Trex* in this region since the geometry of the missile has a smooth transition

instead of an abrupt change. The surface mesh was generated with an initial anisotropic cell height of 0.1 mm . The final surface mesh contained 225,000 quadrilaterals and 5000 triangular cells for a total of 260,000 surface elements. The maximum area ratio on the surface was measured at 5.2. The block generated by *Trex* implemented the same spacing growth rate and initial cell height as the conic missile-fin configuration. A sponge layer was extruded from the block created by the *Trex* scheme to permit use of the mesh for all positive angles of attack. The resulting mesh is seen in Figure 4.10. The grid totaled 46,400,000 cells with 36,800,000 hexahedral elements and 800,000 triangular prisms with the remainder cells of the tetrahedral and pyramid type.

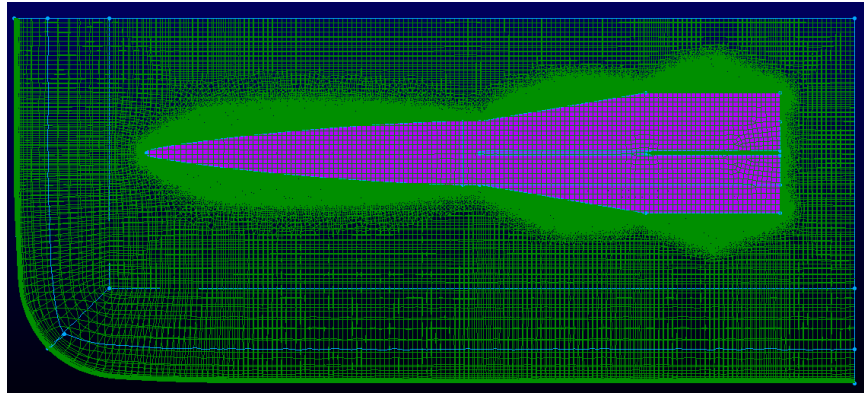


Figure 4.10: Main block of ogive missile mesh.

An additional mesh was made for the ogive missile-fin +1 configuration, shown in Figure 4.11. The anisotropic cell growth on the surface mesh from the connectors is the same as the conical configuration. The generated surface mesh contained 400,000 quadrilateral elements and 6500 elements, totaling 406,500 surface elements. The maximum area ratio was maintained below 4.8. Parameters for the growth of the prism layer were the same as the conic configuration in the creation of the first block. An extruded block was generated from the *Trex* block boundaries. The resulting grid totaled 61,400,000 cells containing 45,900,000 hexahedrals and 940,000 triangular prisms with the remaining cells of tetrahedral and pyramid type. The general form of the prism layers between the fin is the same as the conic +1 missile-fin configuration in Figure 4.9.

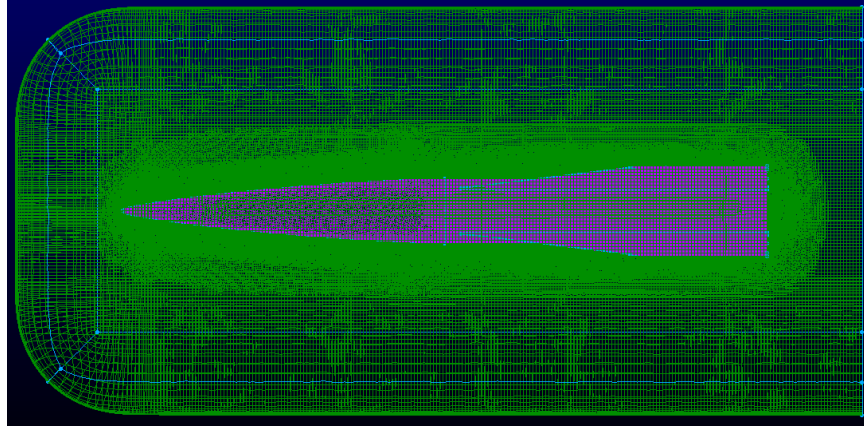


Figure 4.11: Main block of ogive missile +1 configuration.

The missile configurations were simulated in Kestrel version 11.1rc5 with a RANS solver employing the Spalart-Allmaras turbulence model. Each missile was solved at three angles of attack, 0° , 1° , and 10° with the same input options. A summary of key input parameters is shown in Table 4.1. A CFL number of 100 was employed to increase convergence speed. Second-order numerical schemes were selected to improve accuracy of the solution.

The appropriate boundary conditions were set to ensure good performance. The symmetry plane was set to a symmetry boundary; the missile body and fins were set to an adiabatic, no-slip wall; the boundary downstream of the end of the missile was set to a sink boundary condition, and a farfield boundary condition was imposed on the remaining boundaries. The sink boundary condition allows for different methods of an outflow boundary condition to be enforced (e.g., static pressure outlet, mass flow outlet). The presented simulations implemented an extrapolated outlet.

Table 4.1: Key inputs simulating the Mach 3.64 nozzle with a test section and test article in Kestrel.

Model	RANS
Turbulence model	SA
Gas model	5-Species gas
Re/L	6.15E6
Freestream Mach number	5.9
Freestream temperature	54 K
Spatial accuracy	2 nd -order
Transition temporal accuracy	2 nd -order
Turbulence spatial accuracy	2 nd -order
Slope limiter	Venkatakrisnan
Inviscid flux scheme	HLLE+
Viscous flux scheme	LDD+
Convective flux scheme	HLL

4.2 CFD Results

The results of the CFD simulations are presented in groups by configuration. All angles of attack are displayed together for comparison. The first configuration presented is the conic missile-fin configuration, followed by the conic +1, ogive, and ogive +1 configurations. General behavior of the flow is identified and then an assessment of the SBLI and complex flow structures is made. Additional plots of the flowfield for each configuration are located in APPENDIX A: Results of hypersonic missile-fin configurations.

The y^+ value is plotted for the first cell on the conic missile configuration in Figure 4.12 to confirm the grid spacing from the wall is small enough to resolve the boundary-layer without the use of wall functions. The plot presents values on the missile surface along a slice at $z = 0.003937$ inches (parallel to the symmetry plane). The maximum wall y^+ is about 1.2 and occurs at the nose tip. The y^+ term drops immediately downstream of the nose and maintains a value below 0.2. The spikes in the plot indicate locations of shock waves and expansion fans. The value

was proven sufficiently low enough to compute the boundary-layer flow on the entire missile. The y^+ value shown here is used to represent the other simulations – though the magnitude of the y^+ value may increase, it should remain below a nominal value of 1 for all configurations at all angles of attack.

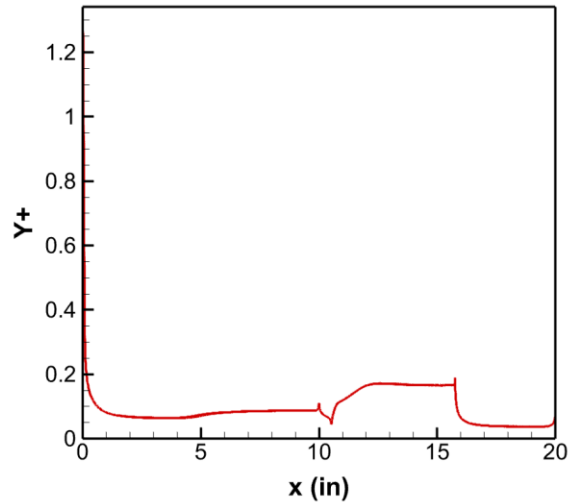


Figure 4.12: Surface y^+ value for the first cell spacing on the conic missile-fin configuration at $z = 0.003937$ in.

The overall flow structure of the conic missile is captured by the density gradient magnitude contours in Figure 4.13. A bow shock is seen in front of the nose and an entropy layer appears at 0° angle of attack. The entropy layer continues downstream and casts an “envelope” around the missile body which eventually blends with the boundary-layer. An expansion fan forms at the end of the conical nose and the beginning of cylindrical section. The expansion fan is seen to interact with the boundary-layer. A shock wave forms near the base of the fin and expansion fans appear on the fin tip leading and trailing edges. A turbulent boundary-layer is seen from the front of the missile to the fin-body interface. The boundary-layer height decreases considerably on the fin. The shock strength around the fin increases on the bottom and decreases on the top as the missile begins to increase its angle of attack to 1° . This is due to the increase of velocity which can be seen in the Mach contours in Figure 4.14. The shock initiated by the fin also appears to oscillate over time. The increase in the angle of attack to 10° shows separation of the flow due to the high angle of attack. An oblique shock appears to form on the nose downstream of the bow shock. Figure 4.13 (c) shows complex flow structures forming upstream of the fin on the upper

surface and high-density gradients on the lower surface. The large density gradients appear primarily behind the expansion fan on the end of the nose and the between the shock wave and Fin 3.

Mach and temperature contours of the missile are shown in Figure 4.14. High temperature regions occur in the corner between the fins and missile body and continue downstream. The areas with the highest surface temperature occur close to the fins with 0° and 1° angle of attack. The high surface temperatures on the missile at 10° AoA can be attributed to the separated flow.

Figure 4.15 shows the Mach number and density gradient magnitude contours rotated about the y-axis 30° with a slice at $x = 15.79$ inches. A general distribution of the boundary-layer height can be visualized Figure 4.15 (a) and (b) before separation begins at the high AoA. The boundary-layer height decreases in the region of the fins and corners and increases to about halfway between the fins. The boundary-layer height also appears to decrease towards the fin tips. Figure 4.15 (c) shows a clear image where separation occurs. The boundary-layer on between Fin 1 and Fin 2 is disrupted and regions of circulating flow can be seen on the slice in regions where the Mach number is low. A tip vortex is also seen around Fin 2. The slice in Figure 4.15 (f) shows an attached boundary-layer on the corner of Fin 3 and the missile body and boundary-layer separation on the corner of Fin 2 and the missile body.

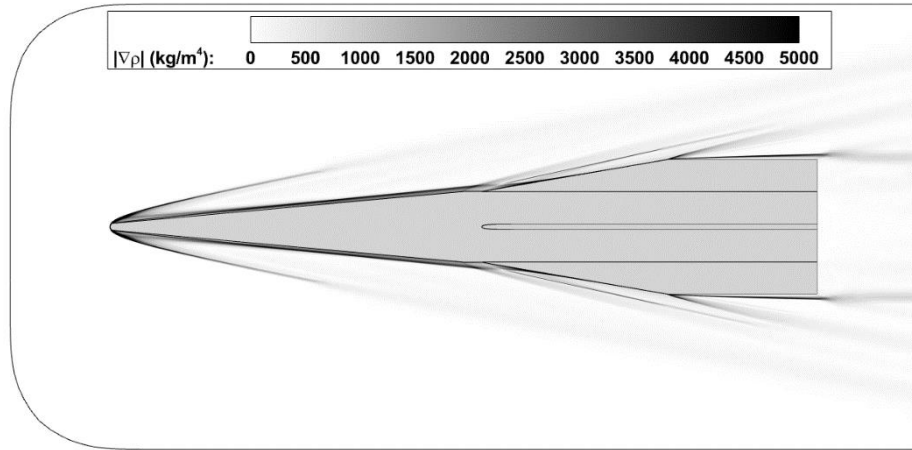
The development of the flow can be visualized by comparing Figure 4.15 to Figure 4.16. Figure 4.16 shows Mach and density gradient contours for all angles of attack with a slice at $x = 17.26$ inches. The 3D expansion fans are seen on the leading edge of the fin tips for all fins in Figure 4.16 (a)-(d) and on Fin 3 in Figure 4.16 (e) and (f). The slice in Figure 4.16 (a)-(d) also displays a good boundary of the upstream shocks and expansion fans. The shocks formed around the fins' blunt edge sweep with the fin and appear to have an interaction which is best visualized in Figure 4.16 (c) and (d) between Fin 2 and Fin 3. Figure 4.16 (e) and (f) show the development of the flow around Fin 1 and Fin 2. The size and radial location of the bubble on Fin 2 appears to be the same. The complex flow between the shock on Fin 2 and Fin 3 appears to be contained between the shock and the expansion fan created on the wing tip.

The pressure, temperature, and skin friction coefficient magnitude of the missile surface is plotted in Figure 4.17, Figure 4.18, and Figure 4.19 respectively. Figure 4.17 (a), Figure 4.18 (a), and Figure 4.19 (a) plot the surface values taken on a slice at $z = 0.003937$ inches. This slice is located on the section of the fin where the blunt edge is perpendicular to the flow and is necessary since Tecplot was unable to plot the surface values on the symmetry plane. Figure 4.17 (b),

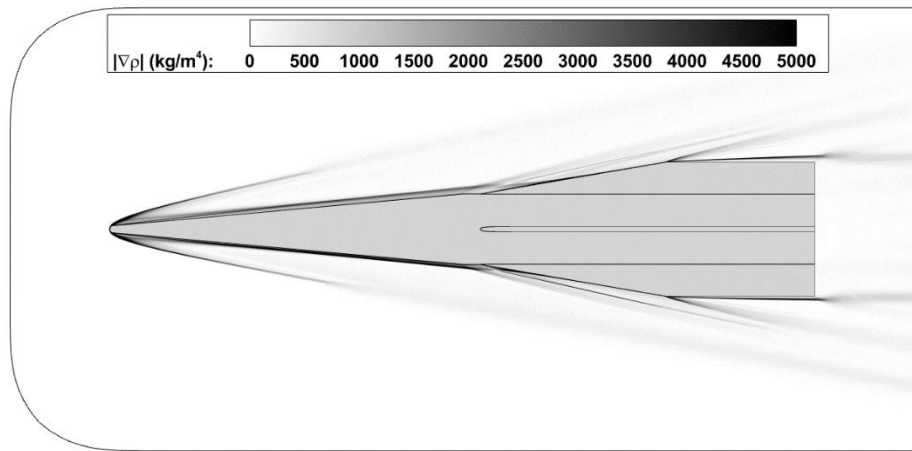
Figure 4.18 (b), and Figure 4.19 (b) plot the surface values taken from a slice 45° between Fin 1 and Fin 2, indicated as “upper”, and 45° between Fin 2 and Fin 3, indicated as “lower”. Only the lower slice was plotted for an AoA of 0° since the flow is symmetrical. The values upstream of the fins (i.e., about 10.5 inches) are the same for the respective angles of attack for all plots. A line plotted with a constant value in Figure 4.17 (b) represents the freestream pressure. The freestream pressure is not seen on the surface of the missile where the slice was extracted; therefore, it is assumed that Tecplot recorded the freestream value along with the surface values when the slices were extracted.

The pressure, temperature, and skin friction plots show display discontinuities at abrupt changes in the geometry. The pressure on the lower surface of the missile increases with AoA and the pressure on the upper surface decreases with AoA. The pressure in Figure 4.17 (a) at 0° AoA decreases after the expansion fan at $x = 10$ inches and begins to increase after the shock in front of the fin. The pressure on the fin’s surface continues to increase and reaches almost a constant value until the fin tip, around $x = 16$ inches, where another expansion fan occurs. Pressure then drops to a minimum and steadily increases again. The behavior at the increased AoA is similar to the 0° AoA case, but with a greater change in magnitude near flow discontinuities. The pressure in Figure 4.17 (b) drops after the initial expansion fan to a near steady value for the 0° and 1° cases and increases again in the 10° case.

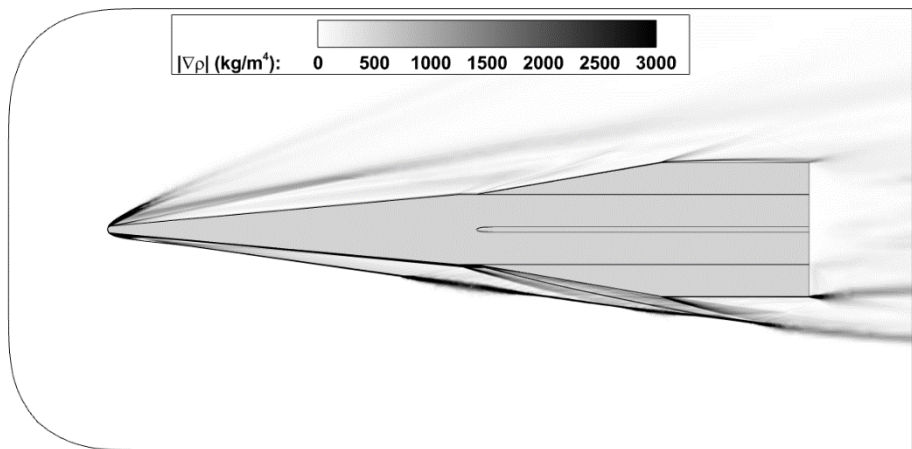
The skin friction coefficient in Figure 4.19 (a) spikes after the expansion fans and drops after shock waves. The skin friction on the fins’ leading edge increases to a peak. The peak C_f on the fins at a 0° and 1° AoA is nearly constant until the expansion fan on the fin tip. The C_f observed on Fin 1 at a 10° AoA oscillates because of the separated flow. The expansion fan at the fin tip causes a spike in the C_f before it drastically drops. The C_f in Figure 4.19 (b) does not exhibit a significant change in magnitude after the initial expansion fan.



(a) $AoA = 0^\circ$

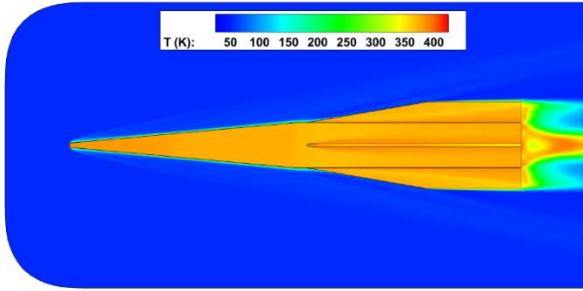


(b) $AoA = 1^\circ$

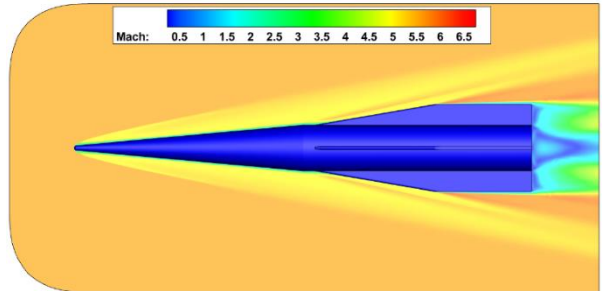


(c) $AoA = 10^\circ$

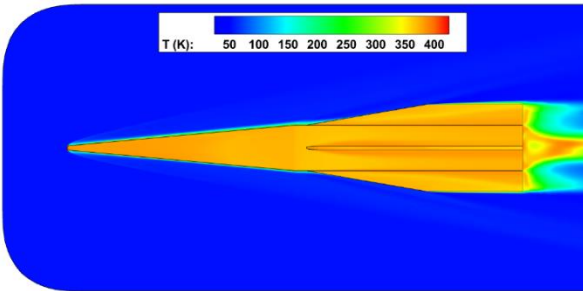
Figure 4.13: Density gradient magnitude contours of conic missile configuration at various angles of attack.



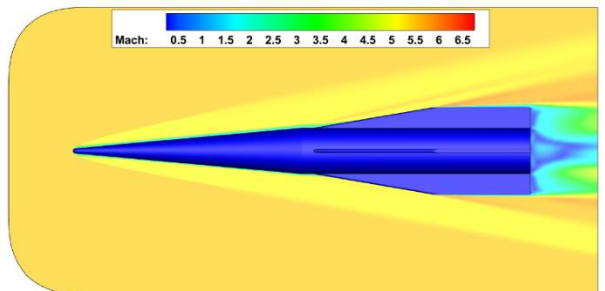
(a) $AoA = 0^\circ$



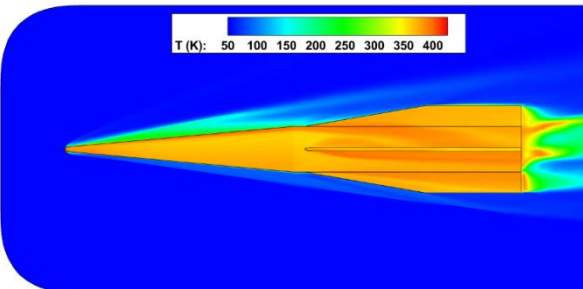
(d) $AoA = 0^\circ$



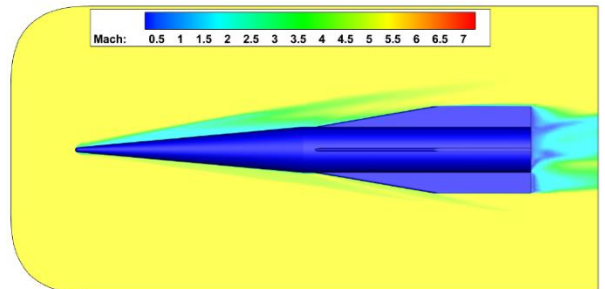
(b) $AoA = 1^\circ$



(e) $AoA = 1^\circ$

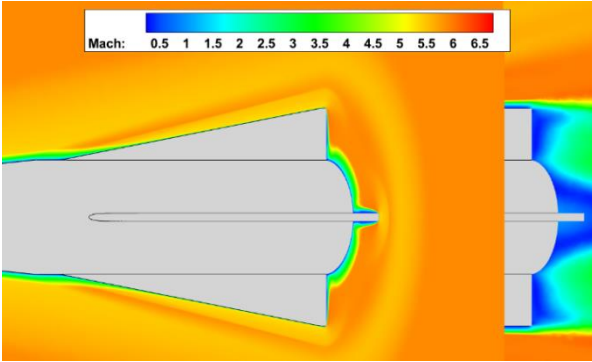


(c) $AoA = 10^\circ$

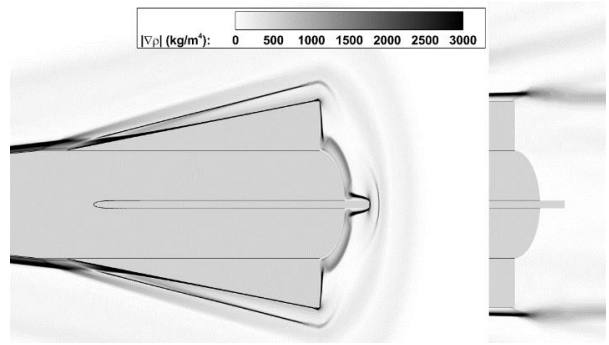


(f) $AoA = 10^\circ$

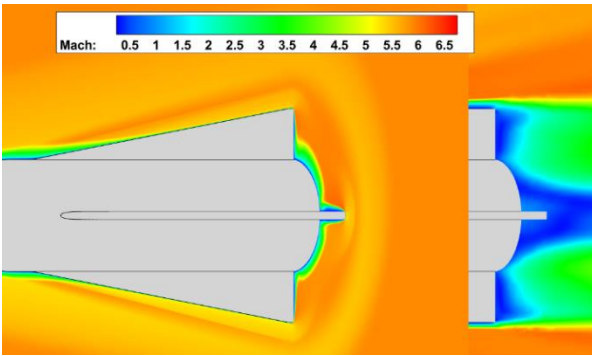
Figure 4.14: Contours of the conical missile of Temperature (a)-(c) and Mach number (d)-(f) at various angles of attack.



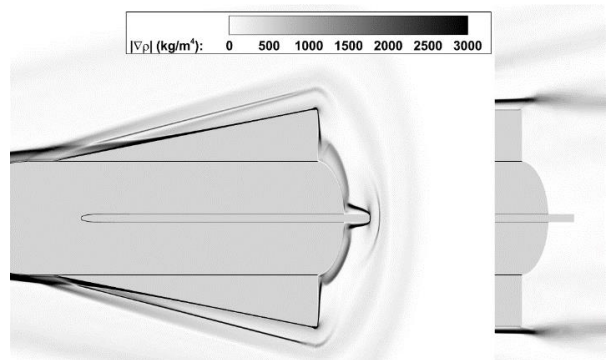
(a) $AoA = 0^\circ$



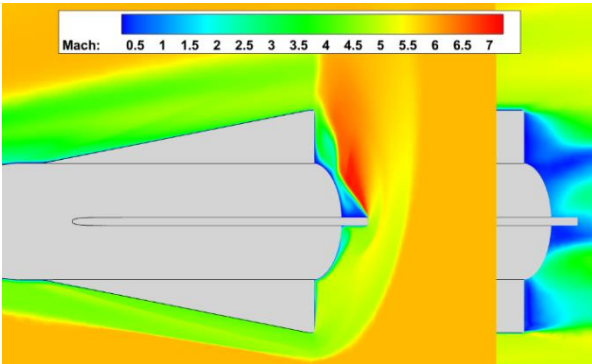
(d) $AoA = 0^\circ$



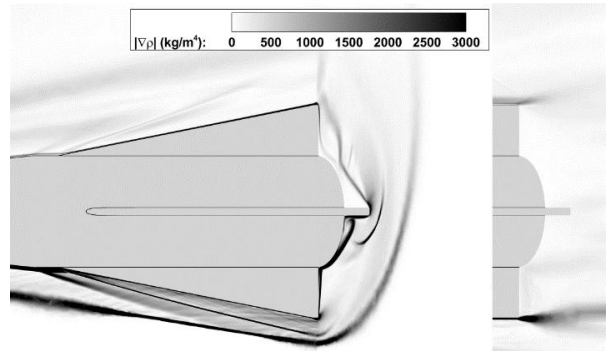
(b) $AoA = 1^\circ$



(e) $AoA = 1^\circ$

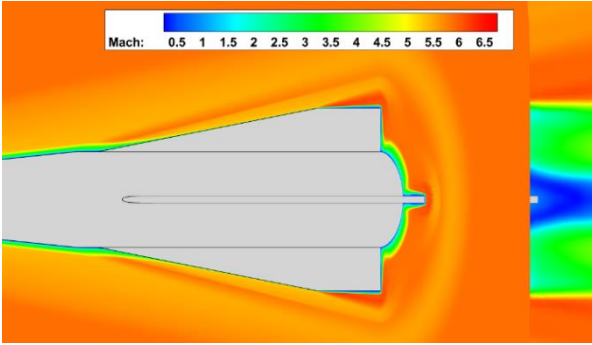


(c) $AoA = 10^\circ$

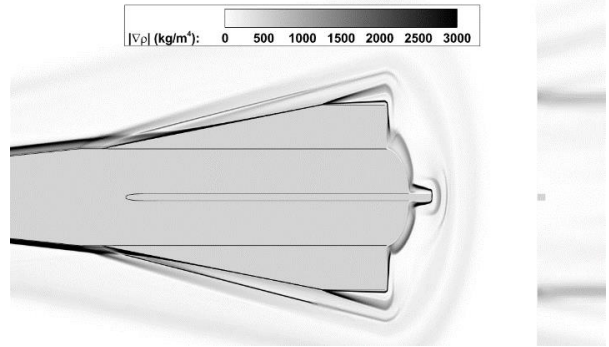


(f) $AoA = 10^\circ$

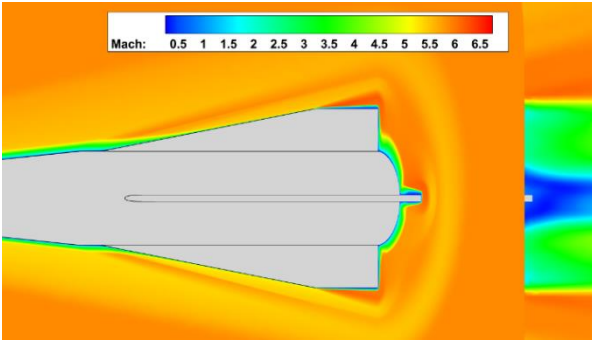
Figure 4.15: Contours of the conical missile of Mach number (a)-(c) and density gradient magnitude (d)-(f) at various angles of attack with a slice at $x = 15.79$ in.



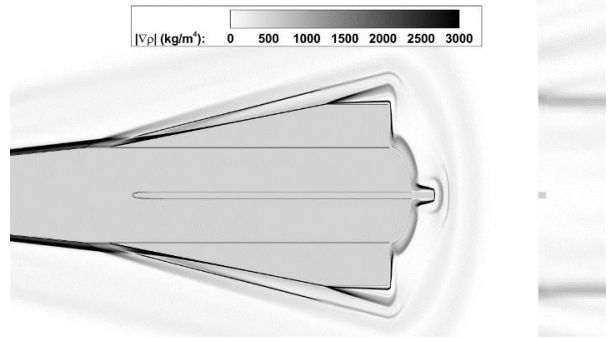
(a) $AoA = 0^\circ$



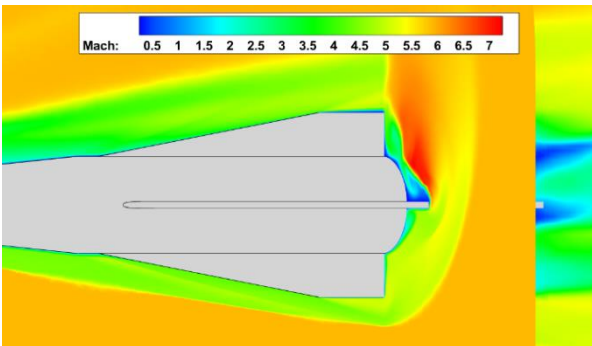
(d) $AoA = 0^\circ$



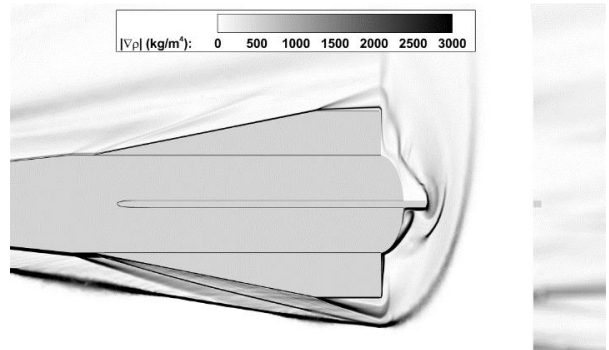
(b) $AoA = 1^\circ$



(e) $AoA = 1^\circ$

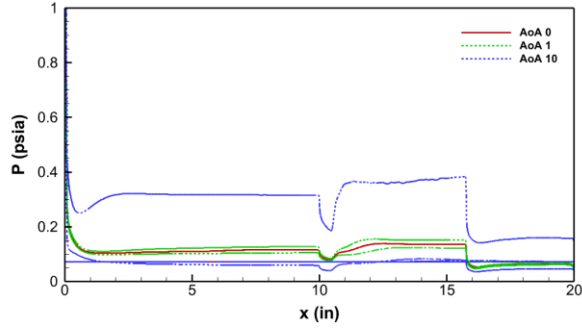


(c) $AoA = 10^\circ$

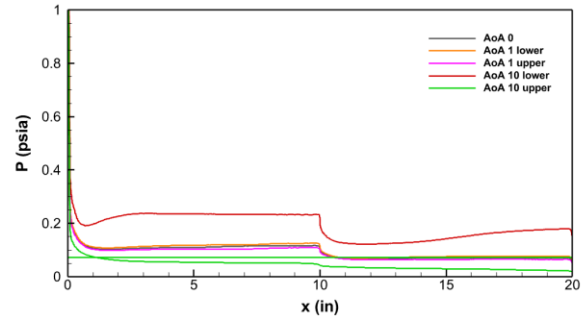


(f) $AoA = 10^\circ$

Figure 4.16: Contours of the conical missile of Mach number (a)-(c) and density gradient magnitude (d)-(f) at various angles of attack with a slice at $x = 17.26$ in.

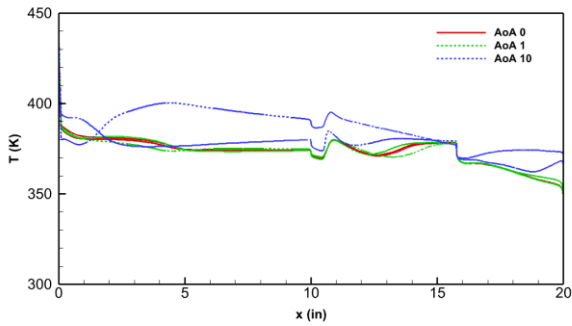


(a) Surface values at $z = 0.003937$ in.

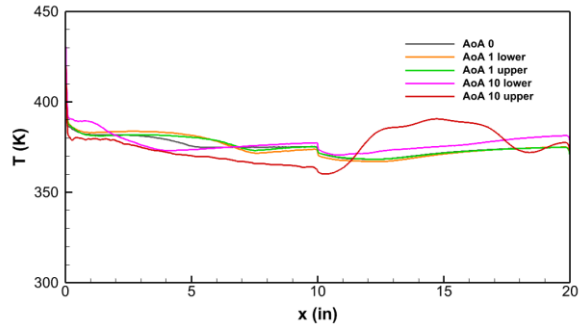


(b) Surface values at slices 45° between Fin 1 and Fin 2 (upper) and 45° between Fin 2 and Fin 3 (lower).

Figure 4.17: Pressure distribution along slices parallel to the symmetry boundary (a) and 45° between fins (b) in conic missile configuration.

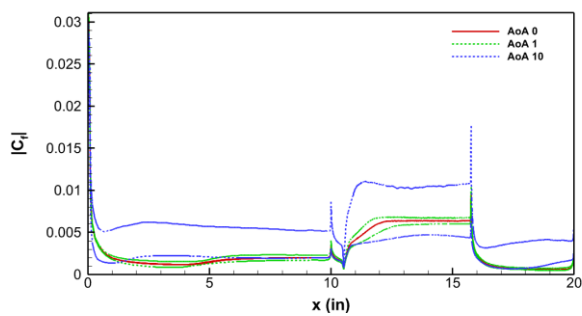


(a) Surface values at $z = 0.003937$ in.

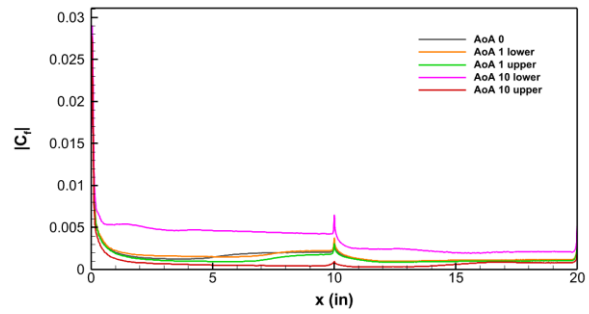


(b) Surface values at slices 45° between Fin 1 and Fin 2 (upper) and 45° between Fin 2 and Fin 3 (lower).

Figure 4.18: Temperature distribution along slices parallel to the symmetry boundary (a) and 45° between fins (b) in conic missile configuration.

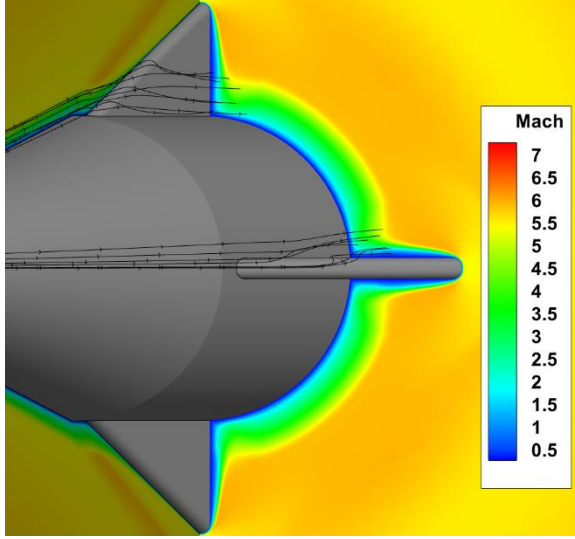


(a) Surface values at $z = 0.003937$ in.

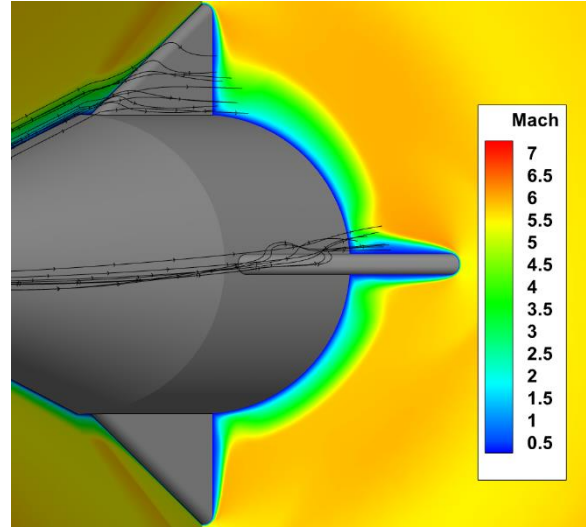


(b) Surface values at slices 45° between Fin 1 and Fin 2 (upper) and 45° between Fin 2 and Fin 3 (lower).

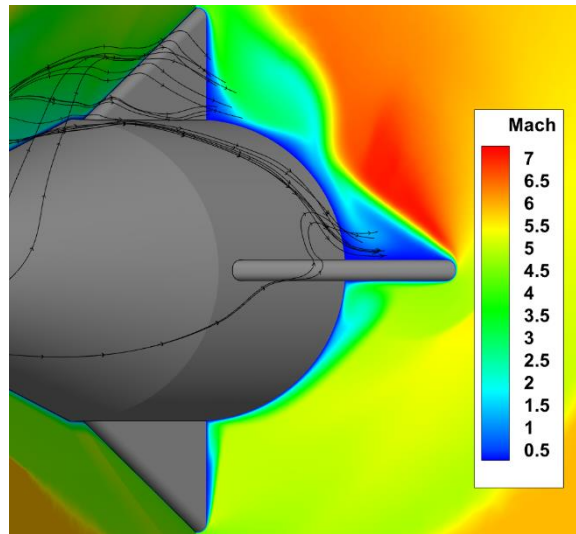
Figure 4.19: Skin friction coefficient magnitude along slices parallel to the symmetry boundary (a) and 45° between fins (b) in conic missile configuration.



(a) $AoA = 0^\circ$



(b) $AoA = 1^\circ$



(c) $AoA = 10^\circ$

Figure 4.20: Mach number contour with a slice at $x = 14.8$ in and velocity streamtraces on conic missile-fin configuration.

The temperature in Figure 4.18 (a) for the 0° and 1° AoA cases decreases linearly from the stagnation point on the front of the nose to $x = 1$ inch. The surface temperature continues to drop at a decreased rate. The rate of temperature drop decreases again at $x = 5$ inches where the edge of the entropy layer and boundary-layer appear to merge. The surface temperature is nearly constant from $x = 5$ inches to $x = 10$ inches where an expansion fan causes a sudden drop in

temperature. The temperature peaks after the shock in front of the fins and immediately begins to drop to a minimum value located less than halfway along the fin's leading edge before increasing until the fin tip on the leading edge. The temperature at this point reaches around 370 K for all cases and all fins. The temperature drops after the expansion fan until the end of the missile.

The temperature in Figure 4.18 (a) for the 10° AoA case starts to show a decrease on the upper and lower surfaces until ~1.8 inches. The temperature on the upper surface increases because of the upstream oblique shock formed around the nose. The temperature continuously decreases on the upper surface for the remainder of the missile, except for instances where a shock temporarily increases the temperature. Figure 4.18 (b) shows the temperature increase on the upper surface after $x = 10$ inches because of the separated flow.

Mach contours with velocity streamtraces on the conic missile-fin configuration are shown in Figure 4.20 at a 0° AoA in (a), 1° AoA in (b), and a 10° AoA in (c). The model is rotated 80° about the y-axis and has a slice take at $x = 0.37$ inches. The streamtraces show the mean flow path of the velocity on the missile. The streamtraces in Figure 4.20 (a) show a relatively simple motion of the flow. The flow from the upstream boundary-layer on the nose may move in a small spiral motion downstream after it encounters the missile fin. Recirculation does not occur at the base of the fin leading edge, which agrees with the idea that SBLI on a low-angle ramp in a high Reynolds number flow may not have a separation bubble [20]. The flow in this region maintains a low positive velocity. The amount of spiral motion increases with an increase of AoA as seen in Figure 4.20 (b). Streamtraces move around the fin and circulate back to the fin sidewall as it continuously flows downstream. The streamtraces in Figure 4.20 (c) show clear motion towards the separated regions. Some of the streamtraces wrap around the missile nose after impinging on the nose and add to the flow three-dimensionality on the missile fin.

The density gradient magnitude contours of the conic +1 missile-fin configuration are shown in Figure 4.21. The major flow structures (e.g., shock waves and expansion fans) on the missile are the similar to the base conic configuration. The flowfield shows the bow shock formed upstream of the nose and an expansion fan at the end of the nose at $x = 10$ inches. The resulting Mach and temperature contours in Figure 4.22 match the expected flowfield seen in Figure 4.21. The flowfield upstream of $x = 10$ inches is the same in Figure 4.13 and Figure 4.21.

Figure 4.23 and Figure 4.24 show the Mach and density gradient contours rotated about the y-axis 30° with a slice at $x = 15.79$ inches and $x = 17.26$ inches respectively. Figure 4.23 (a)

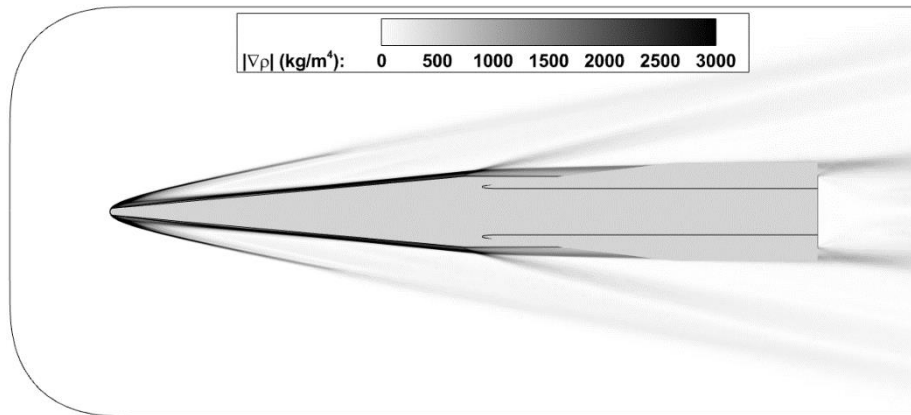
and Figure 4.24 (a) show the same results as Figure 4.15 (a) and Figure 4.16 (a) but at a different perspective. Figure 4.23 (b) and (c) and Figure 4.24 (b) and (c) start to show the result of the 45° roll. The flow over Fin 2a separates on the sidewall in Figure 4.23 (b) and Figure 4.24 (b). The flow in Figure 4.23 (c) and Figure 4.24 (c) show a vortex core on the sidewalls of Fin 1a and Fin 2a. Tip vortices also form on both fins.

The pressure, temperature, and C_f are plotted in Figure 4.25, Figure 4.26, and Figure 4.27 respectively. The plots in (a) show the surface values for a slice taken at $z = 0.003937$ inches, and the plots in (b) show the surface values of slices rotated 45° clockwise and counterclockwise from the symmetry plane. The values of all parameters shown in Figure 4.25, Figure 4.26, and Figure 4.27 for the 0° AoA case are the same as the base conic missile-fin configuration in Figure 4.17, Figure 4.18, and Figure 4.19 respectively.

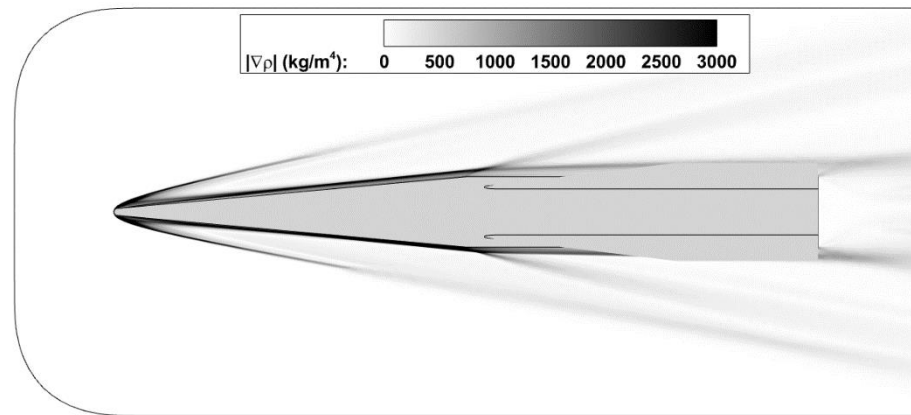
The pressure on all AoA for both configurations of the conical missile are nominally the same shape on the slices taken where fins do not exist, i.e., the plots in Figure 4.17 (b) and Figure 4.25 (a), but with a decreased magnitude with increased angle attacked when comparing the base conic configuration to the conic +1 configuration. The reverse trend is seen when comparing in Figure 4.17 (a) and Figure 4.25 (b), except for the lower surface on Figure 4.25 (b) at a 10° AoA. The lower surface in Figure 4.25 (b) at 10° AoA does not appear to be influenced by a shock wave.

The skin friction coefficient in Figure 4.27 (b) follows the general trend in Figure 4.19 (a). The oblique shock formed on the upper surface of the nose at 10° AoA does not influence the C_f in Figure 4.27 (b) as much as Figure 4.19 (a) because of the 45° roll. The C_f on the upper surface also does react as strongly to flow discontinuities. The C_f on the leading edge of Fin 1a is lower than Fin 1 at a 10° AoA. Fin 1a has a slight overshoot of the C_f after the shock at 1° AoA which did not exist on Fin 1.

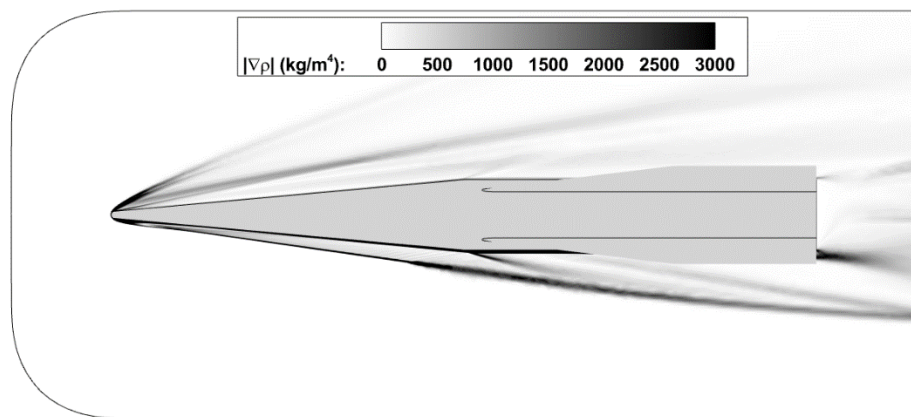
The temperature on the conic +1 configuration increases on the lower surface from the base conic configuration when flow is attached. The temperature in the separated flow on the upper surface of the missile at a 10° AoA continuously decreases as shown in Figure 4.26 (b). The temperature on the nose in Figure 4.26 (a) is larger than the temperature in Figure 4.18 (a) despite that both values were extracted from the same slice location. It is assumed that the difference is the result of the influence of the fins downstream.



(a) $AoA = 0^\circ$

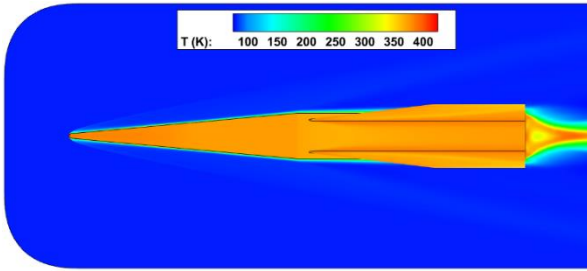


(b) $AoA = 1^\circ$

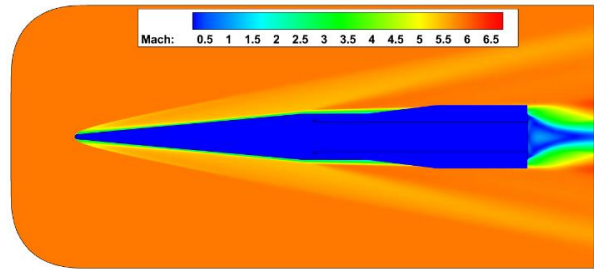


(c) $AoA = 10^\circ$

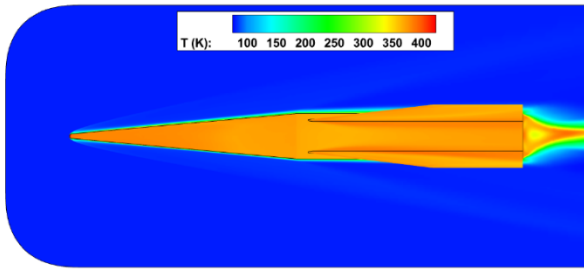
Figure 4.21: Density gradient magnitude contours of conic missile +1 configuration at various angles of attack.



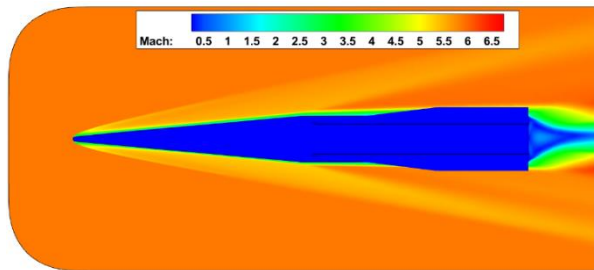
(a) $AoA = 0^\circ$



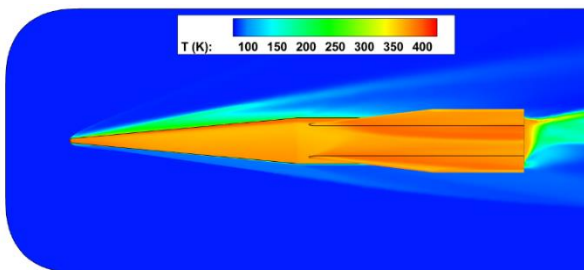
(d) $AoA = 0^\circ$



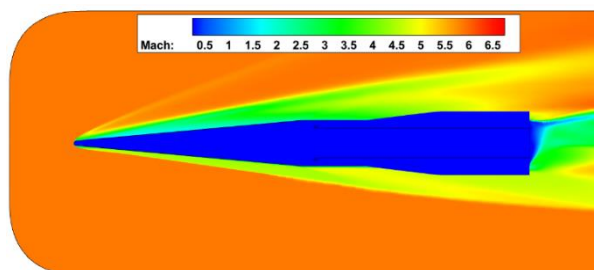
(b) $AoA = 1^\circ$



(e) $AoA = 1^\circ$

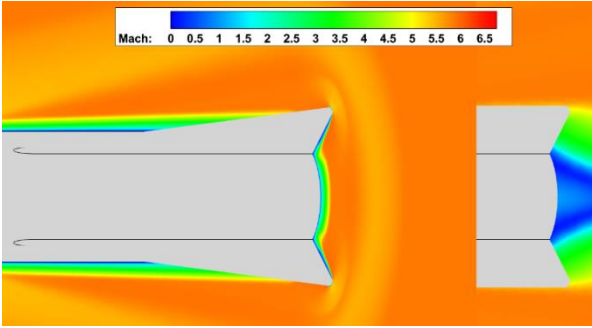


(c) $AoA = 10^\circ$

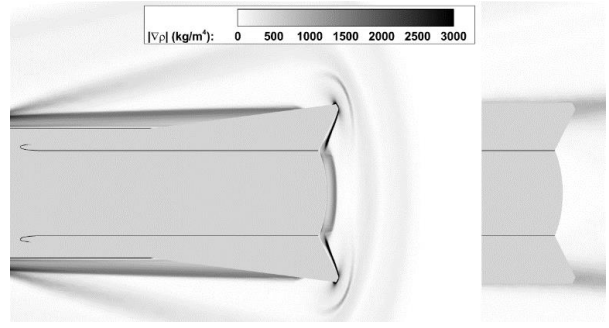


(f) $AoA = 10^\circ$

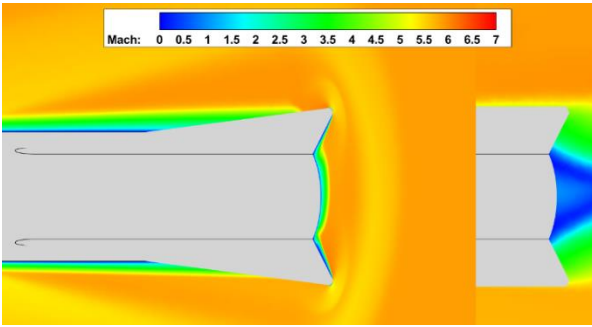
Figure 4.22: Contours of the conic missile +1 configuration of Temperature (a)-(c) and Mach number (d)-(f) at various angles of attack.



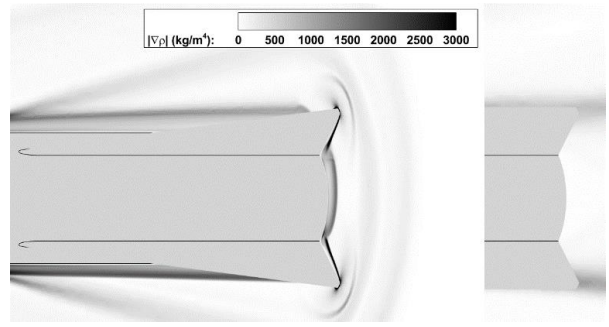
(a) $AoA = 0^\circ$



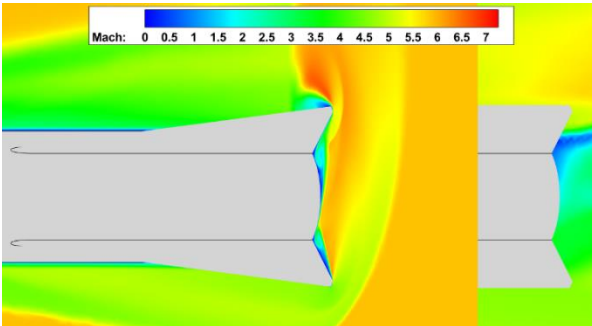
(d) $AoA = 0^\circ$



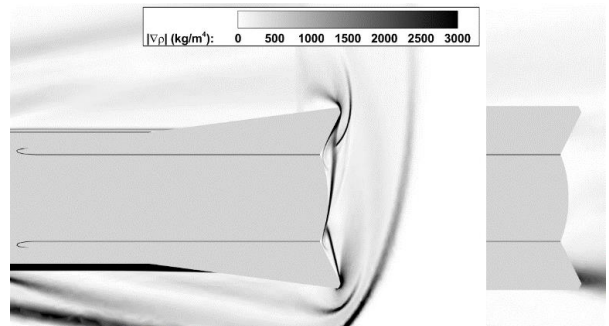
(b) $AoA = 1^\circ$



(e) $AoA = 1^\circ$

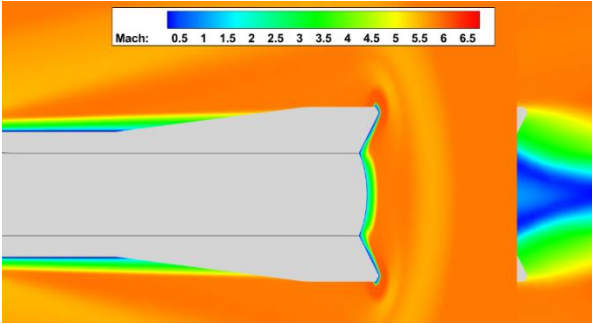


(c) $AoA = 10^\circ$

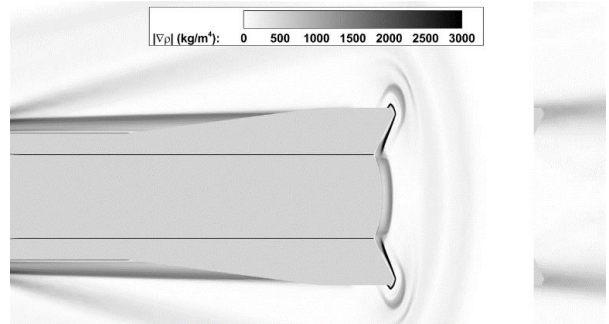


(f) $AoA = 10^\circ$

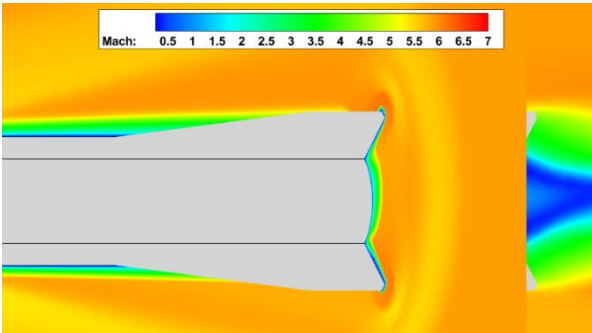
Figure 4.23: Contours of the conic missile +1 configuration of Mach number (a)-(c) and density gradient magnitude (d)-(f) at various angles of attack with a slice at $x = 15.79$ in.



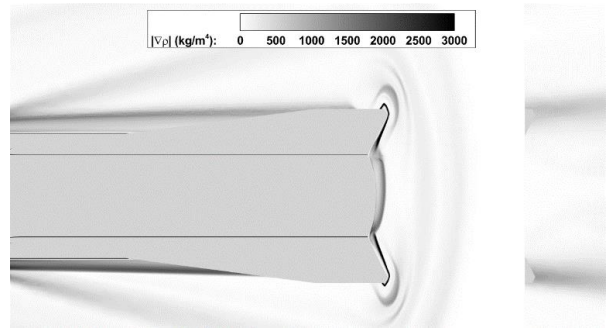
(a) $AoA = 0^\circ$



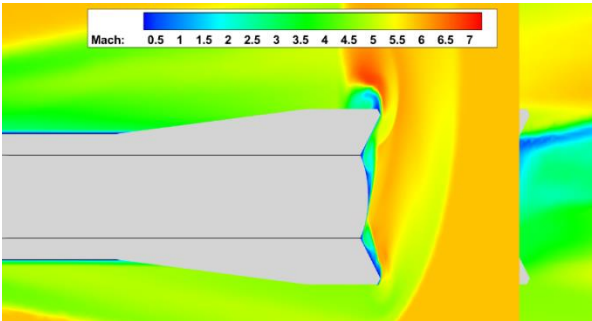
(d) $AoA = 0^\circ$



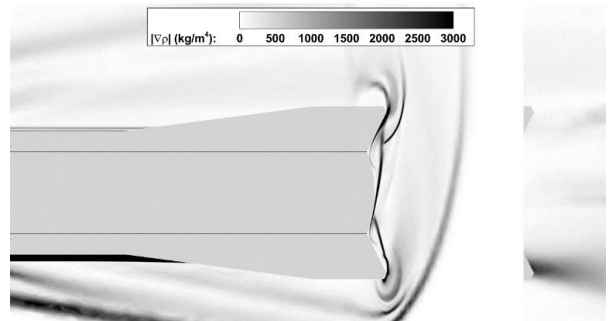
(b) $AoA = 1^\circ$



(e) $AoA = 1^\circ$

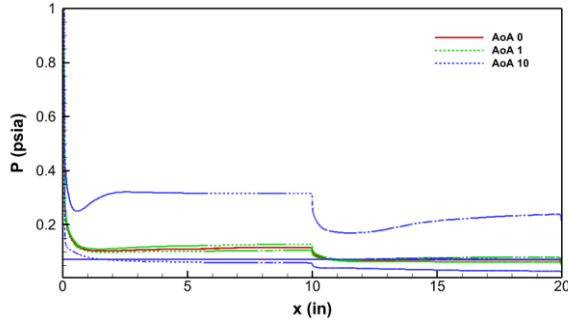


(c) $AoA = 10^\circ$

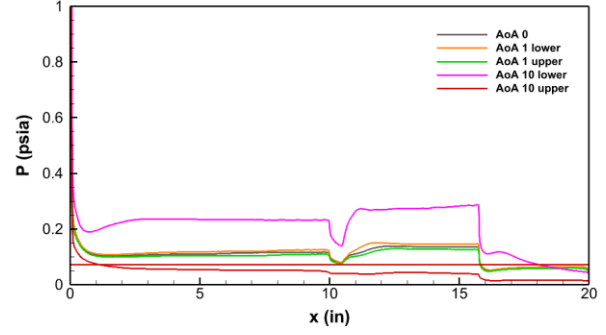


(f) $AoA = 10^\circ$

Figure 4.24: Contours of the conic missile +1 configuration of Mach number (a)-(c) and density gradient magnitude (d)-(f) at various angles of attack with a slice at $x = 17.26 \text{ in.}$

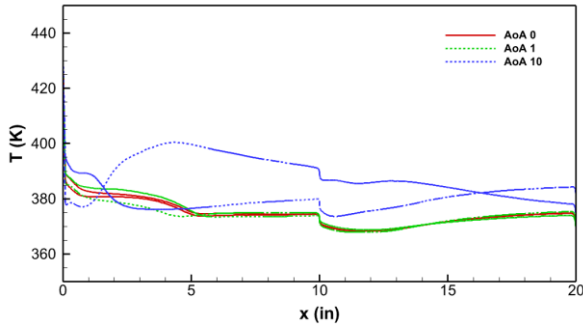


(a) Surface values at $z = 0.003937$ in.

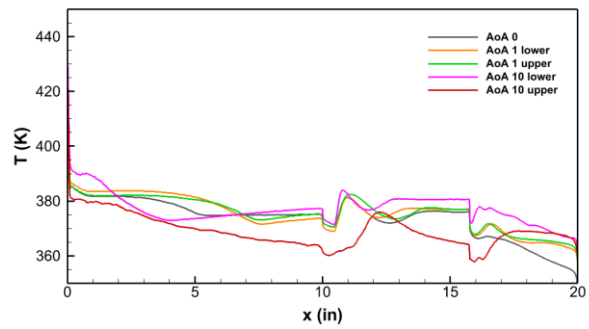


(b) Surface values at slices on Fin 1a (upper) and Fin 2a (lower).

Figure 4.25: Pressure distribution along slices parallel to the symmetry boundary in conic missile +1 configuration (a) and slices on Fin 1a and Fin 2a (b).

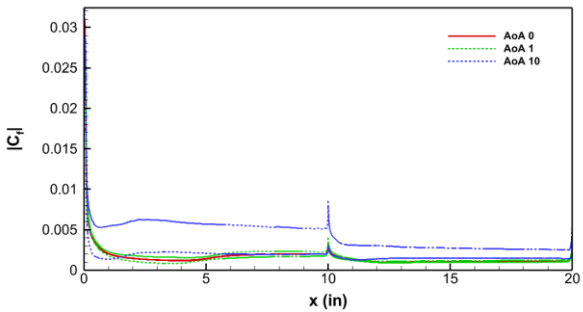


(a) Surface values at $z = 0.003937$ in.

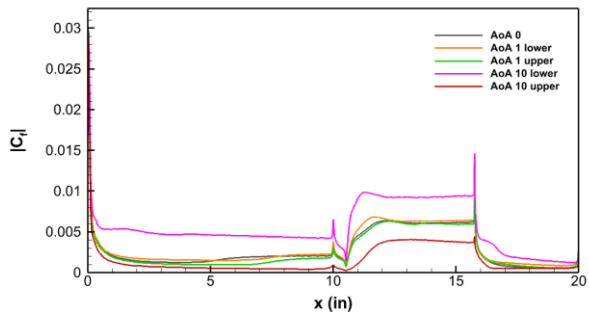


(b) Surface values at slices on Fin 1a (upper) and Fin 2a (lower).

Figure 4.26: Temperature distribution along slices parallel to the symmetry boundary in conic missile +1 configuration (a) and slices on Fin 1a and Fin 2a (b).

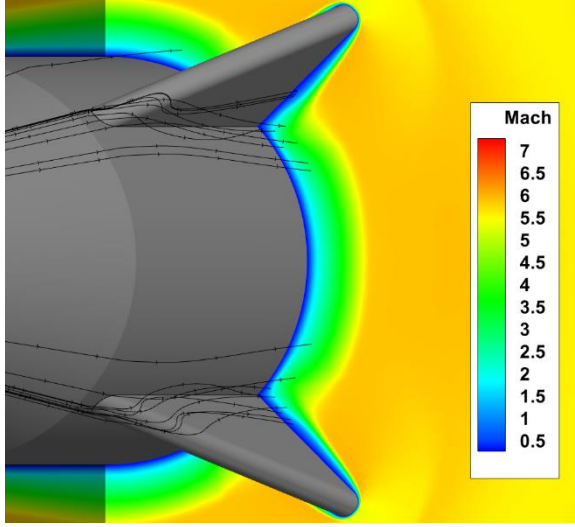


(a) Surface values at $z = 0.003937$ in.

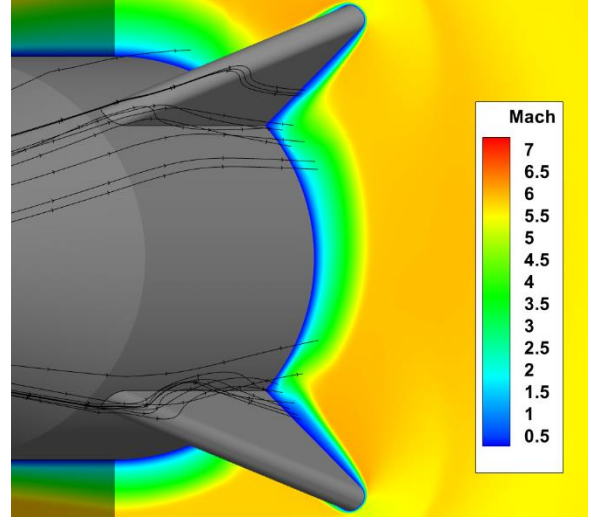


(b) Surface values at slices on Fin 1a (upper) and Fin 2a (lower).

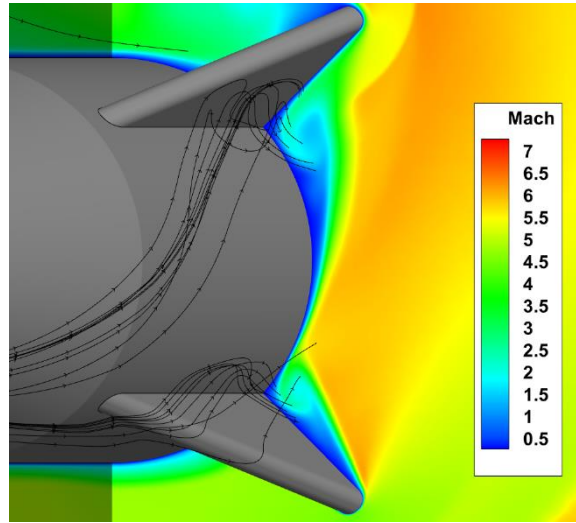
Figure 4.27: Skin friction coefficient magnitude along slices parallel to the symmetry boundary in conic missile +1 configuration (a) and slices on Fin 1a and Fin 2a (b).



(a) $AoA = 0^\circ$



(b) $AoA = 1^\circ$



(c) $AoA = 10^\circ$

Figure 4.28: Mach number contour with a slice at $x = 14.8 \text{ in}$ and velocity streamtraces on conic +1 missile-fin configuration.

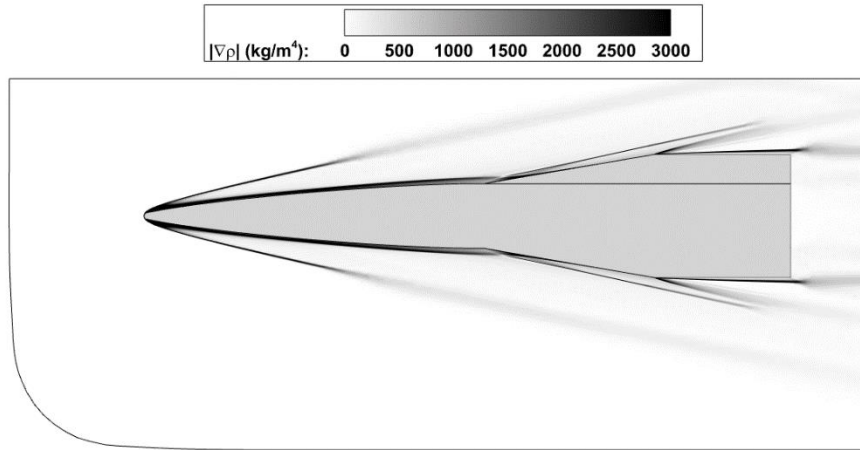
The ogive missile-fin configuration has the same basic flow structure of the conical missile configuration except for the expansion fan at the end of the nose as seen in the density gradient contours in Figure 4.29. The uninterrupted flow creates a strong shock in front of the fins seen in Figure 4.29 (a) and (b). Mach waves are visible in Figure 4.29 (c) between the lower boundary of the bow shock and the missile surface. The Mach and temperature contours in Figure 4.30 show

the respective flow conditions matching the general trend set in the conic missile results and flow structures in Figure 4.29

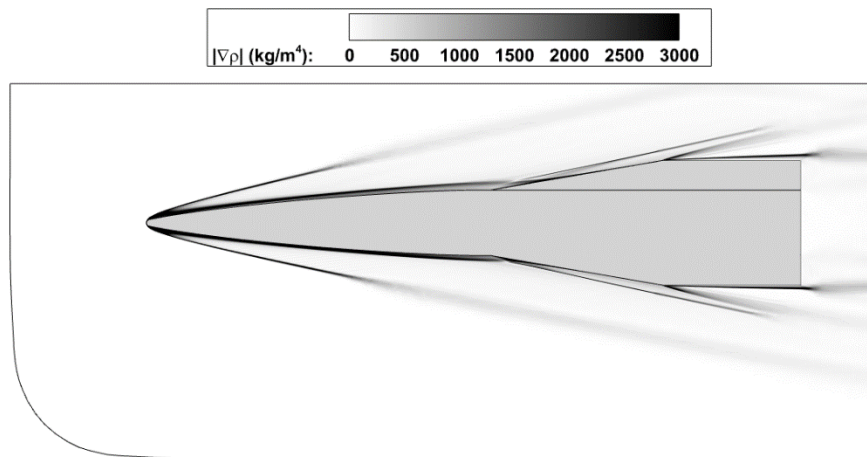
The flow development around the fins is shown in the Mach and density gradient contours in Figure 4.31 and Figure 4.32. The flow around the fins does not appear to change significantly from the conical configuration (excluding the expansion fan at the end of the conical nose). Changes in the boundary-layer thickness and areas of separation are seen in the same general locations as in the conical nose case.

The surface pressure, temperature, and skin friction coefficient are plotted in Figure 4.33, Figure 4.34, and Figure 4.35 respectively. The plots in (a) show the respective parameters on the missile surface on a slice taken at $z = 0.003937$ inches, and plots in (b) display the surface values on a slice rotated 45° clockwise and counterclockwise from the symmetry boundary. The pressure, temperature, and C_f on the ogive missile reach the approximately the same value as the conical missile just before the shock on the fin but take a different path to reach this point. The absence of the expansion fan upstream of the shock generated by the missile fin does not appear to have an effect on the surface values observed.

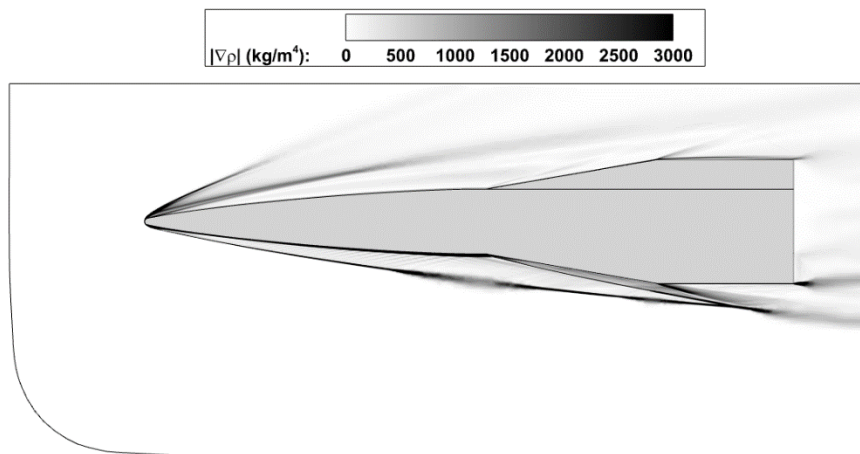
The complex three-dimensionality of the flow path is captured with velocity streamtraces in Figure 4.36. Some of the streamtraces flow downstream in a spiral pattern, indicating the existence of vorticity. The number of streamtraces forming spirals increases with the angle of attack. Some of the streamtraces plotted in Figure 4.36 (c) flow in an erratic manner due to the separation of the flow or flow impingement on the nose. The change in geometry does not appear to affect the complexity of the flow around the fins.



(a) $AoA = 0^\circ$

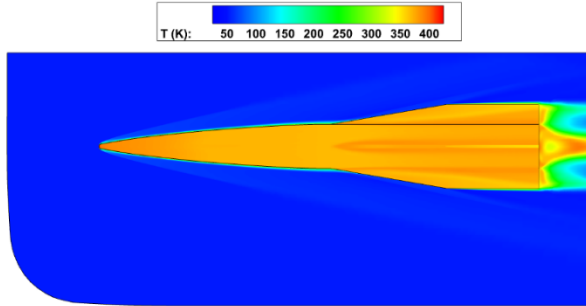


(b) $AoA = 1^\circ$

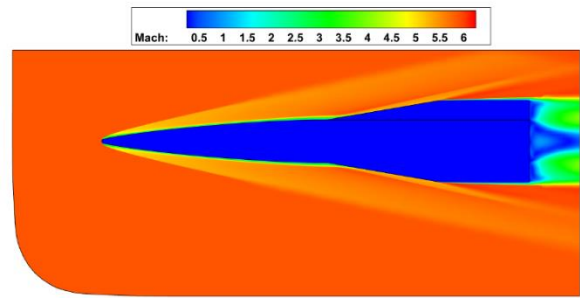


(c) $AoA = 10^\circ$

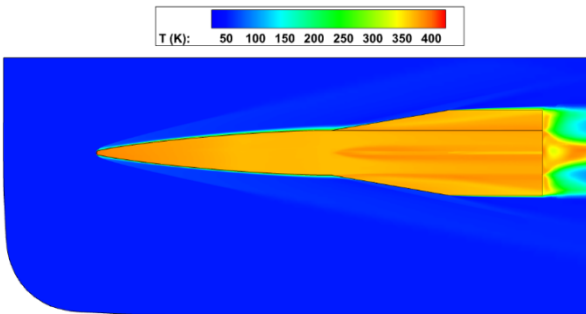
Figure 4.29: Density gradient magnitude contours of ogive missile configuration at various angles of attack.



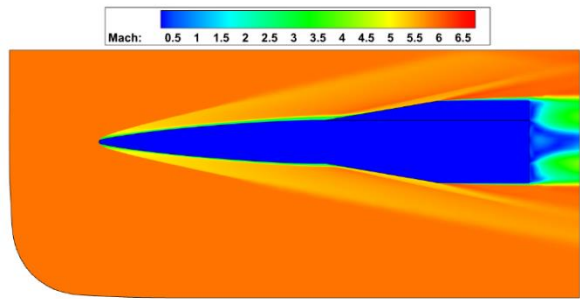
(a) $AoA = 0^\circ$



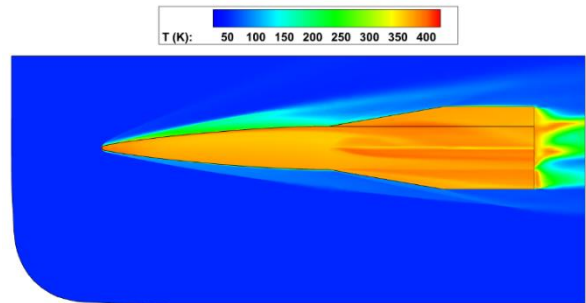
(d) $AoA = 0^\circ$



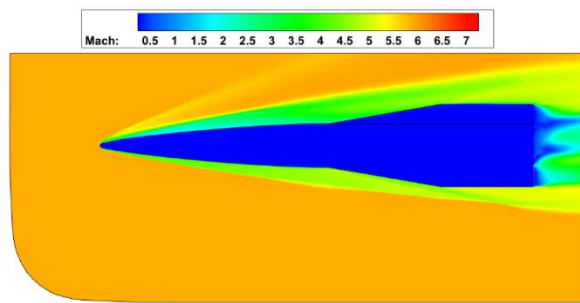
(b) $AoA = 1^\circ$



(e) $AoA = 1^\circ$

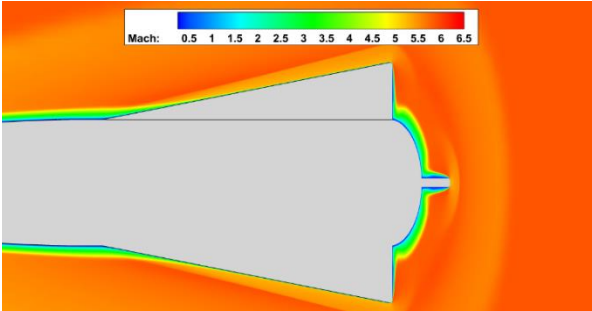


(c) $AoA = 10^\circ$

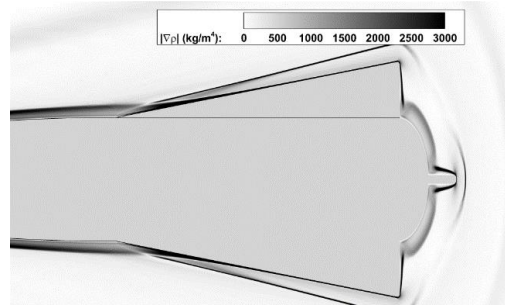


(f) $AoA = 10^\circ$

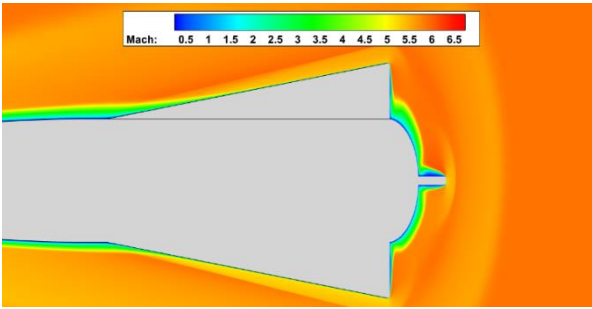
Figure 4.30: Contours of the ogive missile of Temperature (a)-(c) and Mach number (d)-(f) at various angles of attack.



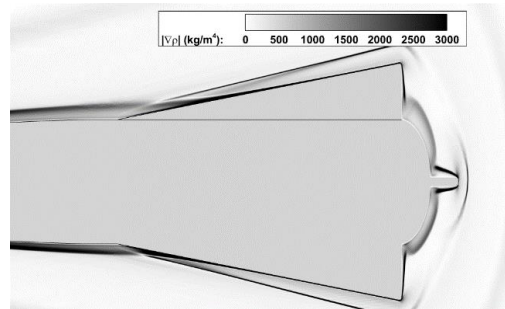
(a) $AoA = 0^\circ$



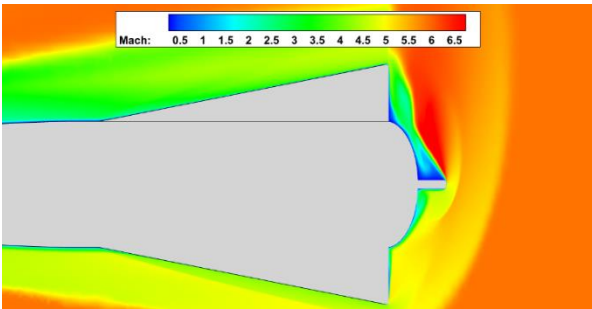
(d) $AoA = 0^\circ$



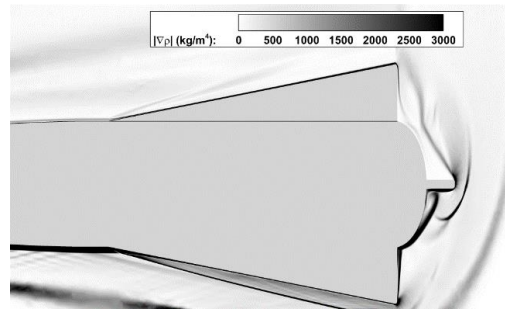
(b) $AoA = 1^\circ$



(e) $AoA = 1^\circ$

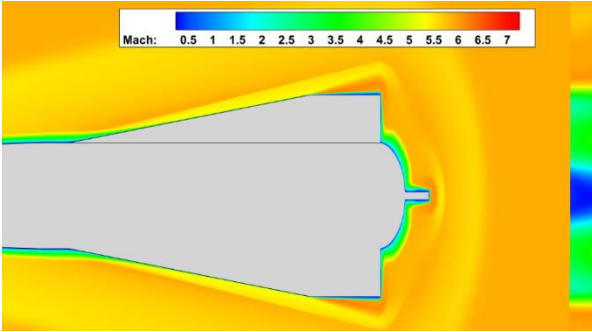


(c) $AoA = 10^\circ$

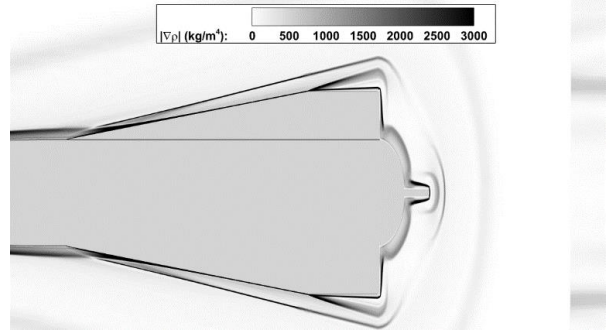


(f) $AoA = 10^\circ$

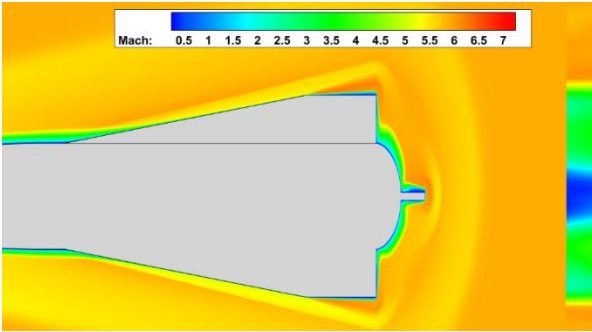
Figure 4.31: Contours of the ogive missile of Mach number (a)-(c) and density gradient magnitude (d)-(f) at various angles of attack with a slice at $x = 15.79$ in.



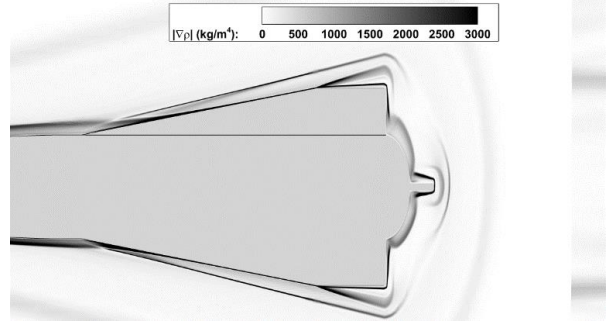
(a) $AoA = 0^\circ$



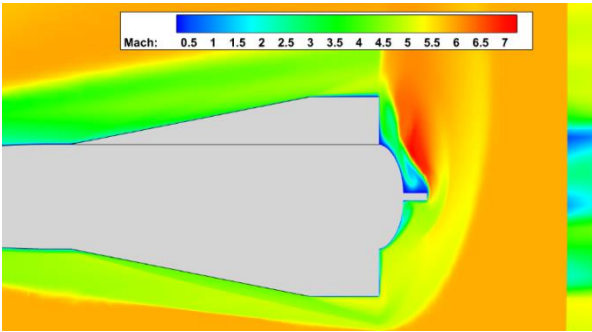
(d) $AoA = 0^\circ$



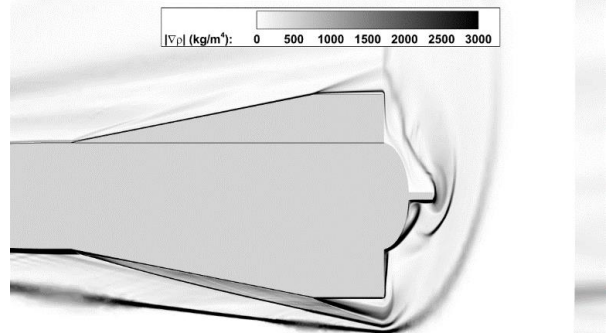
(b) $AoA = 1^\circ$



(e) $AoA = 1^\circ$

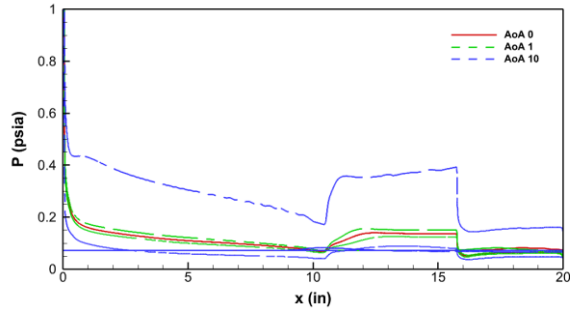


(c) $AoA = 10^\circ$

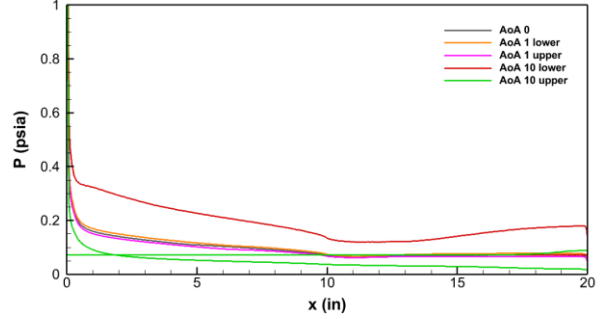


(f) $AoA = 10^\circ$

Figure 4.32: Contours of the ogive missile of Mach number (a)-(c) and density gradient magnitude (d)-(f) at various angles of attack with a slice at $x = 17.26 \text{ in.}$

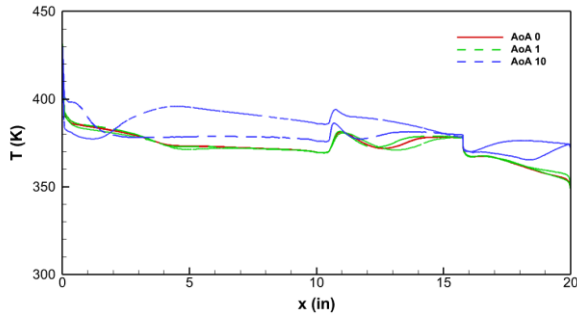


(a) Surface values at $z = 0.003937$ in.

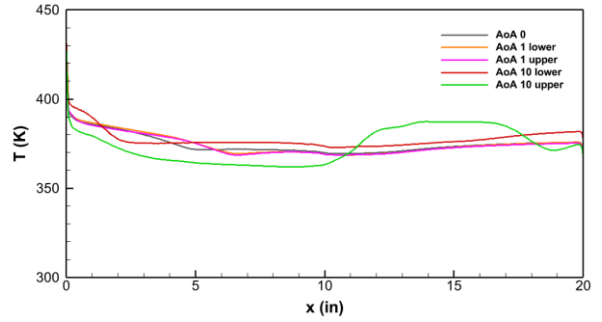


(b) Surface values at slices 45° between Fin 1 and Fin 2 (upper) and 45° between Fin 2 and Fin 3 (lower).

Figure 4.33: Pressure distribution along slices parallel to the symmetry boundary (a) and 45° between fins (b) in ogive missile configuration.

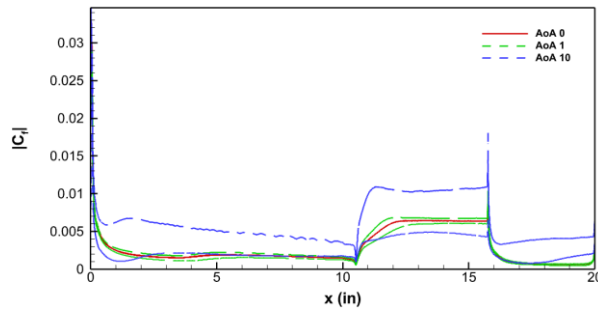


(a) Surface values at $z = 0.003937$ in.

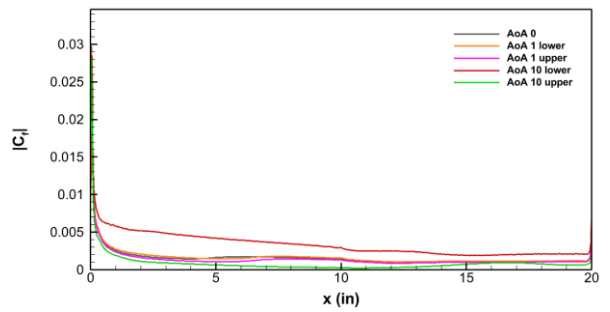


(b) Surface values at slices 45° between Fin 1 and Fin 2 (upper) and 45° between Fin 2 and Fin 3 (lower).

Figure 4.34: Temperature distribution along slices parallel to the symmetry boundary (a) and 45° between fins (b) in ogive missile configuration.

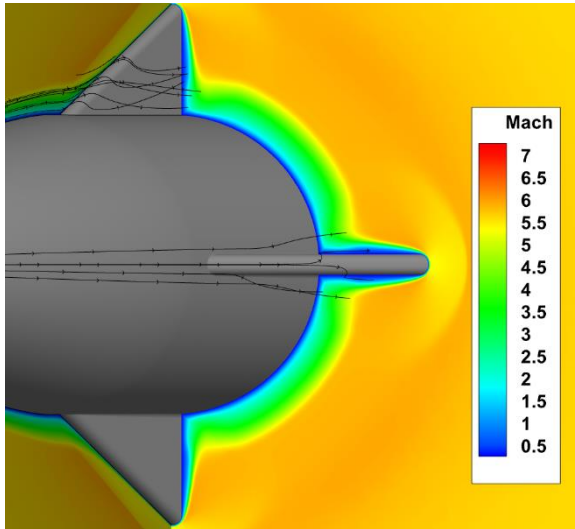


(a) Surface values at $z = 0.003937$ in.

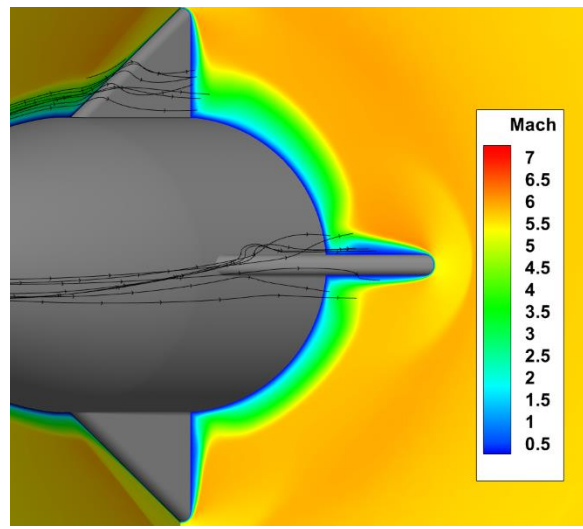


(b) Surface values at slices 45° between Fin 1 and Fin 2 (upper) and 45° between Fin 2 and Fin 3 (lower).

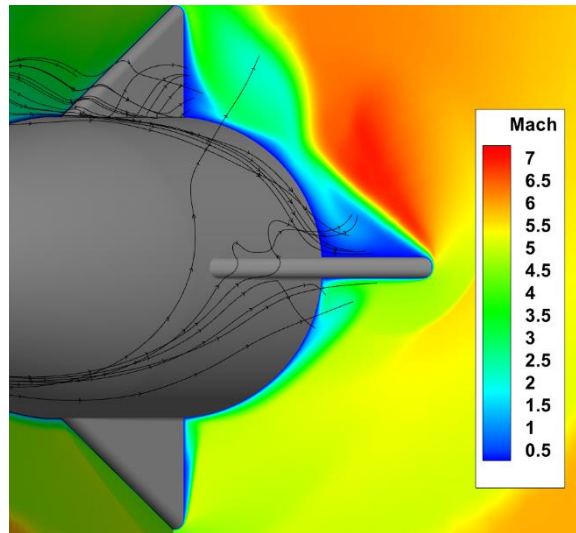
Figure 4.35: Skin friction coefficient magnitude along slices parallel to the symmetry boundary (a) and 45° between fins (b) in ogive missile configuration



(a) $AoA = 0^\circ$



(b) $AoA = 1^\circ$



(c) $AoA = 10^\circ$

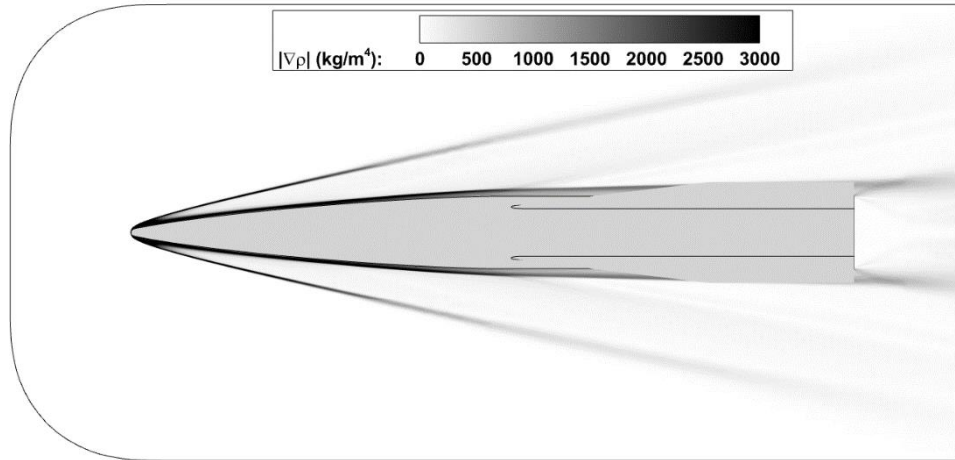
Figure 4.36: Mach number contour with a slice at $x = 14.8$ in and velocity streamtraces on ogive missile-fin configuration.

The flow structure of the ogive +1 missile-fin configuration is visualized in the density gradient, Mach number, and temperature contours in Figure 4.37 and Figure 4.38. The 0° AoA (a) and 1° AoA (b) cases show a bow shock in front of the missile and the outline of the shock wave formed on the fins on the symmetry plane. The 10° AoA (c) case shows an additional oblique shock on the upper surface of the missile. An expansion fan also appears to form on the lower surface upstream of Fin 2a.

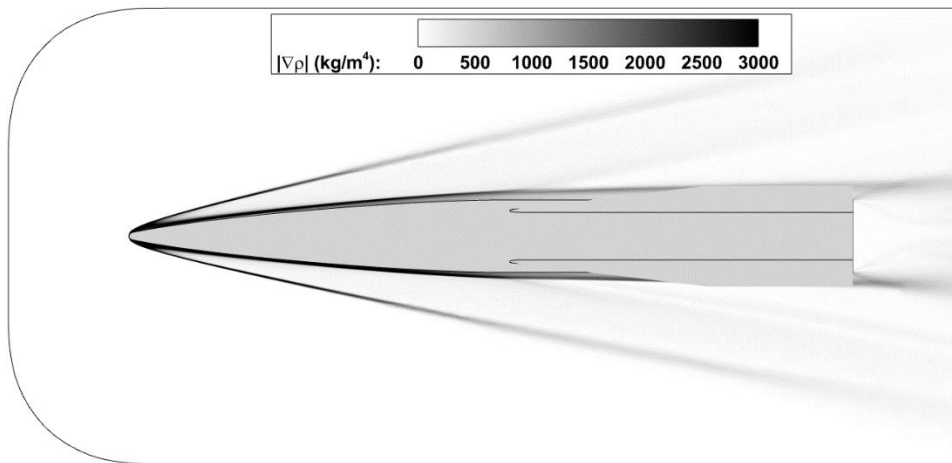
The flow physics between the missile fins is visualized in the Mach and density gradient contours in Figure 4.39 and the flows downstream development in Figure 4.40. The same physics in these contours is seen between the missile fins in the results of the conic +1 configuration.

Surface values of the pressure, temperature, and skin friction coefficient are plotted in Figure 4.41, Figure 4.42, and Figure 4.43 respectively. The surface values were extracted from slices taken in the same locations as the conic +1 configuration. The same trend between the base conic configuration and conic +1 configuration is evident in the comparison of the base ogive and ogive +1 configurations. A slight variation in the trend is seen in Figure 4.42 (b) at a 10° AoA where the temperature suddenly dips on the leading edge of Fin 1a.

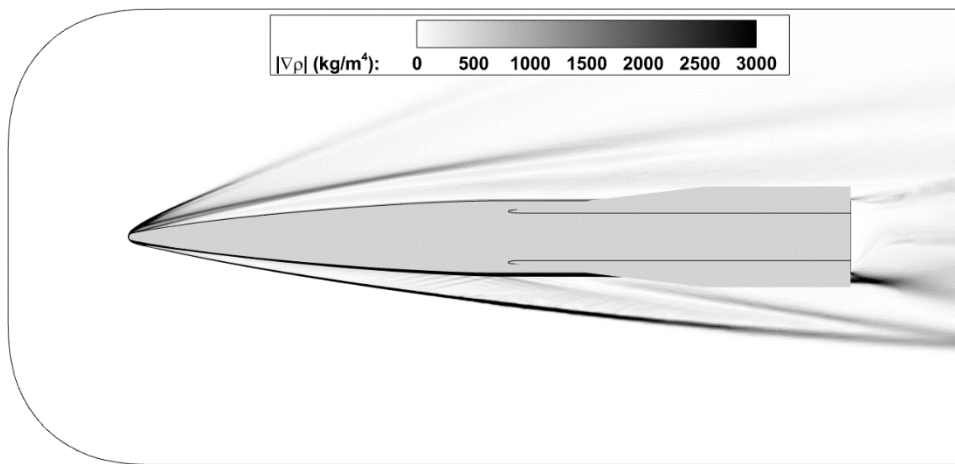
Velocity streamtraces on a Mach contour plot the flow path on the ogive +1 missile at each angle of attack in Figure 4.44 (a)-(c). Flow circulates from the surface of the body at the base of the fin towards the fin tip on the sidewall of Fin 2a as seen in Figure 4.44 (a) which may be a location of boundary-layer separation. The amount of circulating flow increases with angle attack. Figure 4.44 (c) shows a spiraling flow path as a result of the separated flow.



(a) $AoA = 0^\circ$

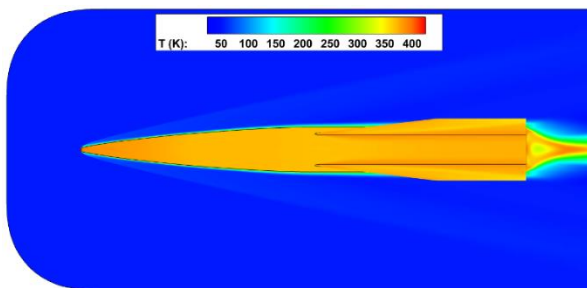


(b) $AoA = 1^\circ$

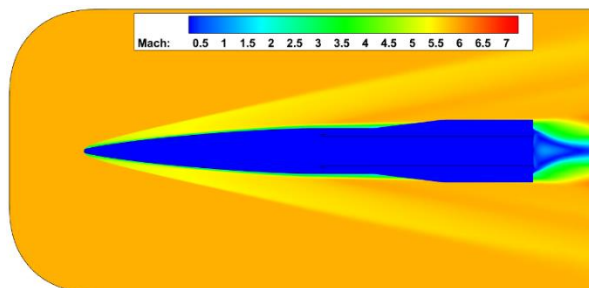


(c) $AoA = 10^\circ$

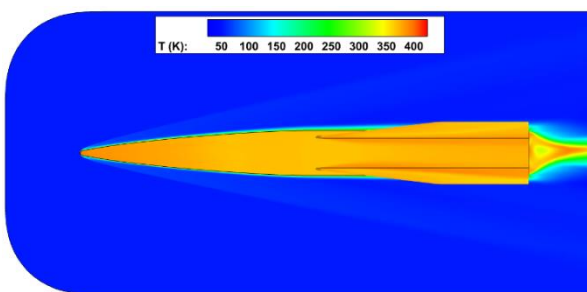
Figure 4.37: Density gradient magnitude contours of ogive +1 missile configuration at various angles of attack.



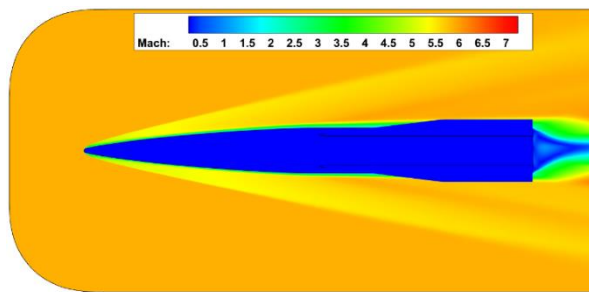
(a) $AoA = 0^\circ$



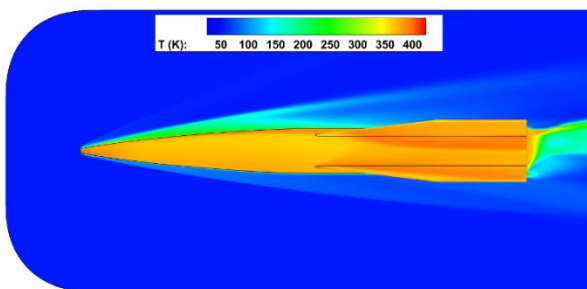
(d) $AoA = 0^\circ$



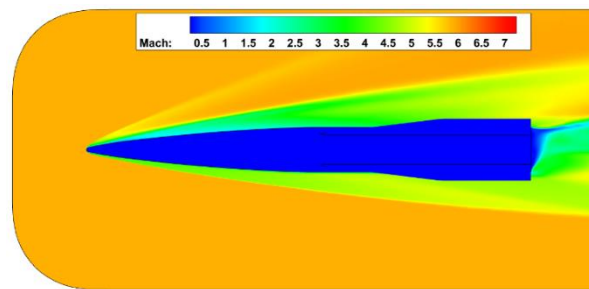
(b) $AoA = 1^\circ$



(e) $AoA = 1^\circ$

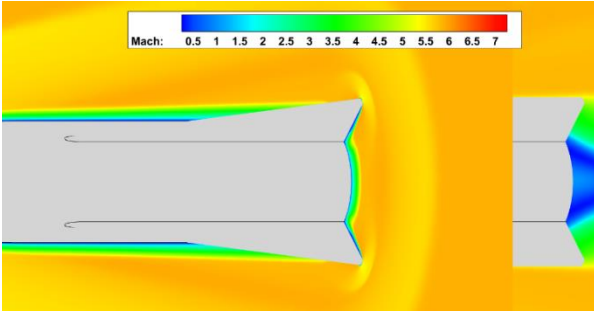


(c) $AoA = 10^\circ$

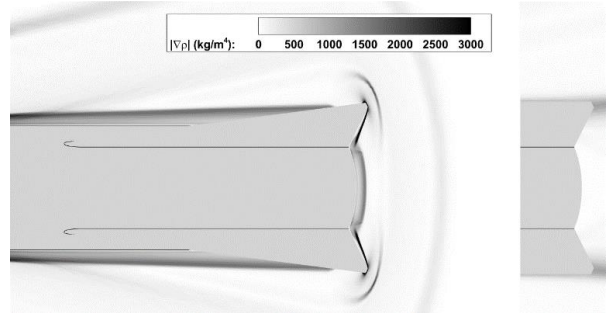


(f) $AoA = 10^\circ$

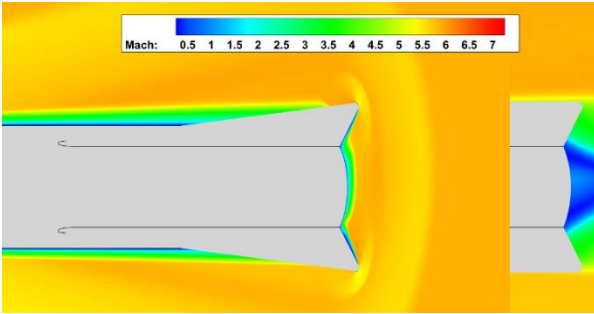
Figure 4.38: Contours of the ogive +1 missile of Temperature (a)-(c) and Mach number (d)-(f) at various angles of attack.



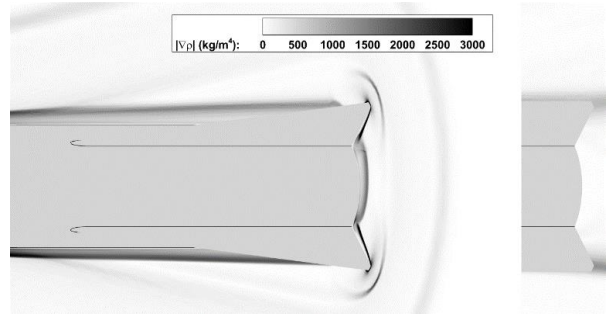
(a) $AoA = 0^\circ$



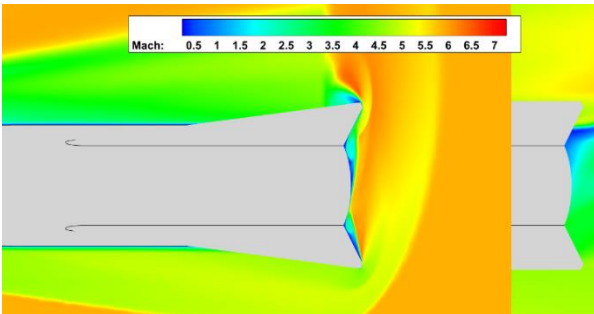
(d) $AoA = 0^\circ$



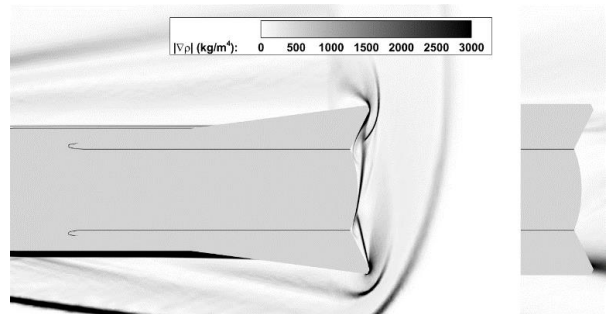
(b) $AoA = 1^\circ$



(e) $AoA = 1^\circ$

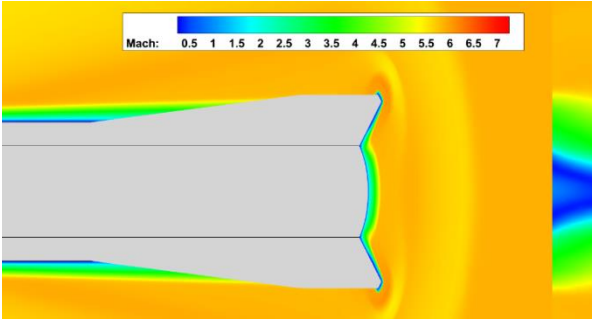


(c) $AoA = 10^\circ$

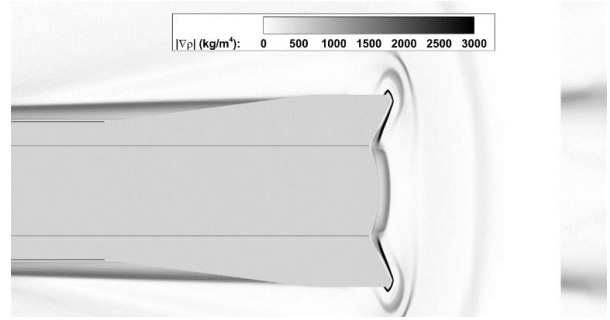


(f) $AoA = 10^\circ$

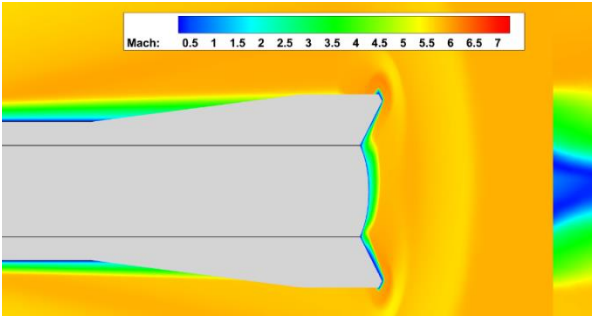
Figure 4.39: Contours of the ogive +1 missile of Mach number (a)-(c) and density gradient magnitude (d)-(f) at various angles of attack with a slice at $x = 15.79$ in.



(a) $AoA = 0^\circ$



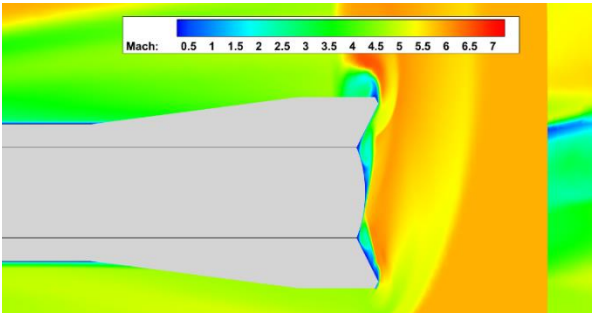
(d) $AoA = 0^\circ$



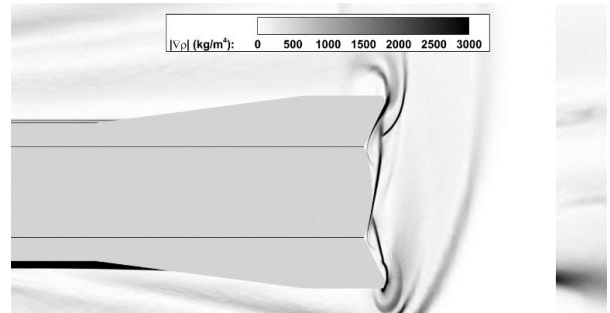
(b) $AoA = 1^\circ$



(e) $AoA = 1^\circ$

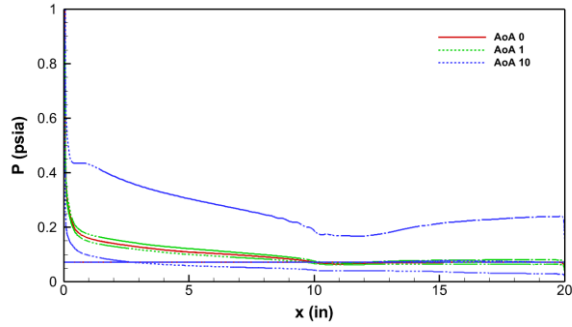


(c) $AoA = 10^\circ$

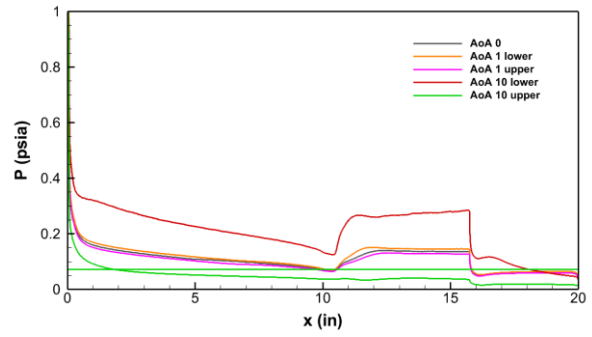


(f) $AoA = 10^\circ$

Figure 4.40: Contours of the ogive +1 missile of Mach number (a)-(c) and density gradient magnitude (d)-(f) at various angles of attack with a slice at $x = 17.26 \text{ in.}$

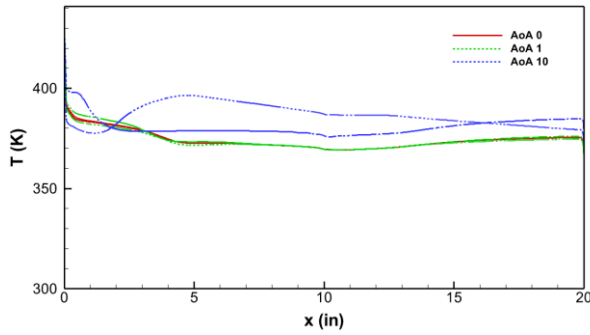


(a) Surface values at $z = 0.003937$ in.

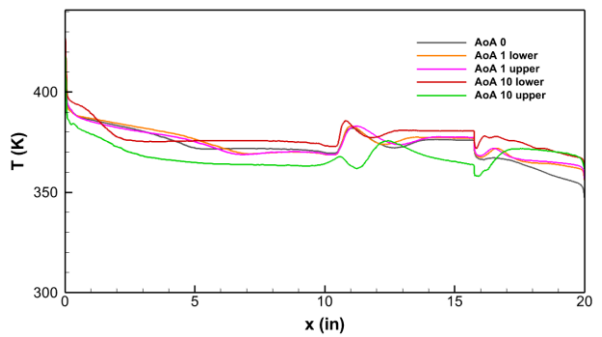


(b) Surface values at slices 45° rotated from symmetry to measuring values on Fin 1a (upper) and Fin 2a (lower).

Figure 4.41: Pressure distribution along slices parallel to the symmetry boundary (a) and 45° clockwise and counterclockwise from symmetry boundary (b) in ogive +1 missile configuration.

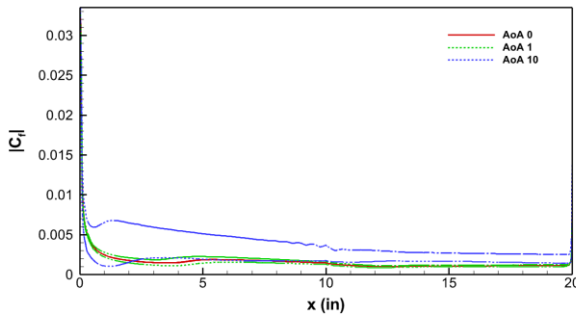


(a) Surface values at $z = 0.003937$ in.

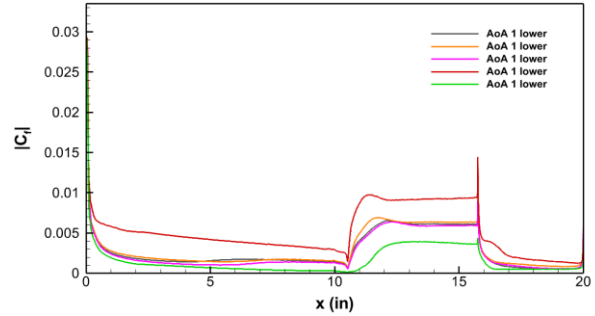


(b) Surface values at slices 45° rotated from symmetry to measuring values on Fin 1a (upper) and Fin 2a (lower).

Figure 4.42: Temperature distribution along slices parallel to the symmetry boundary (a) and 45° clockwise and counterclockwise from symmetry boundary (b) in ogive +1 missile configuration.



(a) Surface values at $z = 0.003937$ in.



(b) Surface values at slices 45° rotated from symmetry to measuring values on Fin 1a (upper) and Fin 2a (lower).

Figure 4.43: Skin friction coefficient magnitude along slices parallel to the symmetry boundary (a) and 45° clockwise and counterclockwise from symmetry boundary (b) in ogive +1 missile configuration.

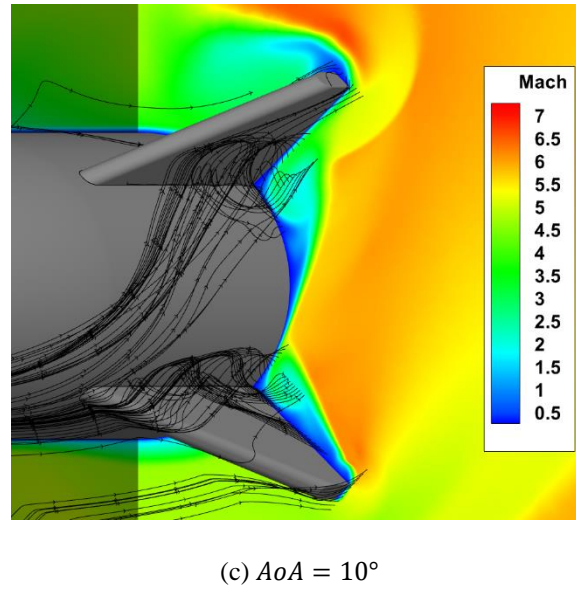
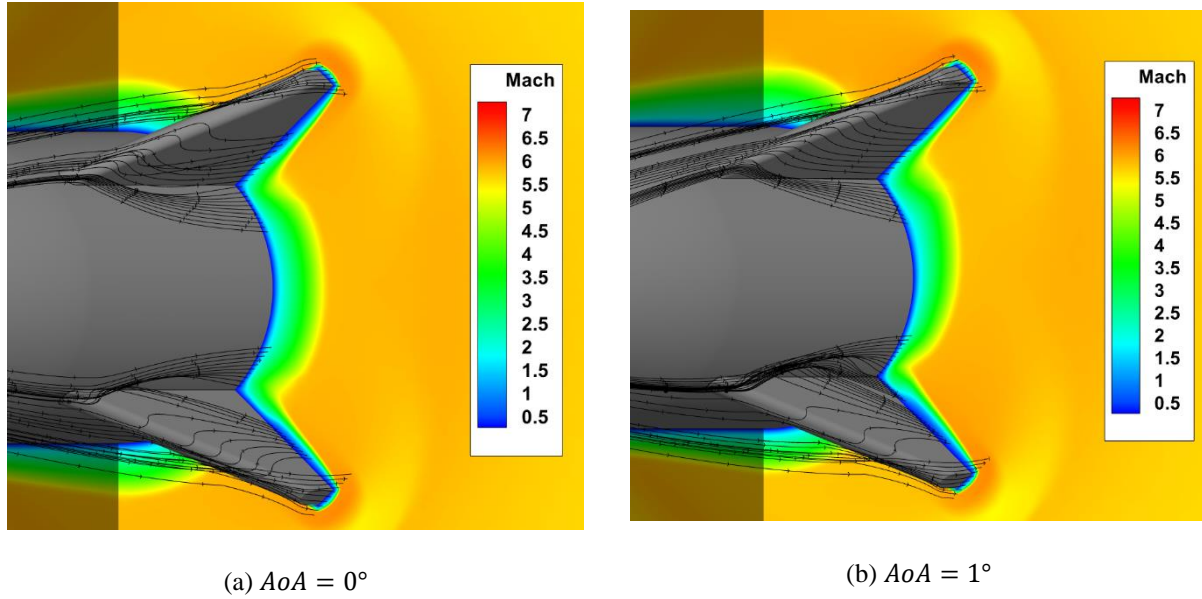


Figure 4.44: Mach number contour and velocity streamtraces on ogive +1 missile-fin configuration.

The shock waves upstream of the missile fins cause a rise in temperature, pressure, and skin friction which impacts the flow near the missile surface. A separation bubble was not found in-between the shock and missile fins as a result of the SBLI; it is assumed that the Reynolds

number of the incoming flow was too high, and that the sweep angle of the fin was too low to cause a sufficiently strong adverse pressure gradient to initiate separation. The shock waves and geometry differences do not appear to have a significant impact on the complexity of the flow around the fins. A small amount of complex flow is visible at 0° AoA and increases with AoA. The 10° AoA showed early flow separation that impacted the flow downstream.

Certain features of the missile-fin flowfield depend strongly on the grid resolution and quality. For example, Figure 4.45 shows a sample of the Mach number contour on the conic missile-fin configuration at 0° angle of attack. The edge of the entropy layer is seen to be well resolved in the portion of the mesh that consists of prisms. The edge of the entropy layer is diffusion, and not captured as clearly in the fully unstructured region in the center of the image. Once the prism layer is large enough to capture the entropy layer again, an edge is clearly seen. These results indicate the need for a future, more detailed study of the effect of mesh quality and resolution on the quantities of engineering interest, such as mean surface temperature.

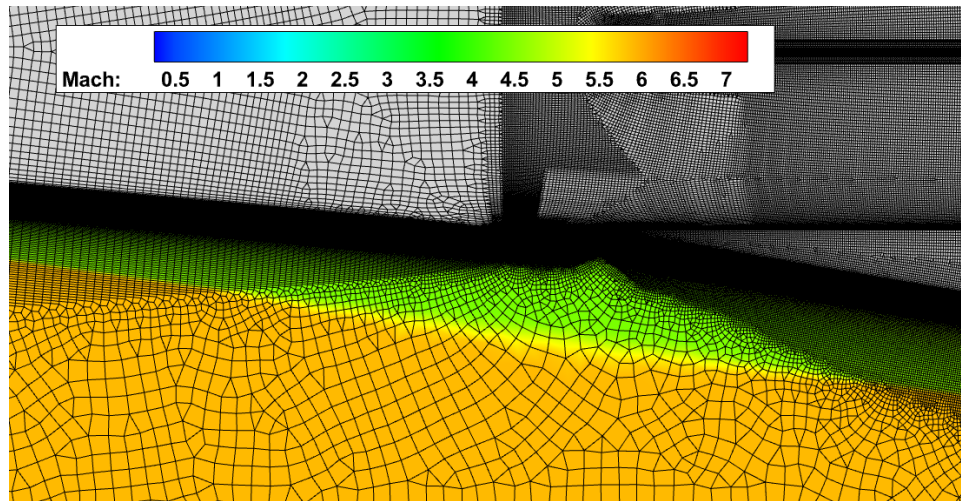


Figure 4.45: Sample of solution dependency on mesh from Mach number contour.

4.3 Conclusions

Two missile geometries were selected to analyze the mean flow and resulting SBLI around a missile-fin configuration. For each missile geometry, six simulations were carried out: two variations with a 90° roll, referred to with a “+1”, and three variations on the angle of attack: 0° ,

1°, and 10°. Four unstructured grids were produced which contained many prism layers with an initial wall spacing of $9\ \mu m$. The flow simulations showed the averaged flow over the different configurations. The SBLI caused an increase in temperature on the missile surface. Flow remained attached upstream of the fin and downstream of the shock because of the high Reynolds number of the flow and low sweep angle of the fin. The complex flow three-dimensionality was visualized using velocity streamtraces. The degree of flow complexity around the fins increased with angle of attack and did not appear to be significantly affected by the different geometry configurations.

A future simulation of both missile-fin configurations is needed to confirm a mesh independent solution. It is also recommended to produce a higher quality mesh to resolve flow discontinuities outside of the prism layer. Furthermore, the mesh produced by the *Trex* tool in Pointwise® was not fully refined in some areas. The anisotropic cell creation (used to generate the prism layers) halted early in regions where the geometry abruptly changed. It is recommended to improve the surface mesh as to reduce the maximum area ratio to 1.2, and extrude the surface mesh to create a layer of hexahedral and triangular prism cells. The new mesh generated should be large enough to resolve the boundary-layer which will allow for a structured block to envelope the near-body mesh. The structured block can be used to focus and align grid points for improved simulation results.

5. SUMMARY

An investigation into the preliminary design of a high enthalpy hypersonic wind tunnel driven by N_2O oxidation was performed. Key performance factors were identified. A combustion facility often produces water droplets in the test region when using clean air. These droplets can affect the flow characteristics around the test article or reduce the Mach number. A mixture of N_2O and N_2 was selected to remove the possibility of water condensation with the presence of hydrogen. The next problem addressed was how to achieve the combustion necessary for the high enthalpy flow. A catalyst is to be selected to lower the energy required to obtain nitrous oxide decomposition.

Flow uniformity is a necessity in any wind tunnel. A nozzle contour was created using Sivells' CONTUR program at Mach 6.13. The contour was modeled in CFD using SU2 to validate the program and identify possible issues. The simulation results confirmed the programs ability to accurately design a nozzle at given Mach number. A test region with a test article was additionally modeled to examine flow quality for testing. The simulation showed adequate flow quality over the test article. An additional nozzle contour was created with CONTUR and modeled in CFD using Kestrel to further validate CONTUR and CFD simulations. Results of a Mach 3.64 nozzle simulation matched reasonably well with experimental results when comparing the outlet pressure on the nozzle wall upstream of the nozzle exit.

Though initial results have been promising, further investigation is required before a complete design can be accomplished. Thermochemical reaction mechanisms and catalysis must be understood and implemented into the nozzle design and CFD simulations before a final design can be considered. The simulations presented showed good results, but future simulations need to include the upstream thermochemical reactions.

Hypersonic test facilities aid the future research and design of high-speed vehicles. Shock / boundary-layer interactions and complex 3D flow structures were examined in RANS computations of two generic high-speed missile geometries. These geometries were simulated at a 0° and 45° roll and 0° , 1° , and 10° angle of attack, yielding six different simulations. The study focused on the flow physics on the missiles' fins. The shock / boundary-layer interactions caused an increase in surface temperature, pressure and skin friction. The increase in surface pressure was not sufficient to cause separation in the boundary-layer. The complexity of the flow and the

presence of streamwise vortices were captured by velocity streamtraces. The degree of flow complexity increased with angle of attack.

REFERENCES

- [1] H.-S. Tsien, "Similarity laws of hypersonic flows," *Journal of Mathematics and Physics*, vol. 25, no. 1-4, pp. 247-251, 1946.
- [2] G. L. Hammock, "Expansion of the AEDC H2 arc heater facility test envelope using cold-air mixing," in *33rd AIAA Aerodynamic Measurement Technology and Ground Testing Conference*, 2017.
- [3] L. Trimmer, J. Cary and R. Voisin, "The optimum hypersonic wind tunnel," in *14th Aerodynamic Testing Conference*, 1968.
- [4] F. K. Lu, *Advanced hypersonic test facilities*, vol. 198, AIAA, 2002.
- [5] P. O. Krehl, *History of shock waves, explosions and impact: a chronological and biographical reference*, Springer Science & Business Media, 2008, 2008.
- [6] J. D. Anderson Jr., *Modern Compressible Flow with a historical perspective*, New York: McGraw-Hill, 2003.
- [7] L. L. Cronvich, "Numerical-graphical methods of characteristics for plane potential shock-free flow problems," *Journal of the Aeronautical Sciences*, vol. 14, no. 4, pp. 237-242, 1947.
- [8] J. C. Sivells, "A computer program for the aerodynamic design of axisymmetric and planar nozzles for supersonic and hypersonic wind tunnels," *Arnold AFB TN*, 1978.
- [9] R. Li, J. Shen and J. Gong, "Development of Aerodynamic Design of Hypersonic Quiet Nozzles," *Procedia Engineering*, vol. 99, pp. 1625-1629, 2015.
- [10] T. J. Juliano, S. P. Schneider, S. Aradag and D. Knight, "Quiet-flow Ludwig tube for hypersonic transition research," *AIAA journal*, vol. 46, no. 7, pp. 1757-1763, 2008.
- [11] Z. Jiang, Z. Hu, Y. Wang and G. Han, "Advances in critical technologies for hypersonic and high-enthalpy wind tunnel," *Chinese Journal of Aeronautics*, vol. 33, no. 12, pp. 3027-3038, 2020.
- [12] J. D. Coles, "The turbulent boundary layer in a compressible fluid," 1962.
- [13] D. S. Dolling, "Fifty years of shock-wave/boundary-layer interaction research: what next?," *AIAA journal*, vol. 39, no. 8, pp. 1517-1531, 2001.

- [14] D. Dolling and S. Bogdonoff, "Blunt fin-induced shock wave/turbulent boundary-layer interaction," *AIAA Journal*, vol. 20, no. 12, pp. 1674-1680, 1982.
- [15] C.-M. Hung and P. G. Buning, "Simulation of blunt-fin-induced shock wave and turbulent boundary-layer interaction," *Journal of Fluid Mechanics*, vol. 154, pp. 163-185, 1985.
- [16] J. Poggie and K. M. Porter, "Flow structure and unsteadiness in a highly confined shock-wave--boundary-layer interaction," *Physical Review Fluids*, vol. 4, no. 2, p. 024602, 2019.
- [17] C. S. Combs, P. A. Kreth, J. D. Schmisser and E. L. Lash, "Image-based analysis of shock-wave/boundary-layer interaction unsteadiness," *AIAA Journal*, vol. 56, no. 3, pp. 1288-1293, 2018.
- [18] N. T. Clemens and V. Narayanaswamy, "Low-frequency unsteadiness of shock wave/turbulent boundary layer interactions," *Annual Review of Fluid Mechanics*, vol. 46, pp. 469-492, 2014.
- [19] D. Dolling, C. Cosad and B. S.M., "An examination of blunt fin-induced shock wave turbulent boundary layer interactions," in *17th Aerospace Sciences Meeting*, New Orleans, 1979.
- [20] G. S. Settles, T. J. Fitzpatrick and S. M. Bogdonoff, "Detailed Study of Attached and Separated Compression Corner Flowfields in High Reynolds Number Supersonic Flow," *AIAA Journal*, vol. 17, no. 6, pp. 579-585, 1979.
- [21] G. S. Settles, S. M. Bogdonoff and I. E. Vas, "Incipient separation of a supersonic turbulent boundary layer at high Reynolds numbers," *AIAA Journal*, vol. 14, no. 1, pp. 50-56, 1976.
- [22] J. Green, "Interactions between shock waves and turbulent boundary layers," *Progress in Aerospace Sciences*, vol. 11, pp. 235-340, 1970.
- [23] M. Lugin, S. Beneddine, C. Leclercq, E. Garnier and R. Bur, "Transition scenario in hypersonic axisymmetrical compression ramp flow," *Journal of Fluid Mechanics*, vol. 907, 2021.
- [24] B. Hodge and K. Koenig, *Compressible Fluid Dynamics with Personal Computer Applications*, Prentice Hall Englewood Cliffs, 1995.
- [25] I. Beckwith, H. W. Ridyard and N. Cromer, "The aerodynamic design of high Mach number nozzles utilizing axisymmetric flow with application to a nozzle of square test section," 1952.

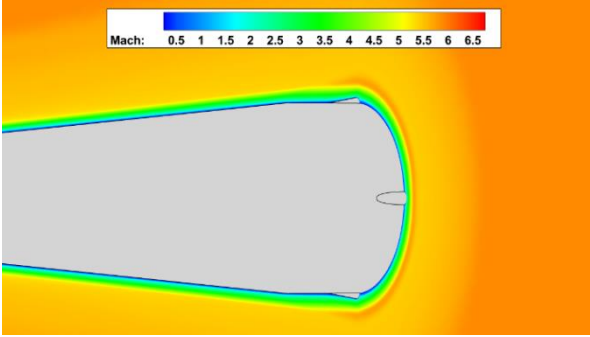
- [26] W. S. Saric, "Görtler Vortices," *Annual Review of Fluid Mechanics*, vol. 26, no. 1, pp. 379-409, 1994.
- [27] H. W. Liepmann and A. Roshko, *Elements of Gasdynamics*, Courier Corporation, 2001.
- [28] S. D. Heister, W. E. Anderson, T. L. Pourpoint and R. J. Cassady, *Rocket Propulsion*, Cambridge University Press, 2019.
- [29] L. Zavalan and A. Rona, "contur," 2019.
- [30] K. Foelsch, "The analytical design of an axially symmetric laval nozzle for a parallel and unimform jet," *Journal of the Aeronautical Sciences*, vol. 16, no. 3, pp. 161-166, 1949.
- [31] S. E. Adams, *The design and computational validation of a Mach 3 wind tunnel nozzle contour*, University of Tennessee, 2016.
- [32] F. Shope, "Contour design techniques for super/hypersonic wind tunnel nozzles," in *24th AIAA Applied Aerodynamics Conference*, 2006, p. 3665.
- [33] I. Hall, "Transonic flow in two-dimensional and axially-symmetric nozzles," *The Quarterly Journal of Mechanics and Applied Mathematics*, vol. 15, no. 4, pp. 487-508, 1962.
- [34] J. Kliegel and J. Levine, "Transonic flow in small throat radius of curvature nozzles.," *AIAA Journal*, vol. 7, no. 7, pp. 1375-1378, 1969.
- [35] R. J. Mary Jr, H. D. Thompson and J. D. Hoffman, "Comparison of transonic flow solutions in CD nozzles," *puwl*, 1974.
- [36] Y.-N. Yu, "A summary of design techniques for axisymmetric hypersonic wind tunnels," 1958.
- [37] J. C. Sivells, "Aerodynamic design of axisymmetric hypersonic wind-tunnel nozzles," *Journal of Spacecraft and Rockets*, vol. 7, no. 11, pp. 1292-1299, 1970.
- [38] D. Spalding and S. Chi, "The drag of a compressible turbulent boundary layer on a smooth flat plate with and without heat transfer," *Journal of Fluid Mechanics*, vol. 18, no. 1, pp. 117-143, 1964.
- [39] F. M. White, *Viscous Fluid Flow*, 3rd ed., New York: McGraw-Hill, 2006, pp. 485-487.
- [40] A. Clément, "Coupling of two absorbing boundary conditions for 2D time-domain simulations of free surface gravity waves," *Journal of Computational Physics*, vol. 126, no. 1, pp. 139-151, 1996.

- [41] P. D. Thomas and J. F. Middlecoff, "Direct Control of the Grid Point Distribution in Meshes," *AIAA Journal*, vol. 18, no. 6, pp. 652-656, 1980.
- [42] J. L. Steger and R. L. Sorenson, "Automatic mesh-point clustering near a boundary in grid generation with elliptic partial differential equations," *Journal of Computational Physics*, vol. 33, pp. 405-410, 1979.
- [43] Pointwise Inc., "User Manual," [Online]. Available: <https://www.pointwise.com/doc/user-manual/index.html>.
- [44] T. D. Economon, F. Palacios, S. R. Copeland, T. W. Lukaczyk and J. J. Alonso, "SU2: An open-source suite for multiphysics simulation and design," *AIAA Journal*, vol. 54, no. 3, pp. 828-846, 2016.
- [45] A. Spinelli, G. Cammi, S. Gallarini, M. Zocca, F. Cozzi, P. Gaetani, V. Dossena and A. Guardone, "Experimental evidence of non-ideal compressible effects in expanding flow of a high molecular complexity vapor," *Experiments in Fluids*, vol. 59, no. 8, p. 126, 2018.
- [46] S. Vitale, G. Gori, M. Pini, A. Guardone, T. D. Economon, F. Palacios, J. J. Alonso and P. Colonna, "Extension of the su2 open source cfd code to the simulation of turbulent flows of fluids modelled with complex thermophysical laws," in *22nd AIAA Computational Fluid Dynamics Conference*, 2015.
- [47] F. R. Menter, "Improved two-equation k-omega turbulence models for aerodynamic flows," 1992.
- [48] S. Rodriguez, *Applied Computational Fluid Dynamics and Turbulence Modeling*, Springer, 10`9.
- [49] J. D. Anderson Jr., *Computational Fluid Dynamics: The Basics with Applications*, New York: McGraw-Hill, Inc., 1995, pp. 497-499.
- [50] S. Yoon and A. Jameson, "Lower-upper symmetric-Gauss-Seidel method for the Euler and Navier-Stokes equations," *AIAA Journal*, vol. 26, no. 9, pp. 1025-1026, 1988.
- [51] M.-S. Liou and C. J. Steffen Jr., "A new flux splitting scheme," *Journal of Computational physics*, vol. 107, no. 1, pp. 23-39, 1993.

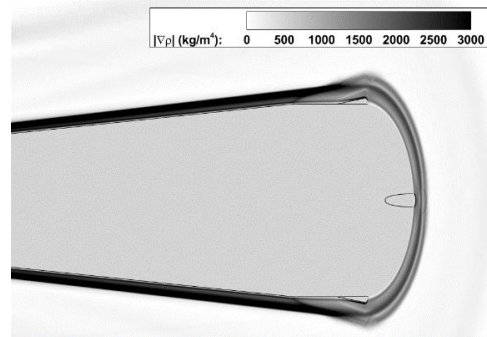
- [52] A. Syrakos, S. Varchanis, Y. Dimakopoulos, A. Goulas and J. Tsamopoulos, "On the order of accuracy of the divergence theorem (Green-Gauss) method for calculating the gradient in finite volume methods," 2017.
- [53] A. Soulaïmani, N. B. Salah and Y. Saad, "Acceleration of GMRES convergence for some CFD problems: Preconditioning and stabilization techniques," 2000.
- [54] R. H. Pletcher, J. C. Tannehill and D. Anderson, Computational fluid mechanics and heat transfer, CRC Press, 2012.
- [55] W. Sutherland, "The viscosity of gases and molecular force," *The London, Edinburgh, and Dublin Philosophical Magazine and Journal of Science*, vol. 36, no. 223, pp. 507-531, 1893.
- [56] HPCMP Create-AV, *HPCMP Create-AV Kestrel User's Guide*, 2020.
- [57] S. Hamdi, W. E. Schiesser and G. W. Griffiths, "Method of lines," *Scholarpedia*, vol. 2, no. 7, p. 2859, 2007.
- [58] F. R. Menter, P. E. Smirnov, T. Liu and R. Avancha, "A one-equation local correlation-based transition model," *Flow, Turbulence and Combustion*, vol. 95, no. 4, pp. 583-619, 2015.
- [59] P. Spalart and S. Allmaras, "A one-equation turbulence model for aerodynamic flows," in *30th Aerospace Sciences Meeting and Exhibit*, Reno, 1992.
- [60] T. Miyoshi and K. Kusano, "A multi-state HLL approximate Riemann solver for ideal magnetohydrodynamics," *Journal of Computational Physics*, vol. 208, no. 1, pp. 315-344, 2005.
- [61] C. Kong, "Comparison of Approximate Riemann Solvers," 2011.
- [62] A. Harten, P. D. Lax and B. v. Leer, "On upstream differencing and Godunov-type schemes for hyperbolic conservation laws," *SIAM review*, vol. 25, no. 1, pp. 35-61, 1983.
- [63] S. H. Park and J. H. Kwon, "On the dissipation mechanism of Godunov-type schemes," *Journal of Computational Physics*, vol. 188, no. 2, pp. 524-542, 2003.
- [64] V. Venkatakrishnan, "Convergence to steady state solutions of the Euler equations on unstructured grids with limiters," *Journal of computational physics*, vol. 118, no. 1, pp. 120-130, 1995.

- [65] N. P. C. Marques and J. C. F. Pereira, "Comparison of three second-order accurate reconstruction schemes for 2D Euler and Navier-Stokes compressible flows on unstructured grids," *Communications in numerical methods in engineering*, vol. 17, no. 5, pp. 309-323, 2001.
- [66] M. Röhrig, E. L. Petersen, D. F. Davidson and R. K. Hanson, "The pressure independence of the thermal decomposition of N₂O," *International Journal of Chemical Kinetics*, vol. 28, no. 8, pp. 599-608, 1996.
- [67] Ansys, Inc., *ANSYS Chemkin-Pro Theory Manual*, 2020.
- [68] P. Finley, "Static pressure in hypersonic nozzle boundary layers," *AIAA Journal*, vol. 15, no. 6, pp. 878-881, 1977.

APPENDIX A: RESULTS OF HYPERSONIC MISSILE-FIN CONFIGURATIONS



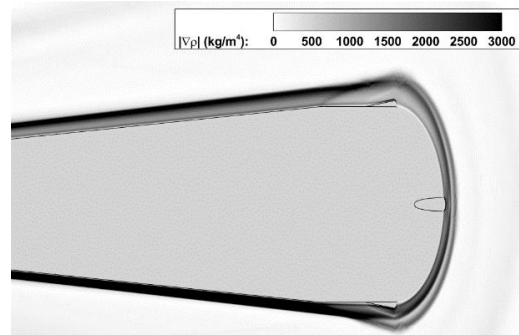
(a) $AoA = 0^\circ$



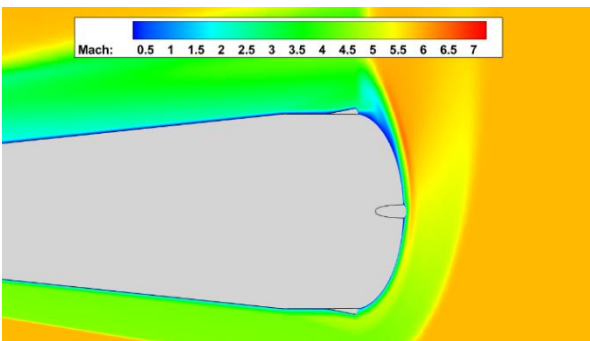
(d) $AoA = 0^\circ$



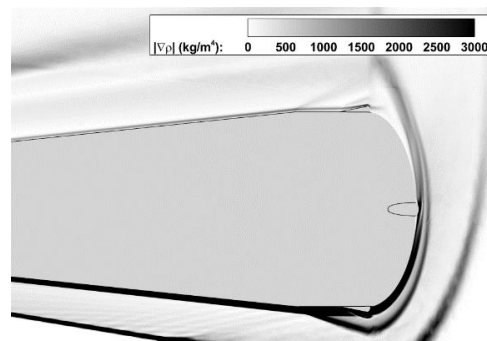
(b) $AoA = 1^\circ$



(e) $AoA = 1^\circ$

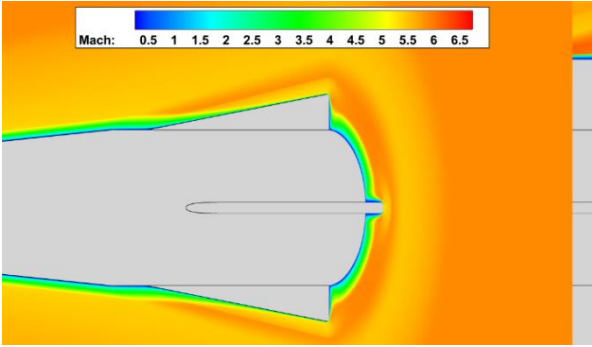


(c) $AoA = 10^\circ$

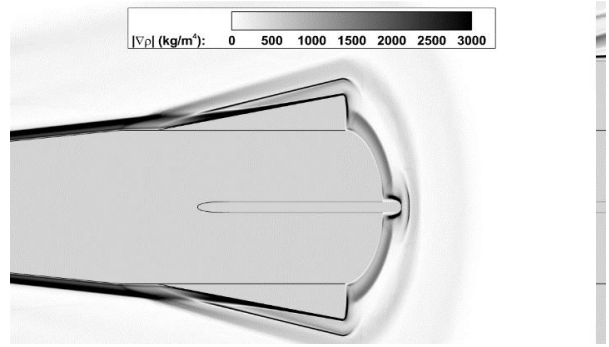


(f) $AoA = 10^\circ$

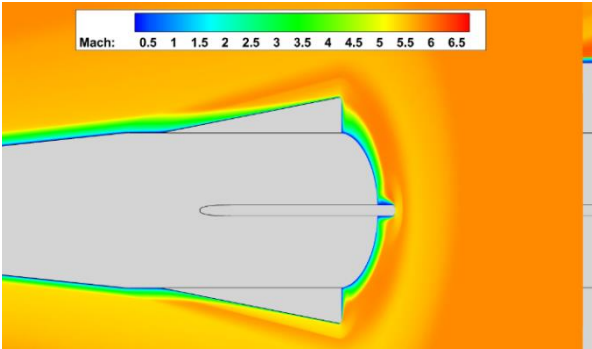
Figure A.1: Contours of the conic missile of Mach number (a)-(c) and density gradient magnitude (d)-(f) at various angles of attack with a slice at $x = 10.77$ inches.



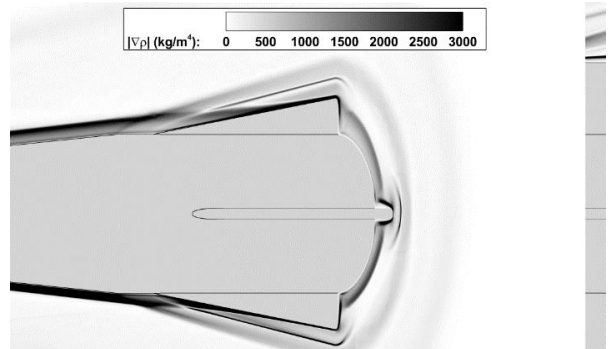
(a) $AoA = 0^\circ$



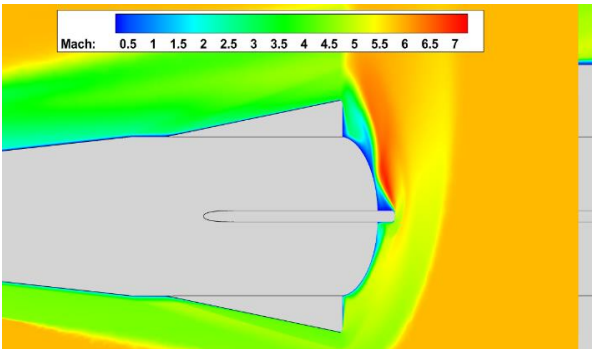
(d) $AoA = 0^\circ$



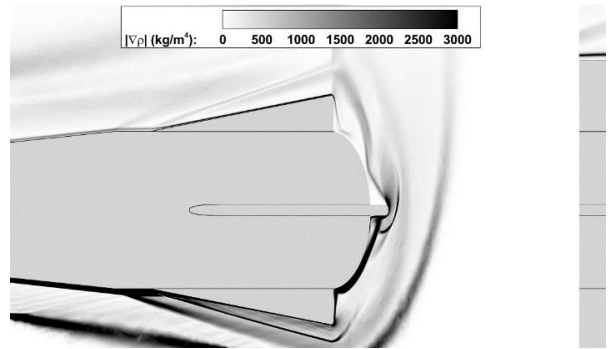
(b) $AoA = 1^\circ$



(e) $AoA = 1^\circ$

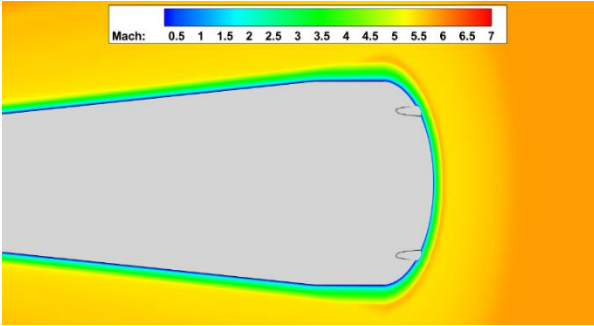


(c) $AoA = 10^\circ$

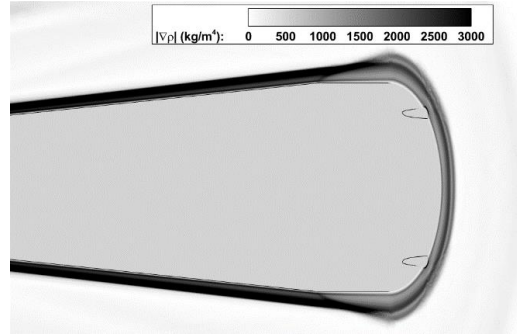


(f) $AoA = 10^\circ$

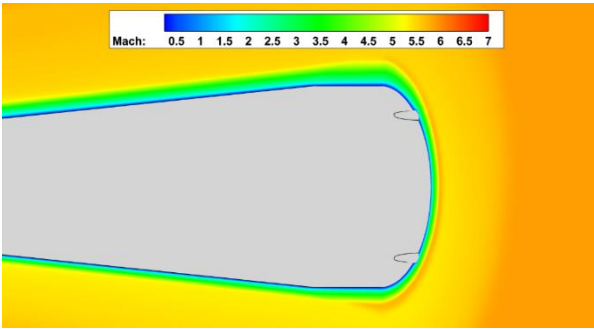
Figure A.2: Contours of the conic missile of Mach number (a)-(c) and density gradient magnitude (d)-(f) at various angles of attack with a slice at $x = 12.68$ inches.



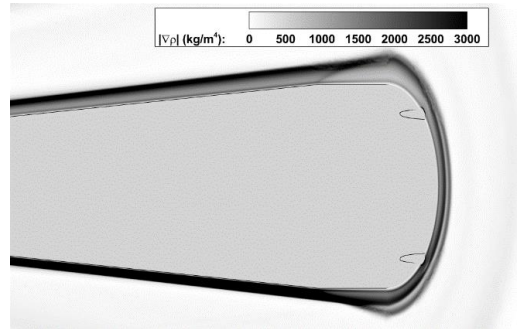
(a) $AoA = 0^\circ$



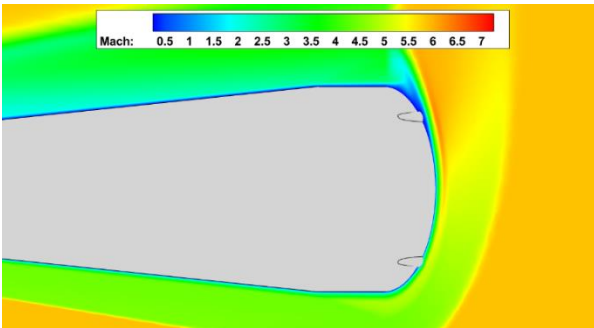
(d) $AoA = 0^\circ$



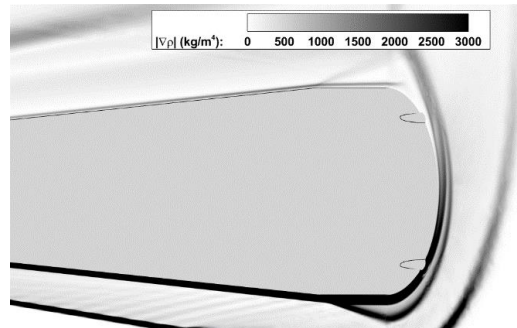
(b) $AoA = 1^\circ$



(e) $AoA = 1^\circ$

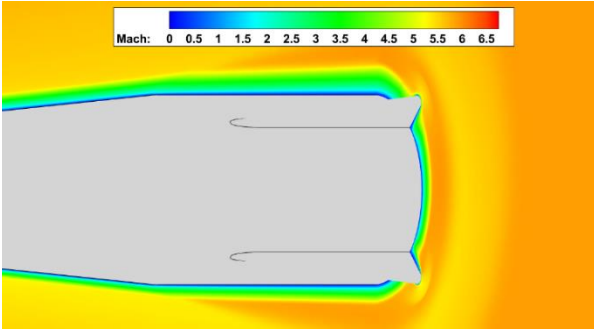


(c) $AoA = 10^\circ$

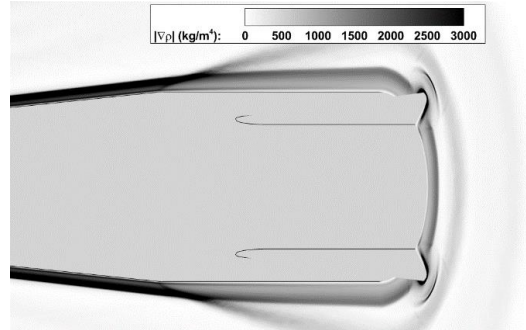


(f) $AoA = 10^\circ$

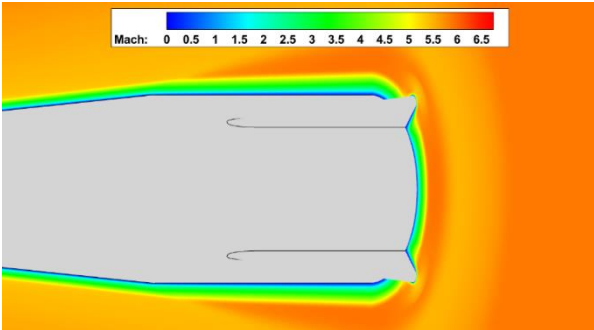
Figure A.3: Contours of the conic missile +1 configuration of Mach number (a)-(c) and density gradient magnitude (d)-(f) at various angles of attack with a slice at $x = 10.77$ inches.



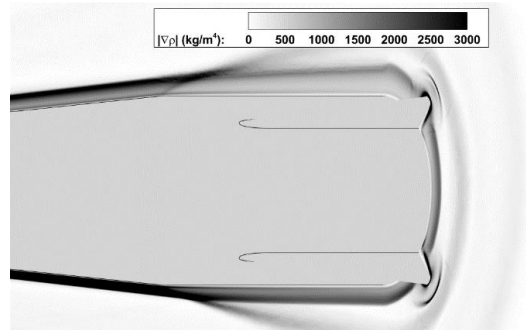
(a) $AoA = 0^\circ$



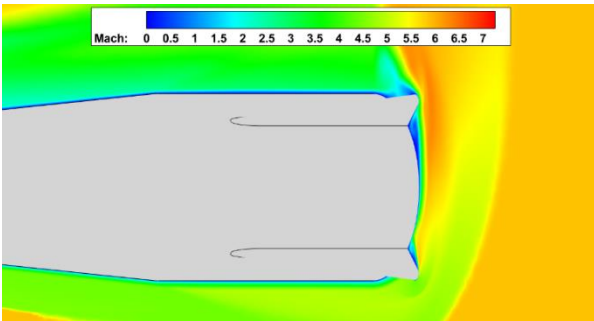
(d) $AoA = 0^\circ$



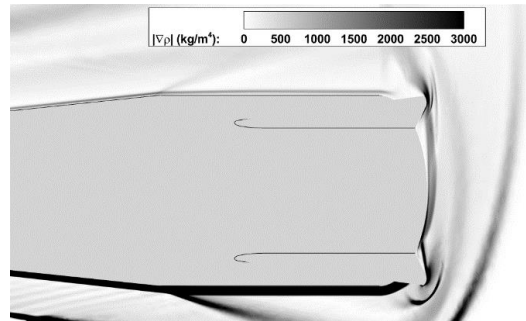
(b) $AoA = 1^\circ$



(e) $AoA = 1^\circ$

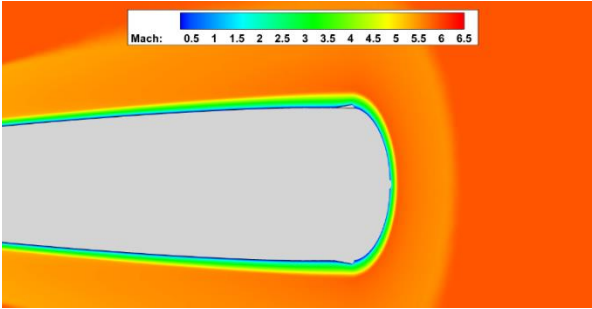


(c) $AoA = 10^\circ$

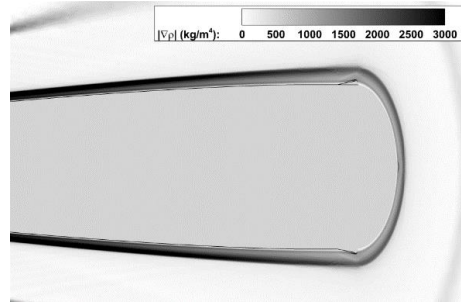


(f) $AoA = 10^\circ$

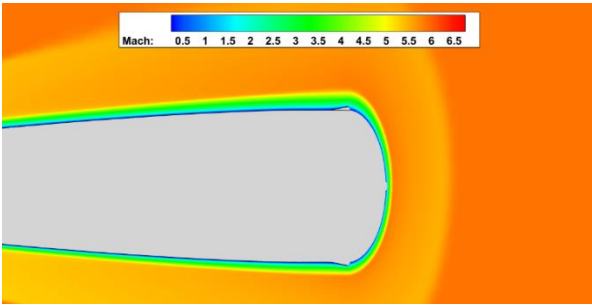
Figure A.4: Contours of the conic missile +1 configuration of Mach number (a)-(c) and density gradient magnitude (d)-(f) at various angles of attack with a slice at $x = 12.68$ inches.



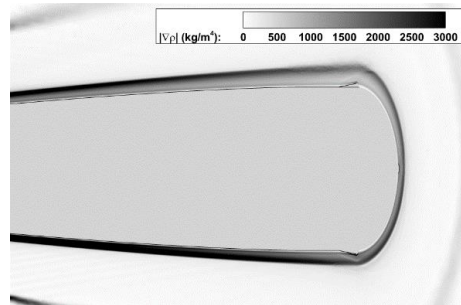
(a) $AoA = 0^\circ$



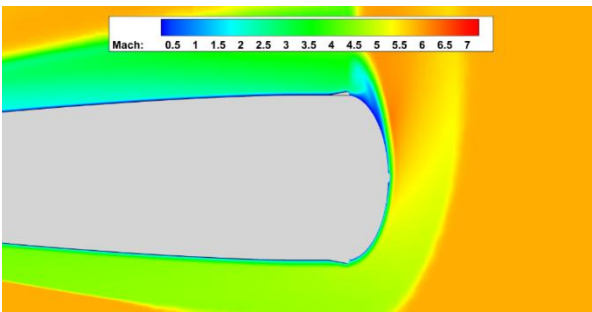
(d) $AoA = 0^\circ$



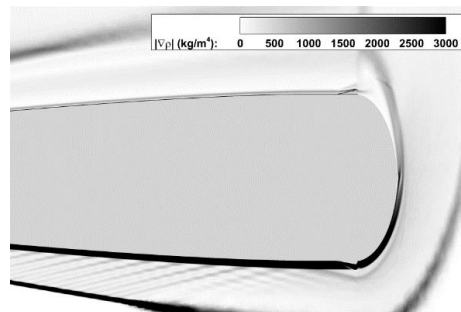
(b) $AoA = 1^\circ$



(e) $AoA = 1^\circ$

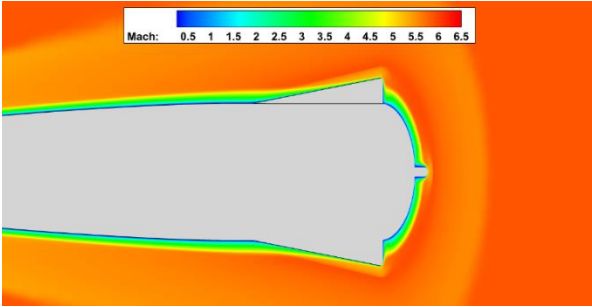


(c) $AoA = 10^\circ$

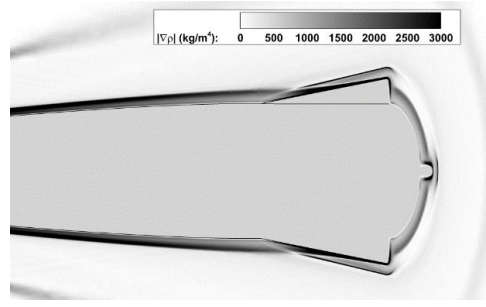


(f) $AoA = 10^\circ$

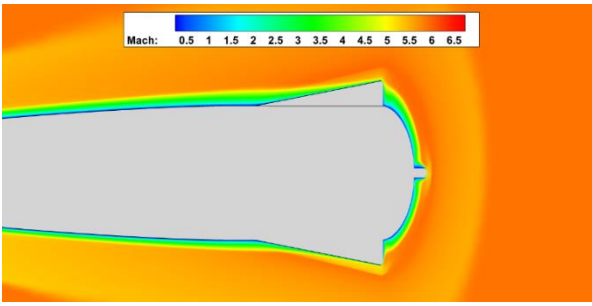
Figure A.5: Contours of the ogive missile of Mach number (a)-(c) and density gradient magnitude (d)-(f) at various angles of attack with a slice at $x = 10.77$ inches.



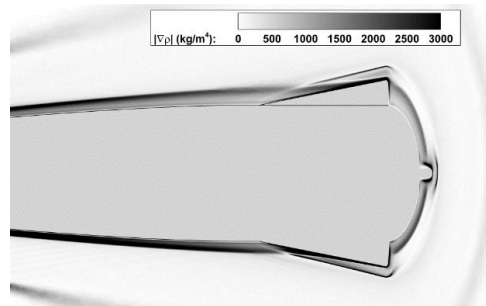
(a) $AoA = 0^\circ$



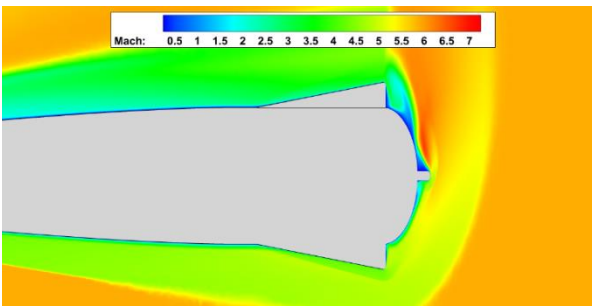
(d) $AoA = 0^\circ$



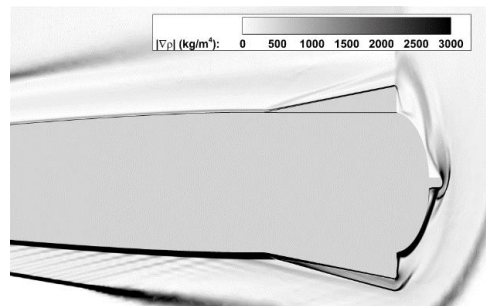
(b) $AoA = 1^\circ$



(e) $AoA = 1^\circ$

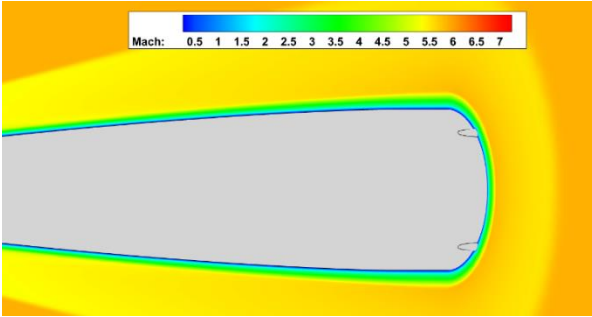


(c) $AoA = 10^\circ$

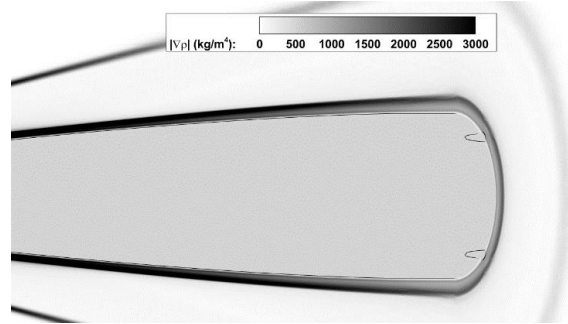


(f) $AoA = 10^\circ$

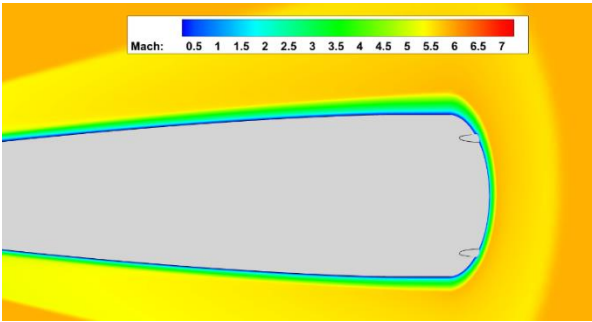
Figure A.6: Contours of the ogive missile of Mach number (a)-(c) and density gradient magnitude (d)-(f) at various angles of attack with a slice at $x = 12.68$ inches.



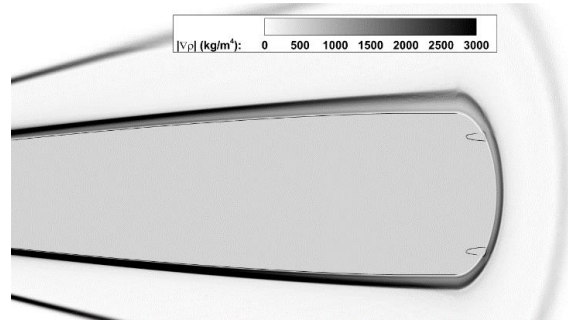
(a) $AoA = 0^\circ$



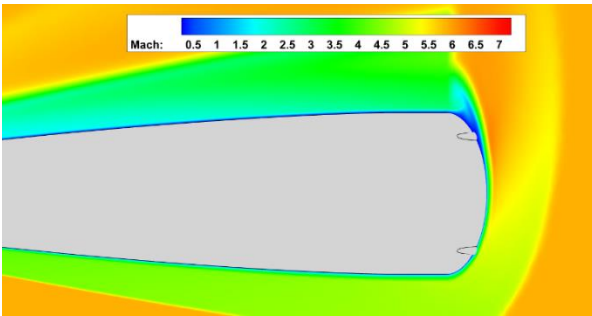
(d) $AoA = 0^\circ$



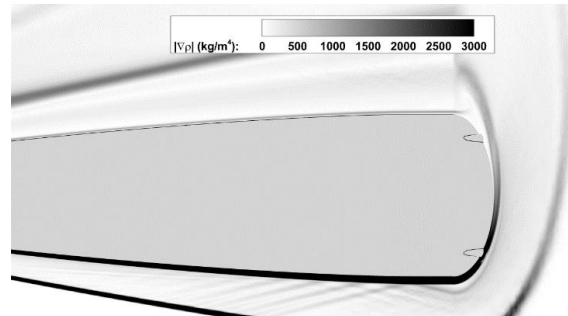
(b) $AoA = 1^\circ$



(e) $AoA = 1^\circ$

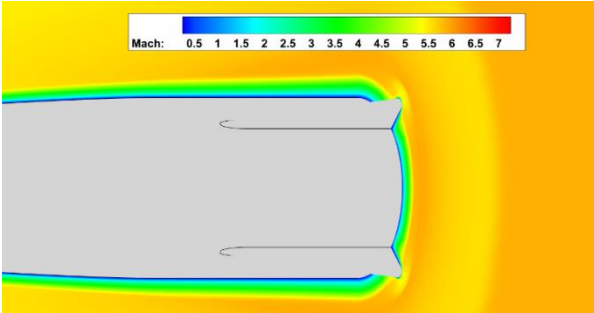


(c) $AoA = 10^\circ$

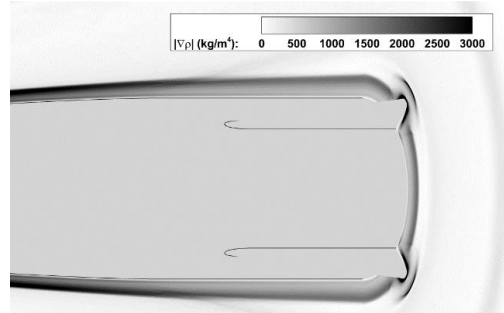


(f) $AoA = 10^\circ$

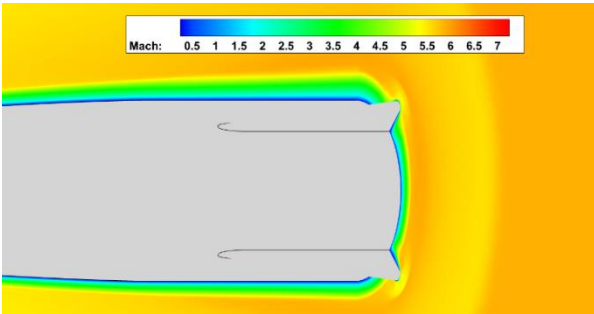
Figure A.7: Contours of the ogive +1 missile configuration of Mach number (a)-(c) and density gradient magnitude (d)-(f) at various angles of attack with a slice at $x = 10.77$ inches.



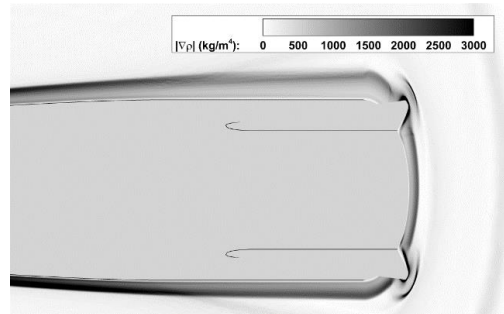
(a) $AoA = 0^\circ$



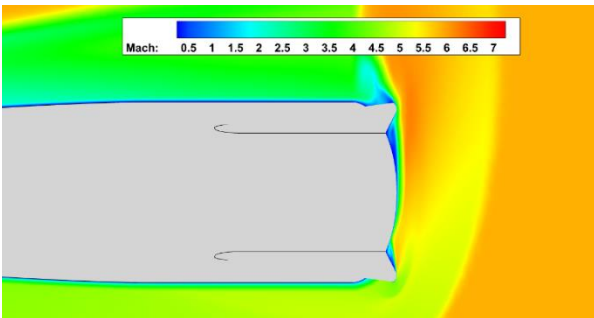
(d) $AoA = 0^\circ$



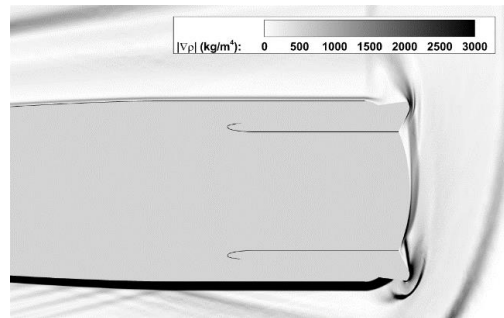
(b) $AoA = 1^\circ$



(e) $AoA = 1^\circ$



(c) $AoA = 10^\circ$



(f) $AoA = 10^\circ$

Figure A.8: Contours of the ogive +1 missile configuration of Mach number (a)-(c) and density gradient magnitude (d)-(f) at various angles of attack with a slice at $x = 12.68$ inches.

APPENDIX B: DESCRIPTION OF INPUT PARAMETERS TO CONTUR [8]

Input	Columns	Description
Card 1		
ITL	2-12	Title
JD	14-15	0 for axisymmetric, -1 for planar
Card 2		
GAM	1-10	Specific heat ratio
AR	11-20	Gas constant, $\frac{ft^2}{s^2R}$
ZO	21-30	compressibility factor
RO	31-40	Turbulent boundary-layer recovery factor
VISC	41-50	Constant in viscosity law
VISM	51-60	Constant in viscosity law. If $VISM \leq 1$, $\mu = VISC \times T^{VISM} \frac{lb - sec}{ft^2}$ <p>If $VISM \geq 1$, $\mu = \frac{VISC \times T^{1.5}}{T + VISM} \frac{lb - sec}{ft^2}$ <p>If $T > VISM$, $\mu = \frac{VISC \times T}{2 \times VISM^{1/2}}$</p></p>
SFOA	61-70	Specifies 3 rd , 4 th , or 5 th -deg axial velocity distribution in radial flow region
XLB	71-89	If $XLB = 1000.$, the spline fit subroutines are used to obtain values at evenly spaced increments
Card 3		
ETAD	1-10	Inflection angle in degrees
RC	11-20	Ratio of throat radius of curvature to throat radius

FMACH	21-30	Mach number at Point <i>F</i> if $ETAD = 60$. Calculated if not given
BMACH	31-40	Mach number at Point <i>B</i>
CMC	41-50	Absolute value is design Mach number at Point <i>C</i>
SF	51-60	Scale factor by which nondimensional coordinates are multiplied to give dimensions in inches. Negative value specifies the inviscid exit radius.
PP	61-70	Station (in.) at Point <i>A</i> . $PP = 0$ gives coordinates relative to geometric throat.
XC	71-80	Nondimensional distance from source to Point <i>C</i> . Also specifies centerline Mach distribution as <i>3rd</i> , <i>4th</i> , or <i>5th</i> degree

Card 4

MT	1-5	Number of points on characteristic <i>EG</i> if $ETAD \neq 60$ or <i>CD</i> if $ETAD = 60$. Maximum value about 125.
NT	6-10	Number of points on axis <i>IE</i> . Maximum value is 149– <i>LR</i> .
IX	11-15	Determines if third derivative of velocity distribution is matched with transonic solution, source flow value, or constant.
IN	16-20	Determines type of distribution from Point <i>B</i> to Point <i>C</i>
IQ	21-25	Zero for complete contour.
MD	26-30	Number of points on characteristic <i>AB</i> . Maximum value about 125.
ND	31-35	Number of points on axis <i>BC</i> . Maximum value is 150.
NF	36-40	Absolute value is number of points on characteristic <i>CD</i> for $ETAD \neq 60$. Maximum value is 149 or $200 - ND - MP - MQ $ —number of points on upstream contour.
MP	41-45	Number of points on conical section <i>GA</i> if $FMACH \neq EMACH$.
MQ	46-50	Number of points downstream of Point <i>D</i> if parallel inviscid contour desired

JB	51-55	Positive number if boundary-layer calculation is desired before spline fit. Negative number transfers control of program to <i>JX</i> .
JX	56-60	Positive number calls for calculation of streamlines.
JC	61-65	If not zero, calls for printout of intermediate characteristics within upstream contour if $JC > 0$ and downstream if $JC < 0$.
IT	66-70	Number of points at which spline fit is desired if points are not evenly spaced. Use only for planar nozzle.
LR	71-75	Absolute value is number of points on throat characteristic used in characteristics solution. Negative values give printout of transonic solution.
NX	76-80	Number from 10 to 20 determines spacing of points on axis for upstream contour. <i>NX</i> gives linear spacing. $NX > 10$ gives closer spacing of points at upstream end than at downstream end.

Card 5

NOUP	1-5	Number of times upstream contour is smoothed
NPCT	6-10	Smoothing factor in percent.
NODO	11-15	Number of times downstream contour is smoothed.

Card 6

PPQ	1-10	Stagnation pressure (psia)
TO	11-20	Stagnation temperature, Rankine
TWT	21-30	Throat wall temperature, Rankine, if $QFUN = 0$.
TWAT	31-40	Wall temperature, Rankine, at Point <i>D</i> .
QFUN	41-50	Heat transfer function at the throat. $Q = 0$ is adiabatic.
ALPH	51-60	Parameter specifying temperature distribution in boundary-layer. $ALPH = 1$. uses quadratic distribution. $ALPH = 0$ uses parabolic distribution. $ALPH = -1$. uses quadratic distribution

for reference temperature and parabolic in calculation of boundary shape parameters.

IHT	61-65	Integer which determines temperature distribution.
IR	66-70	Parameter specifying transformation from incompressible to compressible values. $IR = 2$, Coles' transformation for C_f and Re_θ . $IR = 1$, TP is calculated by a modification of the Spalding-Chi (Van Driest) method. $IR = 0$, Van Driest value of Re_{θ_i} is used. $IR = -1$, Coles' law of corresponding stations is used.
ID	71-75	$ID = \pm 1$, axisymmetric effects are included in momentum equation and in calculation of boundary-layer parameters.
LV	76-80	Absolute value, usually 5, determines number of times boundary-layer solution is iterated so that the radius terms in momentum equation refer to viscid radius instead of inviscid radius.

Card 7

XST	1-10	Station (in.) for throat value of X . If $XST = 1000.$, program uses value previously determined by specifying PP on Card 3.
XLOW	11-20	Starting value for interpolation. Second value of interpolated $X = XLOW + XINC$
XEND	21-30	End value for interpolation. If 0, $SPLIND$ is used to calculate slope and $\frac{\partial^2 y}{\partial x^2}$ at same points as previously defined.
XINC	31-40	Increment in X for interpolation. If zero and $BJ > 10$, contour is divided into BJ increments.
BJ	41-50	Value to update JB for subsequent calculation. $JB = BJ$.
XMID	51-60	Intermediate value for interpolation. Distance ($XMID - XLOW$) is divided into increments defined by $XINC$, and distance ($XEND - XMID$) is divided into increments defined by $XINC2$

XINC2	61-70	Increments in <i>X</i> between <i>XMID</i> and <i>XEND</i> if different that <i>XINC</i> .
CN	71-80	Number of copies desired of final tabulation of coordinates if more than one copy is desired.

APPENDIX C: MATLAB WRAPPER FOR SIVELLS' MOC COMPUTER PROGRAM

```
function SivellWrapper
% Run Sivell's method of characteristics fortran 77 script. Iterate through
% variables by reading in the input card and changing the values. After the
% script finishes, find the output file, rename it, and move it before the
% next iteration runs.
%
% files saved as data_rc_etad.txt
% where rc is the respective ratio of the throat radius of curvature to
% throat radius and etad is the respective inflection angle

% Set inputs
rc = {'6.0','8.0','10.0','12.0','14.0','16.0'};
etad = {'6.0','12.0','20.0','30.0','40.0','50.0','60.0'};

for ii = 1:length(etad)
for jj = 1:length(rc)
    % card 1
    info.itle = 'MACH 6'; % title
    info.jo = '0'; % 0 for axisymmetric, -1 for planar

    % card 2
    info.gam = '1.3448'; % cp/cv ratio
    info.ar = '1692.3'; % gas constant
    info.zo = '1.'; % compressibility factor
    info.ro = '0.89'; % turbulent BL recovery factor
    info.visc = '8.3338E-7'; % viscosity if VISM = 0 (constant viscosity). constant for viscosity
law
    info.vism = '0.'; % constant for sutherland's
    info.sfoa = '0'; % if ~=0, distance from throat to A (in)
    info.xbl = '1000.';

    % card 3
    info.etad = etad{ii}; % inflection angle in degrees
    info.rc = rc{jj}; % ratio of throat radius of curvature to throat radius
    info.fmach = '0';
    info.bmach = '4.8'; % mach number at point B if ETAD ~= 60.
    info.cmc = '6.13'; % design mach number at point c
    info.sf = '-4.'; % if < 0, radius of exit [in]
    info.pp = '0.'; % if ~= 0, station at A [in]
    info.xc = '0'; % nondimensional distance from source to C

    % card 4
```

```

info.mt = '61';
info.nt = '41';
info.ix = '0';           % decides how third derivate is calculated
info.in = '10';
info.iq = num2str((str2double(etad{ii}) == 60)*1);
info.md = '41';
info.nd = '49';
info.nf = '-61';
info.mp = '0';
info.mq = '0';
info.jb = '1';
info.jx = '0';
info.jc = '0';
info.it = '0';           % only use for planar nozzle
info.lr = '-21';
info.nx = '13';

% card 5
info.noup = '50';
info.npct = '85';
info.nodo = '50';

% card 6
info.ppq = '524.8336'; % stagnation pressure [psia]
info.t0 = '3427.9';    % stagnation temperature [R]
info.twt = '2500.';    % throat wall temp. 0 == adiabatic
info.twat = '540.';    % wall temp at D [R]
info.qfun = '0.';      % heat transfer function at throat.
info.alph = '0';        % used for temp. distribution in BL
info.iht = '0';
info.ir = '0';          % specifies transformation from incompressible to compressible values.
info.id = '1';
info.lv = '5';

% card 7
info.xst = '1000.';
info.xlow = '5.';
info.xend = '0.';
info.xinc = '.01';
info.bj = '0';
info.xmid = '0';
info.xinc2 = '0';
info.cn = '0';

makeCard(info)

```

```

% check to see if a file named 'data.txt' exists. If it does not exist,
% create the file
file = dir;
file = {file.name};
if ~contains(file,'data.txt')
    save('data.txt')
end

unix(fullfile(cd,'MAIN.exe')); % run linux command
movefile(fullfile(cd,'data.txt'),...
    fullfile(cd,'Results',[ 'data_',rc{jj},'_' ,etad{ii},'.txt'])); % move file to results folder
end
end
disp('done')
end

function makeCard(info)
card1 = makeCard1(info);
card2 = makeCard2(info);
card3 = makeCard3(info);
card4 = makeCard4(info);
card5 = makeCard5(info);
card6 = makeCard6(info);
card7 = makeCard7(info);

% concatenate cards and write to file
CARD = vertcat(card1, card2, card3, card4, card5, card6, card7);
[row,~] = size(CARD);
fid = fopen('input.txt','w'); % open text file to write
for i = 1:row
    fprintf(fid,'%s\n',CARD(i,:));
end
fclose(fid);
end

function card = makeCard1(info)
% Create space for card 1
card = blanks(80);
ITLE = blanks(11); ITLE(1:length(info.itle)) = info.itle;
JO = blanks(2); JO(1:length(info.jo)) = info.jo;
card(2:12) = ITLE; card(14:15) = JO;
end

```



```

function card = makeCard2(info)
% create space for card 2
card = blanks(80);
GAM = blanks(10); GAM(1:length(info.gam)) = info.gam;
AR = blanks(10); AR(1:length(info.ar)) = info.ar;
Z0 = blanks(10); Z0(1:length(info.zo)) = info.zo;
R0 = blanks(10); R0(1:length(info.ro)) = info.ro;
VISC = blanks(10); VISC(1:length(info.visc)) = info.visc;
VISM = blanks(10); VISM(2:length(info.vism)+1) = info.vism;
SFOA = blanks(10); SFOA(1:length(info.sfoa)) = info.sfoa;
XBL = blanks(10); XBL(1:length(info.xbl)) = info.xbl;
card(1:10) = GAM; card(11:20) = AR; card(21:30) = Z0; card(31:40) = R0;
card(41:50) = VISC; card(51:60) = VISM; card(61:70) = SFOA; card(71:80) = XBL;
end

```

```

function card = makeCard3(info)
% create space for card 3
card = blanks(80);
ETAD = blanks(10); ETAD(1:length(info.etad)) = info.etad;
RC = blanks(10); RC(1:length(info.rc)) = info.rc;
FMACH = blanks(10); FMACH(1:length(info.fmach)) = info.fmach;
BMACH = blanks(10); BMACH(1:length(info.bmach)) = info.bmach;
CMC = blanks(10); CMC(1:length(info.cmc)) = info.cmc;
SF = blanks(10); SF(1:length(info.sf)) = info.sf;
PP = blanks(10); PP(1:length(info.pp)) = info.pp;
XC = blanks(10); XC(1:length(info.xc)) = info.xc;
card(1:10) = ETAD; card(11:20) = RC; card(21:30) = FMACH; card(31:40) = BMACH;
card(41:50) = CMC; card(51:60) = SF; card(61:70) = PP; card(71:80) = XC;
end

```

```

function card = makeCard4(info)
% A zero value of MT, NT, MD, or ND will allow a repeat of calculations
% for parameters specified by new cards No. 3 and 4.
% A negative value will allow a repeat of calculations for new
% cards Nos. 1, 2, 3, and 4.

% create space for card 4
card = blanks(80);
MT = blanks(5); MT(1:length(info.mt)) = info.mt;
NT = blanks(5); NT(1:length(info.nt)) = info.nt;
IX = blanks(5); IX(1:length(info.ix)) = info.ix;
IN = blanks(5); IN(1:length(info.in)) = info.in;
IQ = blanks(5); IQ(1:length(info.iq)) = info.iq;
MD = blanks(5); MD(1:length(info.md)) = info.md;

```

```

ND = blanks(5); ND(1:length(info.nd)) = info.nd;
NF = blanks(5); NF(1:length(info.nf)) = info.nf;
MP = blanks(5); MP(1:length(info.mp)) = info.mp;
MQ = blanks(5); MQ(1:length(info.mq)) = info.mq;
JB = blanks(5); JB(1:length(info.jb)) = info.jb;
JX = blanks(5); JX(1:length(info.jx)) = info.jx;
JC = blanks(5); JC(1:length(info.jc)) = info.jc;
IT = blanks(5); IT(1:length(info.it)) = info.it;
LR = blanks(5); LR(1:length(info.lr)) = info.lr;
NX = blanks(5); NX(1:length(info.nx)) = info.nx;
card(1:5) = MT; card(6:10) = NT; card(11:15) = IX; card(16:20) = IN;
card(21:25) = IQ; card(26:30) = MD; card(31:35) = ND; card(36:40) = NF;
card(41:45) = MP; card(46:50) = MQ; card(51:55) = JB; card(56:60) = JX;
card(61:65) = JC; card(66:70) = IT; card(71:75) = LR; card(76:80) = NX;
end

```

```

function card = makeCard5(info)
% create space for card 5
card = blanks(80);
NOUP = blanks(5); NOUP(1:length(info.noup)) = info.noup;
NPCT = blanks(5); NPCT(1:length(info.npct)) = info.npct;
NODO = blanks(5); NODO(1:length(info.nodo)) = info.nodo;
card(1:5) = NOUP; card(6:10) = NPCT; card(11:15) = NODO;
end

```

```

function card = makeCard6(info)
% create space for card 6
card = blanks(80);
PPQ = blanks(10); PPQ(1:length(info.ppq)) = info.ppq;
T0 = blanks(10); T0(1:length(info.t0)) = info.t0;
TWT = blanks(10); TWT(1:length(info.twt)) = info.twt;
TWAT = blanks(10); TWAT(1:length(info.twat)) = info.twat;
QFUN = blanks(10); QFUN(1:length(info.qfun)) = info.qfun;
ALPH = blanks(10); ALPH(1:length(info.alph)) = info.alph;
IHT = blanks(5); IHT(1:length(info.iht)) = info.iht;
IR = blanks(5); IR(1:length(info.ir)) = info.ir;
ID = blanks(5); ID(1:length(info.id)) = info.id;
LV = blanks(5); LV(1:length(info.lv)) = info.lv;
card(1:10) = PPQ; card(11:20) = T0; card(21:30) = TWT; card(31:40) = TWAT;
card(41:50) = QFUN; card(51:60) = ALPH; card(61:65) = IHT; card(66:70) = IR;
card(71:75) = ID; card(76:80) = LV;
end

```

```

function card = makeCard7(info)
% create space for card 7
card = blanks(80);
XST = blanks(10); XST(1:length(info.xst)) = info.xst;
XLOW = blanks(10); XLOW(1:length(info.xlow)) = info.xlow;
XEND = blanks(10); XEND(1:length(info.xend)) = info.xend;
XINC = blanks(10); XINC(1:length(info.xinc)) = info.xinc;
BJ = blanks(10); BJ(1:length(info.bj)) = info.bj;
XMID = blanks(10); XMID(1:length(info.xmid)) = info.xmid;
XINC2 = blanks(10); XINC2(1:length(info.xinc2)) = info.xinc2;
CN = blanks(10); CN(1:length(info.cn)) = info.cn;
card(1:10) = XST; card(11:20) = XLOW; card(21:30) = XEND; card(31:40) = XINC;
card(41:50) = BJ; card(51:60) = XMID; card(61:70) = XINC2; card(71:80) = CN;
end

```

This research was sponsored by the Army Research Laboratory and was accomplished under Cooperative Agreement Number W911NF-20-2-0189. The views and conclusions contained in this document are those of the authors and should not be interpreted as representing the official policies, either expressed or implied, of the Army Research Laboratory, or the U.S. Government. The U.S. Government is authorized to reproduce and distribute reprints for Government purposes notwithstanding any copyright notation herein.